HELLENIC REPUBLIC
National and Kapodistrian University of Athens

Department of Physics and Medical School

MASTER THESIS

FUNDAMENTALS OF MAGNETIC PARTICLE IMAGING: A SIMULATION STUDY

SIDERI ATHINA

20181071

Supervisor:
Efstathios Stiliaris, Associate Professor

ATHENS 2020

The present work was also co-supervised by Dr. Spiridon Spirou from the “Sismanogleio - Amalia Fleming” General Hospital.

Examination Committee

P. Karaiskos, Professor

Medical School, National and Kapodistrian University of Athens ……..

P. Bouziotis, Research Director

Institute of Nuclear & Radiological Sciences, Technology, Energy & Safety, NCSR *Demokritos* ……..

E. Stiliaris, Associate Professor

Department of Physics, National and Kapodistrian University of Athens ……..

Oral Presentation and Examination: August 25, 2020

Acknowledgments

I would like to thank Prof. Efstathios Stiliaris, for his guidance and for providing his expertise and valuable time. I am extremely grateful that I was welcomed to his SPECT-Lab group, and had the chance to collaborate with distinguished people.

I would like to express my gratitude to Dr. Spiridon Spirou, for introducing Magnetic Particle Imaging to me and for providing all of his knowledge for this project. For her contribution and for providing samples of SPIO nanoparticles for experimentations, I would like to thank nanoparticles' specialist, Dr. Penelope Bouziotis.

At last but not least, I would like to thank all of the SPECT-Lab members, my friends and family for their help and support.

CONTENTS

Abstract

Operating principles of Magnetic Particle Imaging (MPI) and reconstruction using the Algebraic Reconstruction Technique (ART) under the influence of noise that exists in Magnetic Particle Imaging with a Field Free Line encoding scheme images, are examined in this Thesis.

The aim of this study is first to introduce MPI and all the necessary aspects for the understanding of its basic operating principles and then examine the effect that the generated noise in MPI causes on the quality of resulting images using iterative reconstruction techniques. To carry out this study, MPI simulations were performed using the COMSOL Multiphysics software package. Two MPI scanners, one with Field Free Point (FFP) and one with Field Free Line (FFL) encoding scheme were simulated in order to prove the principle of operation. The magnetic behavior of superparamagnetic iron oxide (SPIO) nanoparticles that are used as tracers in MPI was also simulated. In the imaging process, a three-source software phantom was created and reconstructed in order to test the performance of the Algebraic Reconstruction Technique for different numbers of projections. In addition, a Digital Subtraction Angiography (DSA) image of an internal carotid artery with a sacciform aneurysm was converted into a software phantom which was later reconstructed using ART. In order to consider the noise in the MPI signal, a combined model with Gauss like noise and linear attenuation was added. The effect of the noise in the reconstructed image was evaluated.

Introduction

Magnetic Particle Imaging (MPI) is a novel medical imaging modality capable of imaging the distribution of Superparamagnetic Iron Oxide (SPIO) nanoparticles offering high sensitivity, high resolution, and fast data acquisition. In addition, MPI offers high contrast due to the absence of any background signal from tissues and zero signal attenuation from different depths of interaction. Applications of MPI such as angiography, oncology, inflammation, stem cell tracking are under active research. MPI as a tracer-based imaging technique could be used for a variety of functional imaging applications similarly to Positron Emission Tomography (PET) and Single-Photon Emission Computed Tomography (SPECT), but without the use of ionizing radiation.

The present work is organized as follows:

In the first chapter, the basic principles of electromagnetism are discussed. Physical quantities and fundamental laws of electromagnetic theory necessary for a complete understanding of Magnetic Particle Imaging are provided.

The basic principle of MPI is based on the nonlinear magnetization behavior of the SPIO tracer nanoparticles. MPI signal is generated from SPIO tracers as they respond to applied magnetic fields. In the second chapter, a brief overview of composition and characteristic behavior of SPIO nanoparticles is presented and the phenomenon of superparamagnetism is further discussed.

In the third chapter, a synopsis about the evolution of MPI is given and an outline of the Magnetic Particle Imaging operating principles is introduced. The signal generation using oscillating magnetic fields to excite the magnetization of SPIO tracers and the signal reception by receive coils as well as quantification of the signal are explained. In addition, spatial encoding, achieved by applying gradient fields and thus spatially varying particle response, are presented. The various encoding schemes for data acquisition are also discussed in this chapter.

To conduct the simulations in this study, COMSOL Multiphysics simulation package was used. COMSOL Multiphysics is a general-purpose simulation platform that allows to build multidimensional models, set up the physics for the model and, most importantly, it allows to couple different physics interfaces. In chapter four, simulation results are presented. The generated magnetic field from

Helmholtz and Maxwell coil pairs was calculated and evaluated. Both MPI scanner topologies, with Field Free Point (FFP) and with Field Free Line (FFL) encoding scheme, were simulated. Some simple Lissajous trajectories of the FFP and the line rotation in the FFL scanning procedure are presented. Subsequently, the superparamagnetic behavior of SPIO nanoparticles was simulated.

In chapter five, the general concept of reconstruction procedure in MPI is presented and the ability to use the Algebraic Reconstruction Technique (ART) for the reconstruction of MPI images is argued. The basic principles of ART are also discussed. In order to get acquainted with the reconstruction using ART, a study was conducted showing the dependence of image quality on the number of projections. To evaluate how the noise, resulted by magnetic field imperfections and the intrinsic noise of the detector in MPI, affects the quality of reconstructed images, a Digital Subtraction Angiography (DSA) image of an internal carotid artery with a sacciform aneurysm was considered. Images of this software phantom were reconstructed using ART, before and after adding noise to the data.

A summary of MPI and general remarks of the current study are given at the end of the thesis. The advantages of MPI as a new image modality and its potential future applications are finally discussed.

CHAPTER 1. FUNDAMENTALS OF ELECTROMAGNETISM

1.1 Introduction

In this chapter basic principles of electromagnetism necessary for describing Magnetic Particle Imaging are discussed. A brief overview of the theory of magnetic fields and the physics of magnetic materials is provided. Definition of electromagnetic quantities, Maxwell's equations for two approximations, quasi static and time dependent current distribution, are introduced. Biot-Savart law is derived and exploited for the calculation of the magnetic field generated by electromagnetic coils. Voltage induction due to magnetization or magnetic field change and the law of reciprocity are also discussed. Furthermore, the phenomenon of magnetization of materials is described, magnetic materials based on their magnetic properties are classified.

1.2 Maxwell's Equations

Maxwell's equations are a set of equations written in differential or integral form, that describe electromagnetic phenomena in a unified theory. They have been proposed by Maxwell in the years 1861-1864 where he combined three laws by Gauss, Faraday and Ampere and extended them by the displacement current [KNO12].

Differential Form	Integral Form	Name of Law	
$\nabla \cdot \vec{D} = \rho_v$	$\oint_S \vec{D} \cdot d\vec{S} = \int_v \rho_v dV$	Gauss's Law	(1.1)
$\nabla \times \vec{E} = -\frac{\partial \vec{B}}{\partial t}$	$\oint_c \vec{E} \cdot d\vec{l} = -\int_s \frac{\partial \vec{B}}{\partial t} d\vec{S}$	Faraday's Law	(1.2)
$\nabla \cdot \vec{B} = 0$	$\oint_s \vec{B} \cdot d\vec{S} = 0$	Gauss's Law of Magnetics	(1.3)
$\nabla \times \vec{H} = \vec{j} + \frac{\partial \vec{D}}{\partial t}$	$\oint_c \vec{H} \cdot d\vec{l} = \int_S \left(\vec{j} + \frac{\partial \vec{D}}{\partial t}\right) d\vec{S}$	Ampere's Law	(1.4)

Figure1. Maxwell's Equations.

Where the Vectoral quantity

- E is the electric field measured in V/m
- H is the magnetic field strength measured in A/m
- B is the magnetic flux density measured in T
- D is the electric displacement field measured in C/m^2
- ρ is the free charge density measured in C/m^3
- J_c is the free current density measured in A/m^2

The scalar field

- $\int_v \rho dV := Q^f$ denotes the free electrical charge (1.5)
- $\int_S \vec{B} \cdot d\vec{S} := \Phi_S^B$ denotes the magnetic flux (1.6)
- $\int_S \overrightarrow{D} \cdot d\vec{S} := \Phi_S^D$ denotes the electrical flux and (1.7)
- $\int_S^f \vec{j} \cdot d\vec{S} := I_S^f$ denotes the free electrical current (1.8)

Gauss's law relates the distribution of electric charge to the resulting electric displacement field within a close surface showing that the source of the electrical field lines is electrical charges in such a way that field lines are directed from positive to negative charges. Gauss's law of magnetism states that the magnetic field B has divergence equal to zero and is equivalent to the statement that magnetic monopoles do not exist. In addition, it states that the field lines of magnetic flux density have to be closed. Faraday's law of induction describes how the change of magnetic flux density results in electric field generation. Ampere's law indicates that a magnetic field can be generated by both an electrical or by a displacement current [KNO12].

1.3 Magnetic Materials

Magnetization or magnetic polarization $\vec{M}$ is a vectoral quantity that expresses the density of permanent or induced magnetic dipole moments in a magnetic material. Magnetic moments origins in either microscopic electric currents resulting from the motion of electrons in atoms, or the spin of the electrons or the nuclei. Magnetization is not necessarily uniform within a material.

Magnetization also describes how materials respond to an applied magnetic field as well as the way the material changes the magnetic field. The magnetic behavior of materials can be classified into the following categories: diamagnetism, paramagnetism, ferromagnetism, ferrimagnetism and antiferromagnetism. The materials that have the corresponding behavior are characterized as diamagnetic, paramagnetic, ferromagnetic, ferrimagnetic and antiferromagnetic. [WIKI], [GEH10].

The classification of the different types of magnetic materials is based on their permeability and susceptibility. For this reason, these two properties of materials have to be defined before proceeding with the differences between the magnetic materials.

- Magnetic permeability $\mu = \frac{\partial \vec{B}}{\partial \vec{H}}$ (1.9)

- Magnetic susceptibility $\chi_m = \frac{\partial \vec{M}}{\partial \vec{H}}$ (1.10)

Since B and M can be linear or not, depending on the type of material in the medium, permeability and susceptibility may or may not be constant depending on the case. Sometimes the relative permeability is used instead of permeability.

- Relative permeability $\mu_r = \frac{\mu}{\mu_0}$ (1.11)

where μ_0 is the permeability of free space, in SI $\mu_0 = 4\pi \times 10^{-7}$ H/m. The relative permeability of free space is 1. The relative permeability is related to susceptibility by the equation

$$\mu_r = \chi_m + 1 \quad (1.12)$$

Diamagnetic materials have a small and negative susceptibility $\chi_m \approx -10^{-5}$ and their magnetic momentum tends to resist the externally imposed magnetic field. Examples of such materials are copper, silver, gold, bismuth and beryllium. Paramagnetic materials have small but positive susceptibility values, ranging from $10^{-5} \leq \chi_m \leq 10^{-3}$. The magnetization of these materials is weak and is oriented in the same direction as the external magnetic field. Examples of this category are aluminum, platinum and manganese. The susceptibility of ferromagnetic materials is positive, much higher than 1 ranging from $50 \leq \chi_m \leq 10000$. Examples of these materials are iron, cobalt, nickel and various rare earths as well as their alloys.

Other types of magnetic materials, ferrimagnetic, antiferromagnetic and superparamagnetic were discovered much later than the categories mentioned above. According to the measurement of susceptibility, ferromagnetic are very difficult to distinguish from ferrimagnetic, while antiferromagnetic and superparamagnetic have been confused for many years for paramagnetic materials. In ferrimagnets, the magnetic moments of the sublattices moments are not equal resulting in a net magnetic moment. Ferrimagnetism is similar to ferromagnetism exhibiting ferromagnetic behavior such as spontaneous magnetization, same Curie temperatures, hysteresis, and remanence. However, ferro- and ferrimagnets have very different magnetic ordering. An example of ferrimagnetic material is magnetite. In antiferromagnetic materials sublattice moments are exactly equal but opposite, as a result the net moment is zero.

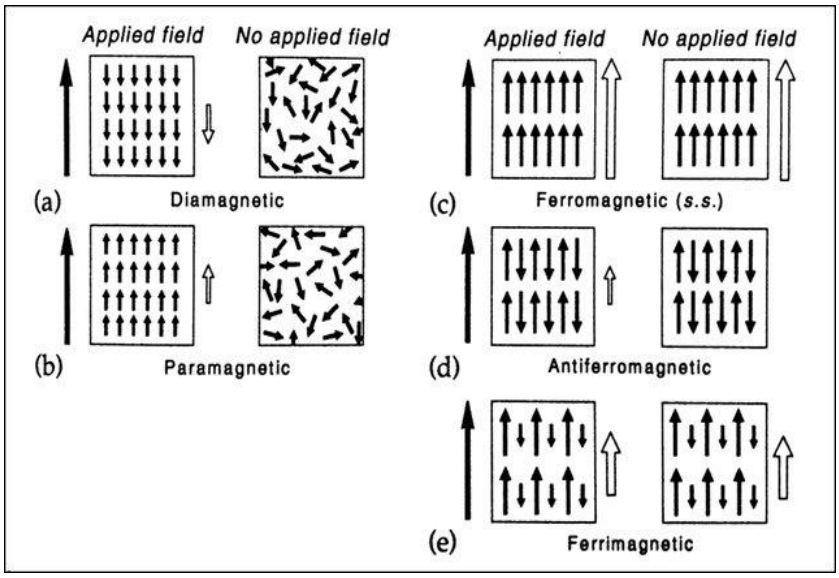

Figure 2. Arrangement of magnetic moments.

Magnetic moment per atom or ion of an ordinary paramagnetic material is just a few times μ_B (Bohr magneton $\mu_B = \hbar\, e/2m_e$). For a spherical particle of Iron with a diameter of 50 Angstrom magnetic moment is much greater (~12000μ_B) the term superparamagnetism was suggested to describe the magnetic behavior of such particles.

Superparamagnetism describes the magnetic behavior of nanoparticles used in MPI and will be further discussed in a subsequent section.

1.4 Constitutive Relations

The constitutive relations which relate the magnetic flux B with the magnetic flux strength H and the electrical flux density D to the electric field E describe the macroscopic relation of the medium.

$$\vec{D} = \varepsilon_0 \vec{E} + \vec{P} \tag{1.13}$$

$$\vec{B} = \mu_0 (\vec{H} + \vec{M}) \tag{1.14}$$

$$\vec{J} = \sigma \vec{E} \tag{1.15}$$

where $\varepsilon_0 \approx 8.854 \cdot 10^{-12} \mathrm{Fm}^{-1}$ is the permittivity of vacuum, $\mu_0 = 4\pi \cdot 10{-}7$ H/m is the permeability of vacuum, and σ is the electrical conductivity. M the magnetization and P the polarization of the medium. $\vec{M}$, $\vec{P}$ and σ are spatially and temporally dependent.

For linear and isotropic materials, the polarization is directly proportional to the electric field and the magnetization is directly proportional to the magnetic field,

$$\vec{P} = \varepsilon_0 \chi_e \vec{E} \tag{1.16}$$

where χ_e is the electric susceptibility, and χ_m is the magnetic susceptibility and

$$\chi_e = \varepsilon_r - 1 \tag{1.17}$$

For these materials the constitutive relations are

$$\vec{D} = \varepsilon_0(1 + \chi_e)\vec{E} = \varepsilon_0\varepsilon_r\vec{E} = \varepsilon\vec{E} \tag{1.18}$$

$$\vec{B} = \mu_0(1 + \chi_m)\vec{H} = \mu_0\mu_r\vec{H} = \mu\vec{H} \tag{1.19}$$

The relation between the free current density and the electrical field is called Ohm's law and is formulated as

$$u = RI^f \tag{1.20}$$

where

$$R = \frac{l}{\sigma A} \tag{1.21}$$

is the electrical resistance of the conductor with l being the length of the conductor and A its cross section.

$$u := \int_0^l \vec{E} \cdot d\vec{l} \tag{1.22}$$

denotes the electric voltage between the end points of the conductor.

Considering the total current j which consist of the free current density j^f and the bound current density j^b, $\vec{j} = \vec{j}^f + \vec{j}^b$, constitutive can be formulated as follows, [JAC99], [KNO12],

$$\nabla \times \vec{M} = j^b + \frac{\partial \vec{P}}{\partial t} \tag{1.23}$$

$$\nabla \times \vec{B} = \mu_0\vec{j} + \mu_0\varepsilon_0\frac{\partial \vec{E}}{\partial t} \tag{1.24}$$

1.4.1 Quasi static Approximation and Time independent Current distribution

Solving Maxwell's equations means a set of partial differential equations needs to be solved, which is computationally demanding. Usually numerical methods such as the Finite Elements Method (FEM) and the Finite Differences Method (FDM) are being used.

Under specific conditions, depending on different factors such as the size of the considered region (described by the maximum diameter D_{region}), the maximum occurring frequency f_{max}, and the material properties, quasi-static approximation can be applied. In this approximation, displacement current $\varepsilon_0 \frac{\partial \vec{E}}{\partial t}$ is neglected, thus Ampère's law is now formulated

$$\nabla \times \vec{B} = \mu_0 \vec{j} \tag{1.25}$$

Two conditions have to be fulfilled in order to consider quasi-static approximation

1. Minimum wavelength must be considerably larger than the size of the considered region
$$\lambda_{min} \gg D_{region} \Leftrightarrow \frac{c}{f_{max}} \gg D_{region} \Leftrightarrow f_{max} \ll \frac{1}{\sqrt{\varepsilon\mu} D_{region}}$$
2. Displacement current $\varepsilon_0 \frac{\partial \vec{E}}{\partial t}$ must be significantly smaller than current density $\vec{j}$ or $f_{max} \ll \frac{\sigma}{\varepsilon}$

As has been discussed in [KNO12] the critical frequency under which one can consider quasi-static approximation in MPI is 20MHz. In MPI the frequencies in the sent chain are in kHz range and in the receive chain about 2 MHz. Thus, Maxwell's displacement current can be neglected leading to the conclusion that a change in current density results immediately in a change of the generated magnetic field.

Another approximation is the assumption of time independent current distribution. This implies that applying a time-dependent current will not result in a different current distribution within the conductor. This assumption is often violated even for low frequencies due to the skin effect, that is the tendency of an alternating electric current (AC) to become distributed within a conductor in a way the current density is largest near the surface of the conductor and decreases with depth [WIKI]. In order to avoid this effect conductors are made of litz wire (several thin wires) when applying frequencies in kHz range and up to 1MHz.

1.5 Biot-Savart Law

The magnetic field produced by a constant linear current is given by the Biot-Savart law

$$\vec{B}(r) = \frac{\mu_0}{4\pi}\int \frac{I\times\hat{\tau}}{\tau^2} dl' = \frac{\mu_0}{4\pi} I \int \frac{d\vec{l}'\times\hat{\tau}}{\tau^2} \tag{1.26}$$

The integration is done along the path of the current in the flow direction, $d\vec{l}'$ is the length element on the wire and τ the vector from the source point, r', at the calculation point, r, and the unit is 1T=1N/(Am)=10^4 Gauss [GRI99].

According to Gauss's law of magnetism, the divergence of the magnetic flux density is zero, this means that a magnetic vector potential A exists, so that

$$\vec{B} = \nabla \times \vec{A} \tag{1.27}$$

However, this definition does not define a unique magnetic vector potential. More precisely, since the divergence of the curl of any vector field is equal to zero, the sum of any scalar function φ with A will satisfies the aforementioned equation. To define a unique magnetic vector potential, a common choice is to consider

$$\nabla \cdot \vec{A} = 0 \tag{1.28}$$

Under this consideration Ampère's law is formulated

$$\nabla^2 \vec{A} = -\mu_0 \vec{j} \tag{1.29}$$

In order to solve of this partial differential equation Green's function for the Laplace operator is applied

Within the quasi-static approximation and for the Coulomb gauge, the magnetic vector potential A can be explicitly computed by

$$\vec{A}(r) = \frac{\mu_0}{4\pi}\int_{R^3} \frac{\vec{j}\left(\vec{r'},t\right)}{\tau} d^3\vec{r}' \tag{1.30}$$

By exploiting the explicit expression of the magnetic vector potential, $\vec{A}$, Biot-Savart law can be written

$$\vec{H}(r,t) = \frac{1}{4\pi}\int_{R^3} \frac{\vec{j}^f(r',t)\times\vec{\tau}}{\tau^3} d^3\vec{r}' \tag{1.31}$$

The static field generated by a conductor with unit current I=1A and current density $\hat{j}^f(\vec{r})$ is given by

$$\vec{p}(r) = \frac{1}{4\pi}\int_{R^3} \frac{\hat{j}^f(r\prime)\times\vec{\tau}}{\tau^3} d^3\vec{r}' \tag{1.32}$$

and it's called coil sensitivity.
For a time-independent current distribution, the magnetic field strength can be expressed in terms of the coil sensitivity as

$$\vec{H}(\vec{r},t) = \mathrm{I(t)}\vec{p}(r) \tag{1.33}$$

as described in [KNO12].

1.6 Electromagnetic Induction

Faraday's law implies that the temporal change of the magnetic flux density induces an electric voltage.

Assuming an electromagnetic coil consisting of a single loop of an infinite small wire. The surface enclosed by the coil is denoted by S with boundary ∂S. The voltage between the end points of the conductor is equal to the integration of the electric field strength E along the conductor

$$u(t) = \int_{\partial S} \vec{E}(\vec{l},t)\cdot d\vec{l} \tag{1.34}$$

Now, Faraday's law of induction leads to

$$u(t) = -\frac{d\Phi_S^{\vec{B}}}{dx} = -\frac{d}{dt}\int_S \vec{B}\cdot d\vec{A} \tag{1.35}$$

Where $\Phi_S^{\vec{B}}$ is the magnetic flux density through the surface S. This says that the induced voltage is a result of the magnetic flux density change.

Furthermore,

$$u(t) = -\frac{d\Phi_S^{\vec{B}}}{dx} = -\frac{d}{dt}\int_S \vec{B}\cdot d\vec{A} = -\frac{d}{dt}\int_S (\nabla\times\vec{A}(\vec{l},t))\cdot d\vec{A} \tag{1.36}$$

Using Stokes Theorem, the voltage u between the end points of a conductor enclosing the surface S can be computed by

$$u(t) = -\frac{d}{dt}\int_{\partial S}\vec{A}(\vec{l},t)\cdot d\vec{l} \tag{1.37}$$

Now, consider a coil consisting of several windings. The voltage induced in the volume coil can be computed using the aforementioned relation, integrating over the cross section of the coil leading to the volume integral

$$u(t) = -\frac{d}{dt}\int_{V_R}\vec{A}(\vec{r'},t)\cdot\hat{j}^{R}(r')\cdot d^3\vec{r'} \tag{1.38}$$

where $\hat{j}^{R}(r')$ is the unit current density and V^R the volume of the coil.

If u_{H} is the voltage induced by the change of the magnetic field strength and u_{M} the voltage induced by the change of the magnetization

$$u(t) = u_M(t) + u_H(t) \tag{1.39}$$

with

$$u_H(t) := -\frac{d}{dt}\int_{V^R}\vec{A}^H(\vec{r'},t)\cdot\hat{j}^{f}(r')\cdot d^3\vec{r'} \tag{1.40}$$

$$u_M(t) := -\frac{d}{dt}\int_{V^R}\vec{A}^M(\vec{r'},t)\cdot\hat{j}^{b}(r')\cdot d^3\vec{r'} \tag{1.41}$$

1.6.1 Coil Coupling

The voltage $u_{\mathrm{H}}(t)$ induced by Q send coils with volume V_q^S and current densities $j_q^S(\vec{r},t) = I_q(t)\hat{j}_q^S(\vec{r})$, q=0, ..., Q-1, is given by

$$u_H(t) = -\frac{d}{dt}\sum_{q=0}^{Q-1} I_q(t)\,\xi_q \tag{1.42}$$

where $\xi_q = \frac{\mu_0}{4\pi}\int_{V_R}\left(\int_{V_q^S}\frac{\hat{j}_q^S(r)\cdot\hat{j}^R(r')}{\tau}d^3r\right)d^3r'$.

This formula derives from (1.40) for the magnetic potential

$$\vec{A}^H(r,t) = \frac{\mu_0}{4\pi}\int_{R^3}\frac{\vec{j}^f\left(\vec{r'},t\right)}{\tau}d^3\vec{r}' \tag{1.43}$$

and shows that the superposition of currents applied to send coils directly couples into the receive coil [KNO12].

1.6.2 Law of Reciprocity

The voltage u_M induced by a time varying magnetization $\vec{M}(\vec{r},t)$ in a receive coil with sensitivity $\vec{p}(\vec{r})$ is given by the expression

$$u_M(t) = -\mu_0 \int_{V^M} \frac{\partial}{\partial t} \vec{M}(\vec{r},t) \cdot \vec{p}(\vec{r}) d^3\vec{r} \tag{1.44}$$

which is called the law of reciprocity and derives from (1.41) by inserting the magnetic potential

$$\vec{A}^M(r,t) = \frac{\mu_0}{4\pi} \int_{R^3} \frac{\nabla \times \vec{M}(r',t)}{\tau} d^3\vec{r}' \tag{1.45}$$

and shows that the sensitivity of a receive coil is the magnetic field strength generated by the coil when a unit current is applied. This states that the receiving properties of a coil are the same as the field generating properties [HOU11], [KNO12].

CHAPTER 2. SUPERPARAMAGNETIC IRON OXIDE NANOPARTICLES AS MPI TRACERS

2.1 Introduction

Magnetic Particle Imaging does not provide natural contrast and thus a tracer is needed to achieve imaging, the performance of which is of major importance [BUZ10]. Superparamagnetic nanoparticles based on a core consisting of iron oxides are used as MPI tracer. It is known that iron oxide particles are tolerated by the human body since they are already available as contrast agents for Magnetic Resonance Imaging (MRI) [GLE13]. Superparamagnetic Iron Oxide nanoparticles (SPIOs) are injected into the body and can be traced due to their characteristic magnetic behavior when exposed to a combination of external magnetic fields. In this chapter, SPIO nanoparticles' characteristics are presented and the phenomenon of superparamagnetism is further discussed.

2.2 Composition of SPIO Nanoparticles

Superparamagnetic Iron Oxide nanoparticles consist of a magnetic core and a non-magnetic coating as shown in Figure 3. For the size determination of the particle, D_{hydro} is the hydrodynamic diameter of the particle including both the core and its coating and it is an important factor as far as the medical applications concerned. D_{core} is the diameter of the magnetic core and is an important property since it determines the shape of the magnetization curve of the particle.

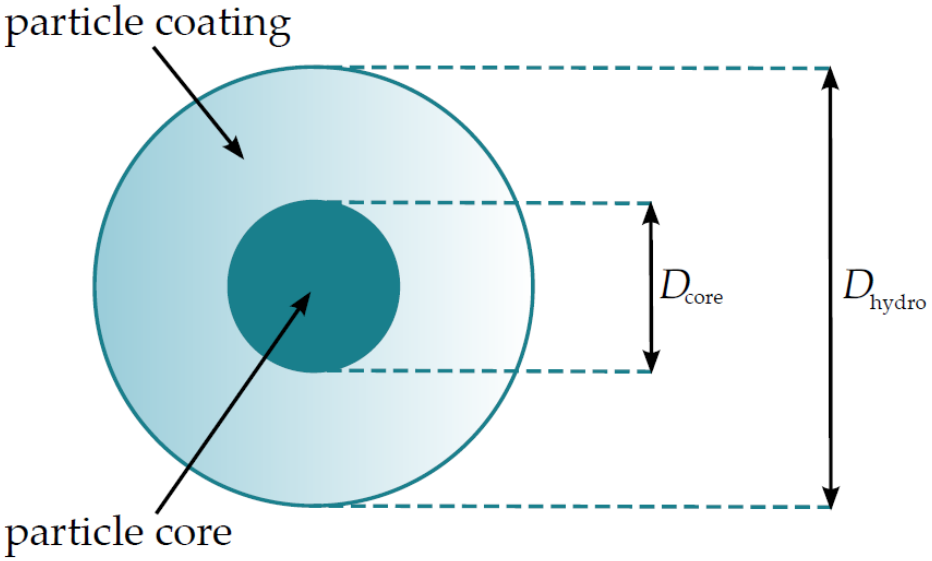

Figure 3. Schematic drawing of a spherical SPIO nanoparticle consisting of a magnetic core and a non-magnetic coating [ERB14].

For the imaging process not only the magnetic properties of core's material are important. The appropriate coating is of crucial importance since it determines the magnetic behavior of the particles. The magnetic neutral coating prevents particles from cluster due to their magnetic properties. Particle's coating should be sufficiently thick, so that particle-particle interactions become negligible, allowing each particle to have its own magnetic domain or in other words to be a single domain particle as it will be discussed in the following section. Furthermore, the coating ensures bio capability of the particles [KNO12], [ERB14].

2.3 Superparamagnetic Behavior of SPIO Nanoparticles

Nanoparticles show different behavior in comparison with larger particles of the same material. When magnetic iron-oxide based nanoparticles are small enough that the magnetic core becomes a single domain, the particles become superparamagnetic [BUZ12] even though the magnetic core of the particles consists of a ferromagnetic substance.

The formation of magnetic domains, known as Weiss domains, is a characteristic of ferromagnetic materials. In these domains, the atomic magnetic moments $\vec{m}_a$ are aligned so that a non-zero magnetization arises. Weiss domains are present, even if an external magnetic field is not applied. Exposing a ferromagnetic material to an external magnetic field leads the atomic magnetic moments $\vec{m}_a$ of all domains to orient in parallel. The size of these domains differs, depending on the corresponding material. Assuming spherical particles, the critical diameter D_{cr}, which is the largest diameter being energetically efficient for a particle to consist of one single domain

$$D_{cr}=\frac{72\sqrt{AK_A}}{\mu_0 M_{sat}^2} \tag{2.1}$$

where:
K_A is the anisotropy constant and
A is the exchange stiffness constant [ERB14].

The critical diameter D_{cr} only depends on material constants. In MPI, magnetite Fe_3O_4 is most often used as tracer and the corresponding saturation field strength of magnetite is given

$$M_{sat} = 0.6\ T\mu_0^{-1} \tag{2.2}$$

For magnetite the value of the critical diameter varies from 12.4 nm up to a range of 30 - 100 nm [ERB14].

For single-domain particles all aligned atomic magnetic moments $\vec{m}_a$ of each particle can be summed up to one particle magnetic moment $\vec{m}$. Since the non-magnetic coating diminishes particle-particle interactions, the behavior of the magnetic moments $\vec{m}$ of the SPIO nanoparticles can be correlated to this of the non-interacting atomic magnetic moments $\vec{m}_a$ of a paramagnetic material [ERB14].

2.3.1 Magnetic Moment of SPIO Nanoparticles

For SPIO particles distributed in a stable suspension, i.e. a ferrofluid, the magnetic moment is approximately given

$$\vec{m} = VcM\text{sat}\ \hat{e}_{\mu} \tag{2.3}$$

where:
V_C the volume of the particle core,
M_{sat} the bulk saturation magnetization of the core material and
$\hat{e}_{\mu}$ denotes a unit vector in direction of the orientation of the magnetic moment of the SPIO particle [ERB14].

Formula (2.1) applies under the assumption of perfectly aligned atomic magnetic moments $\vec{m}_a$ in the one magnetic domain of the corresponding nanoparticle [ERB14]. In reality, the magnetic moment of an SPIO particle depends on the exact formation of the magnetic domains, which will not always be ideally homogeneous [ERB14]. Inhomogeneities in the magnetic alignment will probably occur for different particle sizes. It is important to mention that for particle diameter below 3 nm, the intrinsic force of the particle will not suffice to cause ferromagnetic behavior [GSV06], [ERB14]. In addition, domain formation will be influenced by surface effects and the formation of vortices that occur for particles with a diameter close to the critical diameter [ERB14].

2.3.2 Magnetization of SPIO Nanoparticles

Magnetization is defined as the magnetic moment per volume

$$\vec{M} := \frac{d\vec{m}}{dV} \tag{2.4}$$

As a discrete formulation

$$\vec{M} = \frac{1}{\Delta V}\sum_{J=1}^{N}\vec{m}_j \tag{2.5}$$

If one considers a small finite volume ΔV, which is of the size of an image voxel, N is the number of SPIO particles in this volume and $\vec{m}_j$ the magnetic moment of the j_{th} SPIO particle.

For a distribution of N SPIO particles a mean magnetic moment is defined

$$\vec{m} = \frac{1}{N}\sum_{J=1}^{N} \vec{m}_j \tag{2.6}$$

and the magnetization is now given

$$\vec{M} = \frac{N}{\Delta V}\vec{m} = c\vec{m} \tag{2.7}$$

with c being the particle concentration, defined as the number of particles N per volume ΔV [ERB14], i.e.

$$c := \frac{N}{\Delta V} \tag{2.8}$$

This linear relation between the magnetization M and the concentration c is exploited in MPI as the received signal is analogue to the derivative of the magnetization and consequently to concentration c.

Due to Brownian motion, the directions of the particles' magnetic moments are randomly distributed. As a result, the sum of the magnetic moments is zero. When applying an external magnetic field, $\vec{H}$, the particles' magnetic moments align with the applied field thus a non-zero magnetization in the direction of the applied field arises. At a certain field strength, the majority of particles' magnetic moment is aligned with the applied magnetic field such that the magnetization remains in saturation for further increase of the field strength [KNO12].

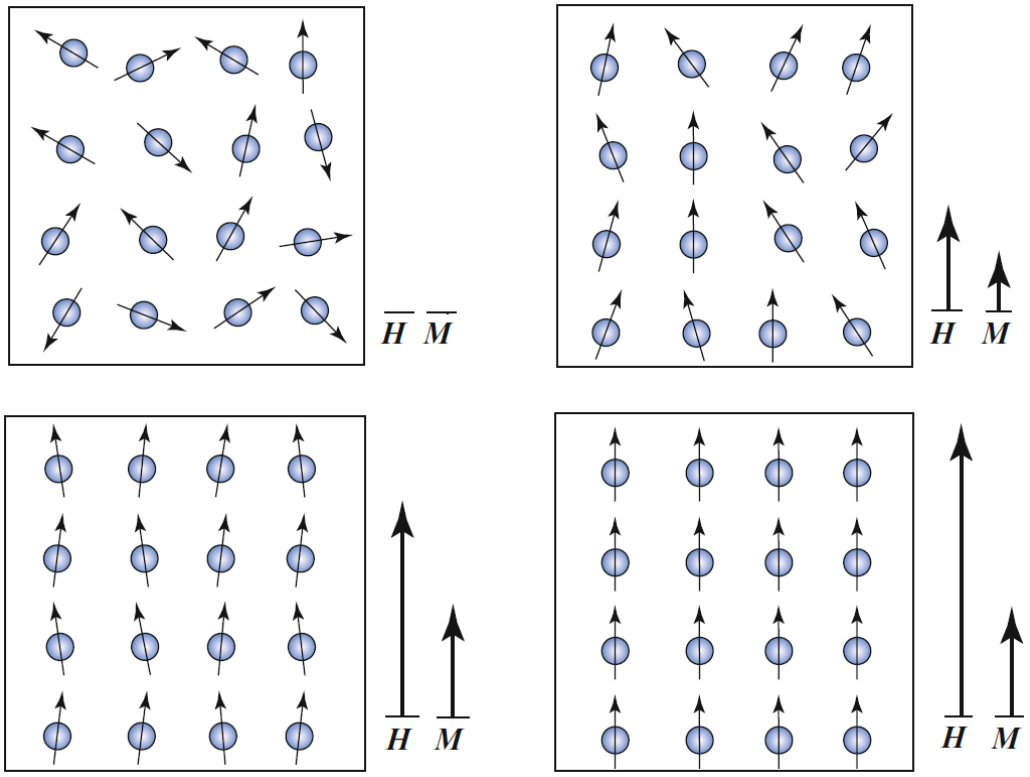

Figure 4. Magnetic behavior of superparamagnetic nanoparticles when applying external magnetic field $\vec{H}$ [KNO12].

Saturation does not occur at an arbitrarily low magnetic field. Thermal fluctuations move the magnetization out of the direction of the external field. To maintain the magnetization in the direction of the external field H, the magnetic energy of the particle must be on the order of the thermal energy [GLE13]. The necessary condition for saturation to occur is

$$\vec{H}V\vec{M}_{sat}\ \mu_0 \gtrapprox k_BT \qquad (2.9)$$

where:
V is the particle volume,
M_{sat} the saturation magnetization of the particle material,
K_B the Boltzmann constant, and
T the absolute temperature.

This means the particle volume must be large in order to observe saturation at low magnetic field strength [GLE13].

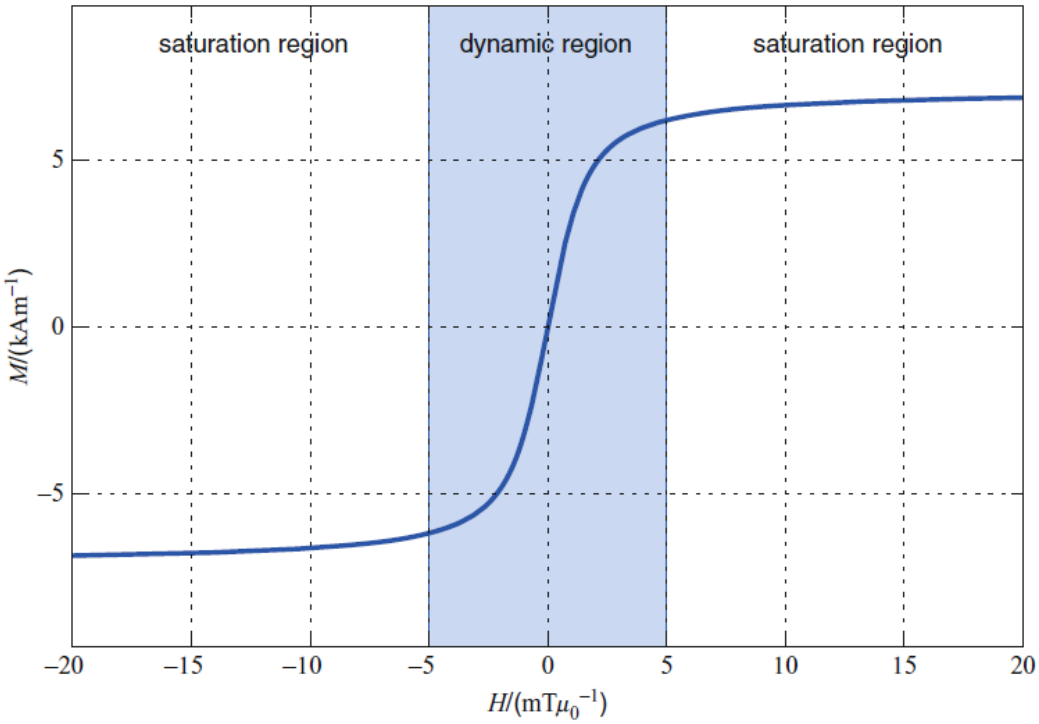

Figure 5. Magnetization curve of particles with D=30 nm particle diameter and unit iron concentration [KNO12].

This non-linear magnetization behavior is a fundamental characteristic of superparamagnetic materials. Neglecting anisotropy of the particles and hysteresis effects, the magnetization curve of a distribution of SPIO particles in thermal equilibrium can be described by the Langevin theory of paramagnetism [GLE13], [ERB14].

2.3.3 Langevin Theory of Paramagnetism

As discussed before the relation between the magnetization of a distribution of SPIO nanoparticles and the external magnetic field $\vec{H}$ is not linear as shown in Figure 5. The magnetization exhibits a sharp increase, as the external field increases from zero to a certain field strength (dynamic region). For further increase of the magnetic field strength, the magnetization flattens and stays into saturation (saturation region). This is a result of the alignment of the majority of particles' magnetic moments with the external magnetic field such that the maximum magnetization is reached. Increasing the field strength beyond this point will not lead to a change in particles' magnetization. This is an important factor for spatial encoding in MPI as will be discussed later.

As shown in [ERB14], the magnetization behavior of an SPIO particle distribution can be modeled using the Langevin function

$$\mathcal{L}(\xi) = \begin{cases} coth(\xi) - \frac{1}{\xi} & \xi \neq 0 \\ 0 & \xi = 0 \end{cases} \quad (2.10)$$

by the

$$\vec{M}(\vec{H}, t) = \frac{N\vec{m}}{V}\mathcal{L}(\beta) \quad (2.11)$$

Using (2.8), equation (2.11) is reformulated

$$\vec{M}(\vec{H}, t) = c\vec{m}\mathcal{L}(\beta) \quad (2.12)$$

where

$$\beta := \frac{\mu_0 \vec{m} \cdot \vec{H}}{K_B T_p} \quad (2.13)$$

K_B is the Boltzmann constant and T_p the particle Temperature.

For monodisperse spherical particles the mean magnetic moment is given

$$m = V_{sat} M_{sat} \quad (2.14)$$

with M_{sat} being the saturation magnetization of the particle core material
and

$$V_{core} = \frac{1}{6}\pi D_{core}^3 \quad (2.15)$$

the volume of the core of the particle with core diameter D_{core} [KNO17].

It is now obvious that the shape of the magnetization curve depends on the core diameter of the particle through the magnetic moment.

In Figure 6. particle magnetization M as a function of the applied field strength H for different particle core diameters D and unit iron concentration is shown.

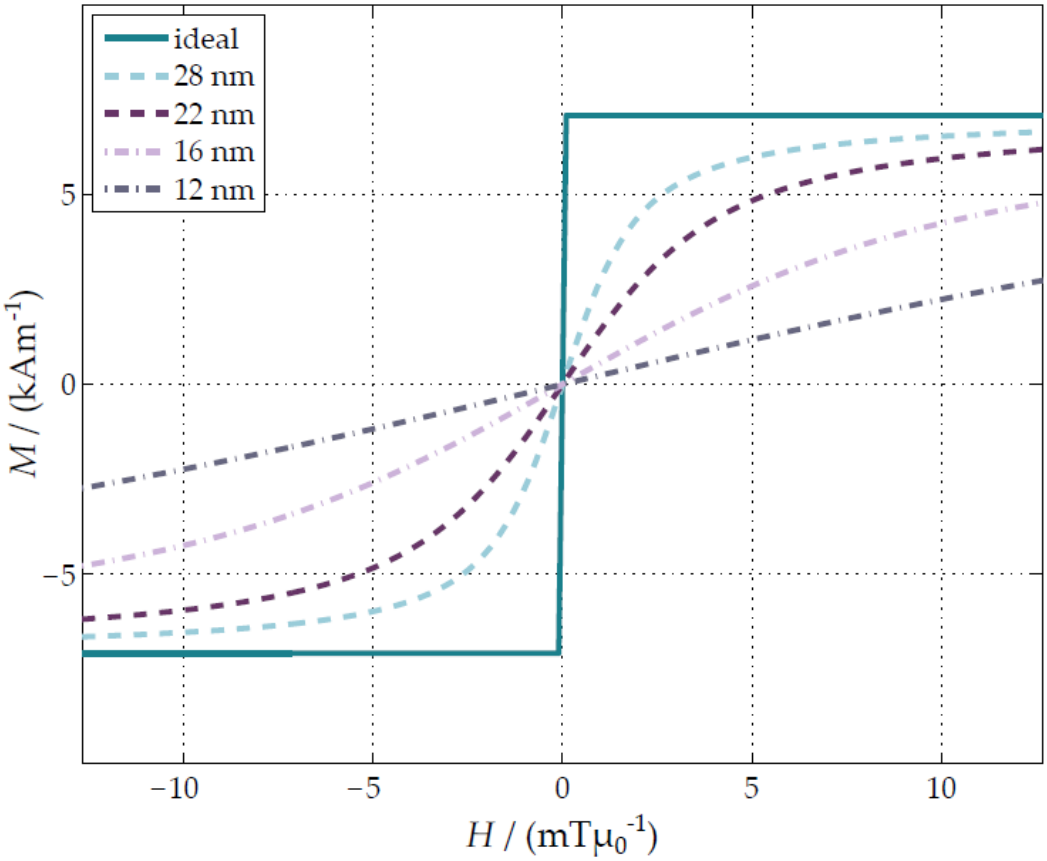

Figure 6. Magnetization curves for different particle core diameters [ERB14].

The simple particle model using Langevin's function leads to acceptable results when included in model based-reconstruction algorithms [ERB14].

2.3.4 Derivative of the Magnetization

Besides the Magnetization curve another way to evaluate the dynamic region of the magnetization is by the full width at half maximum (FWHM) of its derivative, i.e. the width at which a kernel function decays to 50% of its maximum. In this case kernel function is the derivative of (2.12)

$$\frac{d\vec{M}}{d\vec{H}} = c\vec{m}\mathcal{L}(\beta) \tag{2.16}$$

with

$$\mathcal{L}(\beta) = \begin{cases} \frac{1}{\xi^2} - sinh^2\xi & \xi \neq 0 \\ \frac{1}{3} & \xi = 0 \end{cases} \tag{2.17}$$

The FWHM for the derivative of the Langevin function is approximately 4.16, thus the FWHM of the derivative of the magnetization is given by

$$\Delta H^{FWHM} = \frac{4.16 K_B T_p}{\mu_0 m} \tag{2.18}$$

Furthermore, in order to evaluate the steepness of the Magnetization curve the highest slope or else the peak of the derivative of the magnetization at zero field strength can be exploited. That is

$$M'(0) = cm \frac{\mu_0 m}{3 K_B T_p} \tag{2.19}$$

2.4 Relaxation effects

In reality the magnetization behavior of a ferrofluid is not that simple since anisotropy and relaxation effects occur.

There are three main anisotropies in magnetic particles. Crystal anisotropy is a result of different potential energies in different magnetization directions relative to the crystal lattice. Shape anisotropy leads a single domain particle to be energetically more favorable to be magnetized in the direction of the largest elongation. The last one is called induced anisotropy and occurs if the magnetic material is mechanically stressed, however in a suspension of nanoparticles like those in MPI, it does not have an important effect [GLE13]. Consequently, in a realistic ferrofluid, when a time-varying external magnetic field is applied, the particle magnetization vector will not instantaneously follow the direction of the applied field. The change in the magnetization magnitude will also occur with a little delay compared with the change in the magnetic field strength. This results in a finite relaxation time τ and an open hysteresis loop in the magnetization curve. Due to relaxation, the magnetic moment of an SPIO particle does not directly follow the direction of the external magnetic field thus applying a static magnetic field to a distribution of SPIO particles will lead to a remanent magnetization after the deactivation of the field. The magnetization of the system will decrease exponentially

$$M(t) = M(0) e^{\frac{t}{\tau}} \tag{2.20}$$

where:
M(t) is the absolute value of the remanent magnetization with respect to time t and
M(0) is the magnetization of the system at the time of field deactivation and
τ is the relaxation time [ERB14].

There are two different relaxation processes present in an SPIO nanoparticle suspension. The Brownian process which is also called the fast process and the Néel process or slow process [GLE13], [ERB14].

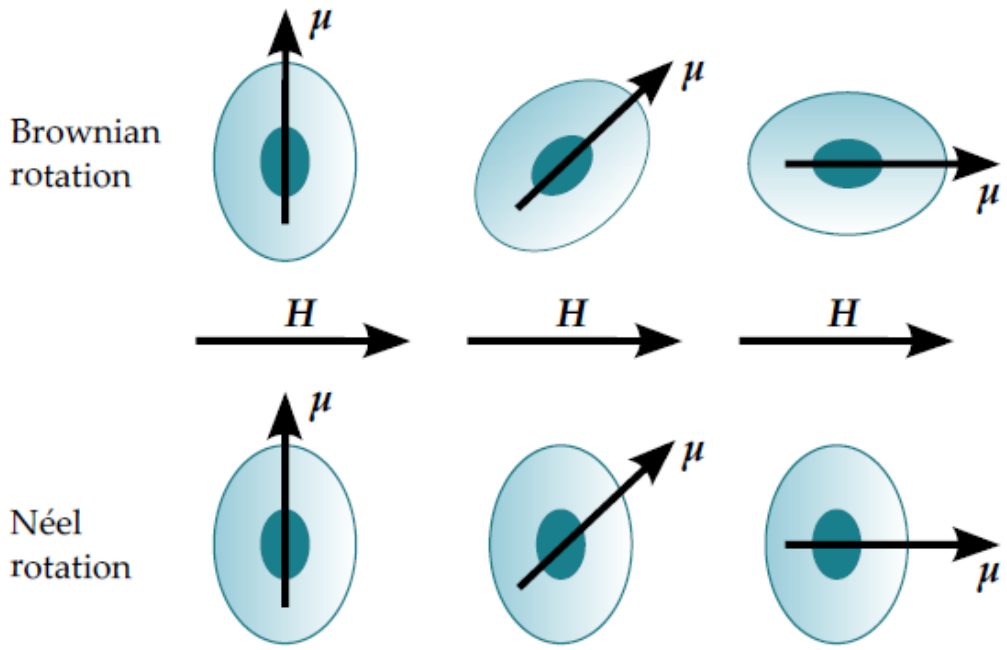

Figure 7. The Brownian and the Néel relaxation of SPIO particles. [ERB14].

Brownian rotation represents a physical rotation of the particle including its magnetic moment. Brownian relaxation describes the effect deriving from this rotation of the particle with a settled direction of its magnetic moment (Figure 7. upper row) [ERB14]. The relaxation time for the Brownian rotation is determined

$$\tau_{Brown} = \frac{3\eta V_{hydro}}{K_B T_p} \tag{2.21}$$

where:
V_{hydro} is the hydrodynamic volume of the SPIO particle and
η is the viscosity of the ferrofluid.

Néel rotation is related to the rotation of the magnetic moment of a particle. Néel relaxation describes the rotation of the magnetic moment itself, while the physical axis of the particle stays still and the corresponding time is given

$$\tau_{Néel} = \tau_0 e^{\frac{K_A V_{core}}{6 K_B T_p}} \tag{2.22}$$

where:
τ_0 corresponds to the frequency of gyromagnetic rotation and is in the order of $10^{-11} - 10^{-9}$ s^{-1}
K_A is the anisotropy constant of the ferrofluid
V_{core} is the volume of the magnetic core [ERB14].

The combined rotation could be described by an efficient relaxation time [ERB14]

$$\tau_{eff} = \frac{\tau_{Brown}\tau_{Néel}}{\tau_{Brown}+\tau_{Néel}} \quad (2.23)$$

In MPI signal main contribution comes from Néel process while the Brownian rotation seems to significantly influences the signal strength [BUZ10].

Figure 8. Fluidal sample of Magnetic nanoparticles, synthesized at the Institute of Medical Engineering of the University of Lübeck, magnetized by a permanent magnet [PAN15].

CHAPTER 3. MAGNETIC PARTICLE IMAGING-BASIC PRINCIPLES

3.1 Introduction

In this Chapter a brief reference to MPI evolution is provided. MPI basic principles are also introduced. Signal encoding, i.e., acquired information about the existence and the amount of magnetic material through the received signal is explained. First the signal generation from magnetic nanoparticles is presented. After being excited by electromagnetic fields, characteristic signal due to their magnetization change is produced and detected by receive coils, signal reception and the signal spectrum is further discussed. Another basic concept of MPI that is presented, is spatial encoding, this is the determination of where the signal comes from referring to the object under examination. Spatial encoding is feasible by making the emitted particle signal spatially dependent.

3.2 Evolution of MPI

MPI was invented at the Philips Research Laboratories in Hamburg by Bernhard Gleich in 2001 [KNO17]. Based on his initial idea in cooperation with Jórgen Weizenecker, the first 1D prototype suitable for tomographic imaging was developed in 2005 leading to the first publication on MPI. After publishing first phantom results, providing a proof of principle [GLE05], MPI became field of research of global interest and experienced rapid development since.

In the early stages resolution in the submillimeter range was achieved but acquisition time of the scanner was about several minutes or an hour. The slow data acquisition was a result of the mechanical movements needed to form a 2D image and the high tracer concentration of the phantom, which was several orders of magnitude higher than clinically approved [KNO12], [WEI09]. Later on, in 2008, mechanical movement was replaced by dynamic spatial encoding, using a 2D Lissajous trajectory, leading acquisition time to a significant reduction. The frame rate of 25 frames per second that was achieved, provided evidence of real time capabilities of MPI [GLE08]. In order to improve sensitivity Weizenecker *et al.* proposed a new encoding scheme, that used a field-free line. However, the currents' magnitude that were used were unfeasible in practice [KNO12].

In 2009, the scanner extended to a 3D system with a temporal resolution of 46 frames per second proving that MPI is capable of 4D imaging. In 2009 based on this system, the first 3D *in vivo* data were published, exhibiting the beating heart of a mouse. Using an

especially designed wide-band, low-noise amplifier, in order to convert the low-voltage measurement signal into the input range of the analog-digital converter provided a significantly improved sensitivity while tracer concentration was within the clinically approved range. In the same year Sattel *et al.* developed a single-sided coil topology and presented dynamic 1D phantom images while Goodwill *et al.* introduced a method to encode the measurement signal in a narrow frequency band and manufactured a 3D scanner capable of static imaging. In 2010 Knopp *et al.* introduced model-based reconstruction and stated the foundations for a feasible coil topology for field-free line imaging. A 3D MPI scanner with a focus field to sample a large FOV was developed by Gleich *et al.* in the same year [KNO12].

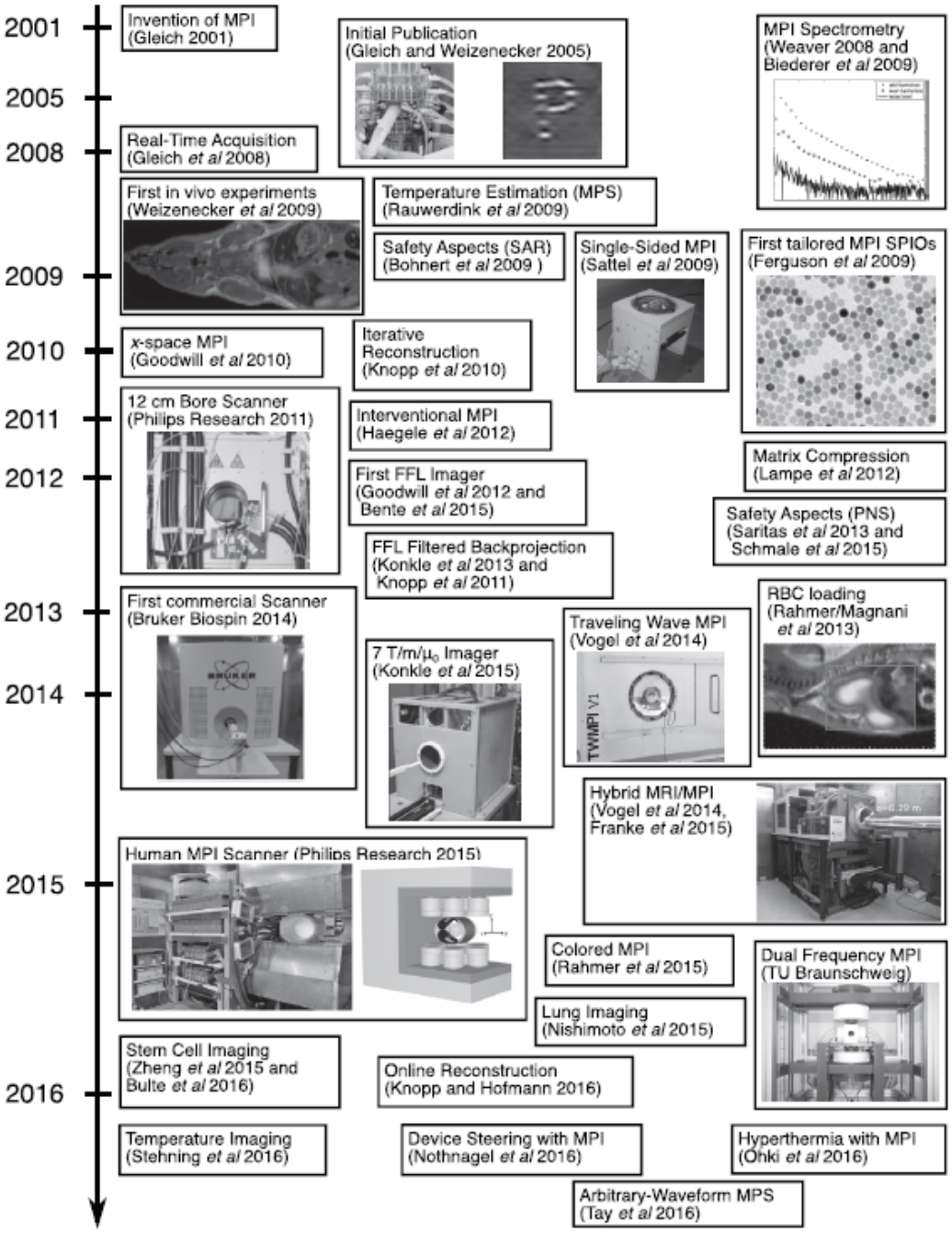

Figure 9. The evolution of MPI by [KNO12].

Many important developments regarding MPI took place in the following years such as hyperthermia with MPI and the capability of forming colored MPI images was and still is under research. MPI based technology to navigate nanoparticles in a non-invasive way has also been introduced [ZHA17]. Three dimensional commercialized systems for preclinical use by Bruker Biospin MRI GmbH in 2014 and Magnetic Insight, Inc. in 2017 were introduced. Commercial scanners for clinical use developed by Philips Healthcare, Netherlands. At least seven groups in the world operate with custom-built MPI scanners Philips, UC Berkeley, University of Lübeck in Germany, Bruker Biospin, University of Würzburg, the Technical University of Braunschweig, and Osaka University each with different scanner designs, reconstruction schemes and pulse sequences [ZHE15]. Nowadays many MPI scanners has been developed and used for research providing many modalities such as MPI/MRI hybrid or MPI/CT hybrid. Image-guided magnetic fluid hyperthermia (MFH) system for small animals is also commercially available.

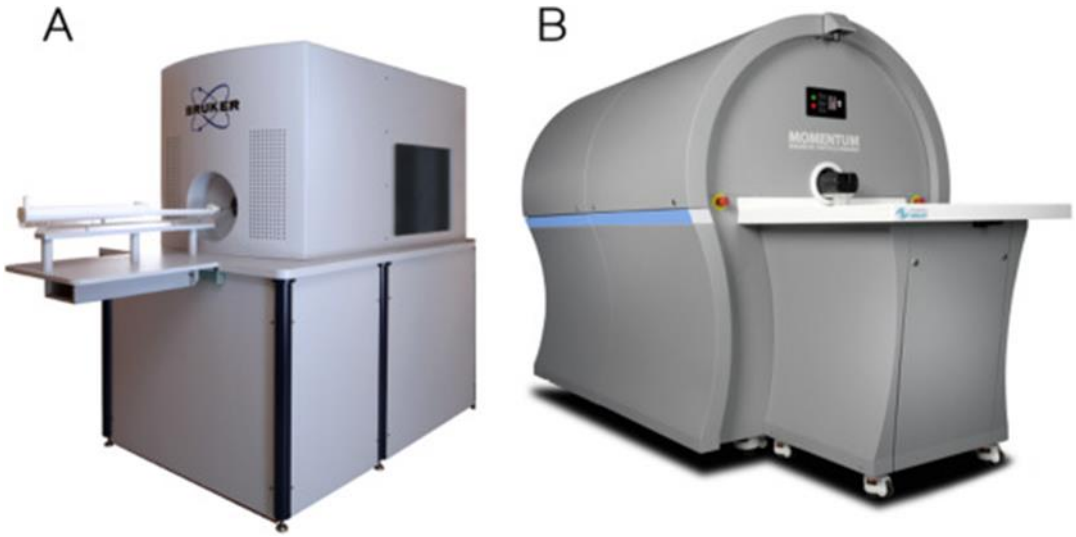

Figure 10. Preclinical MPI systems by Bruker (A) and MOMENTUM by Magnetic Insight (B) [TAL19].

Nowadays there are mainly three geometries for MPI systems as shown in figure 11.

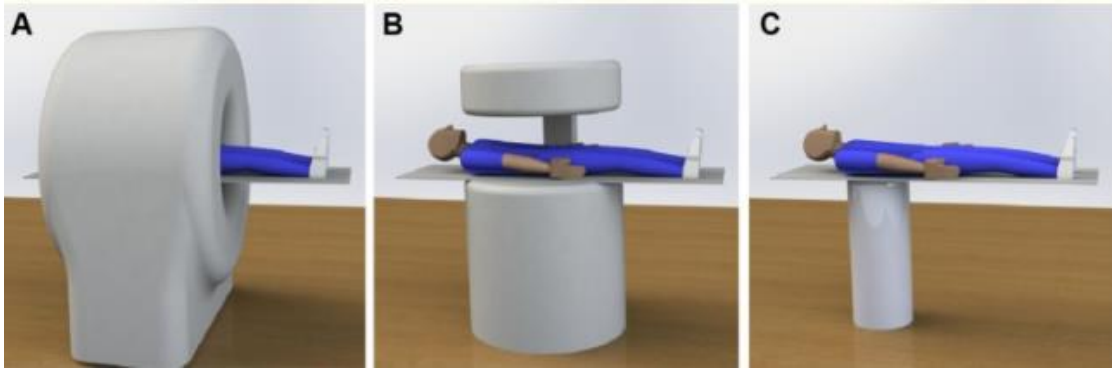

Figure 11. (A) closed-bore scanner, (B) open-bore system and (C) single-sided scanner [PAN15].

Since 2010, the MPI community has met annually at the International Workshop on Magnetic Particle Imaging and in 2015, the MPI community started its scientific research journal called the International Journal on Magnetic Particle Imaging (IJMPI) [KNO17], [KNO12].

3.3 Operating Principles of MPI

Magnetic Particle Imaging is an innovative, tracer based, medical imaging technique. The basic principle of MPI is established on the nonlinear magnetization behavior of the tracer nanoparticles.

MPI signal is generated from the response of tracer particles to applied magnetic fields. SPIO nanoparticles, described by Langevin physics, magnetically align with the applied magnetic field until they reach superparamagnetic saturation. The application of a sinusoidal external magnetic field with fundamental frequency f_0 causes a non-sinusoidal oscillation of particle magnetization [KNO10]. This change in magnetization induces a voltage in receive coils, according to Faraday's law of induction. The existence of higher harmonics in the Fourier spectrum of the measured voltage gives evidence for the existence of SPIO particles inside the volume of interest [ERB12]. Due to the linear relation between the magnetization M and the concentration c, the received signal is analog to the derivative of the magnetization and consequently to concentration c (eq 2.7). This relation makes quantification of the received signal possible.

For spatial encoding of the MPI signal, one or more gradient fields are used to achieve magnetic saturation of all SPIO nanoparticles out of a central region with almost zero magnetic field, called field field-free region (FFR) [GLE05]. Shifting FFR through the volume of interest results in the magnetization change of the SPIO nanoparticles in this area, whereas the nanoparticles' magnetization around this region reaches saturation. As a result, only particles in this specific region

contribute to the measured signal. Spatial encoding can be achieved either by implementing a Field Free Point (FFP) or a Field Free Line (FFL) technique. Field Free Line (FFL) Magnetic Particle Imaging allows reconstruction based on system function [WEI08] or Radon based algorithms [KNO11], [MED15].

3.4 Signal Encoding

As mentioned before, MPI exploits the non-linearity of the magnetization curve of the SPIO nanoparticles to enable their detection. This characteristic behavior is the nanoparticles' response to an external magnetic field.

3.4.1 Signal Generation

In MPI a spatially homogeneous, time varying magnetic field is applied to change the magnetization of the magnetic nanoparticles which leads to a voltage induction. This field is called excitation field or drive field and the frequency of this field is called excitation frequency, fundamental frequency or drive field frequency. The coils that produce the drive field are termed as transmit coils or send coils.

The induced signal from the sample can be distinguished from the external field since the magnetization does not follow the applied field proportionally. A common way to achieve this separation is by implementing a field of sinusoidal shape and search for higher harmonics in the detected signal. Thus, the drive field, is given

$$H_D = A_D \sin(2\pi f_E t) \text{ or } H_D = -A_D \cos(2\pi f_E t) \quad (3.1)$$

Where:
A_D is the drive field amplitude and
f_E is the excitation or drive field frequency.

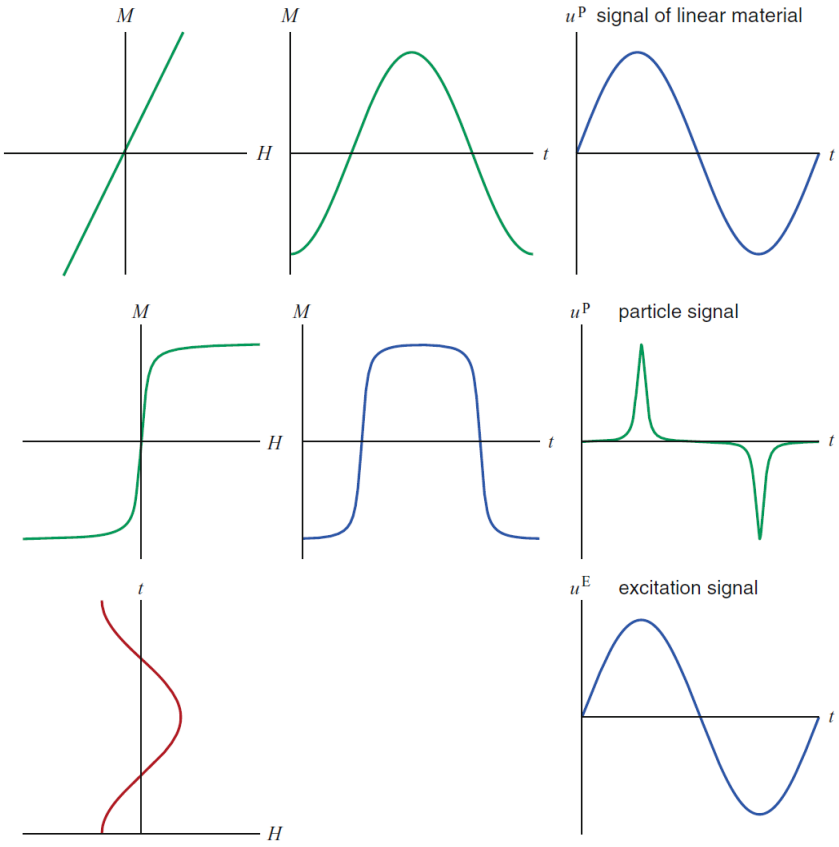

Figure 12. Excitation of particles with a linear magnetization behavior (first row) and SPIO nanoparticles (second row) by a sinusoidal magnetic field (third row). The excitation field causes a magnetization change (second row, left), which is approximately a rectangular function (second row, middle) and results to an induced voltage (second row right). The excitation signal which couples into the receive coil is also shown (third row right) [KNO12].

The sinusoidal time varying field leads to the magnetization change of the SPIO particle distribution as described by the Langevin function (2.12). In order to achieve the non-linear magnetization behavior of the SPIO particles, A_D should be high enough to lead the change in magnetization into the dynamic region of the magnetization curve, roughly into saturation region. The higher the amplitude, the more noticeable the higher harmonics in the received spectrum of the MPI will be. Amplitudes in the range of several mT/μ_0 to $20mT/\mu_0$ are achievable and most common in MPI. Even though higher amplitudes are feasible specific absorption rate (SAR) limitation arise, causing amplitude restrictions [KNO12].

The excitation field has a frequency in the range of ten to over hundreds of kilohertz. In the first publication a frequency of 25 kHz was used, that is a frequency commonly used in MPI. The excitation frequency plays an important role in the resulted signal since the noise in the receiver electronics is in many cases controlled by a factor of $1/f$ [KNO12]. If the excitation frequency is too low the intrinsic

noise of the detector, coil resistance or amplifier noise, is the main source of noise. Higher frequencies can be beneficial; however, certain physiological limitations arise when applying high frequencies, that are about peripheral nerve stimulation and energy deposition (SAR) which is proportional to the square of the field amplitude [LAW97], and frequency.

Another limitation considering the applied frequency results from the particles finite relaxation times. The drive field frequency should be considerably lower than the inverse relaxation time so that the magnetic moments of the particles will manage to follow the alternating direction of the drive field. Otherwise the intensity of the induced signal will be low due to the suppressed change of the particle magnetization.

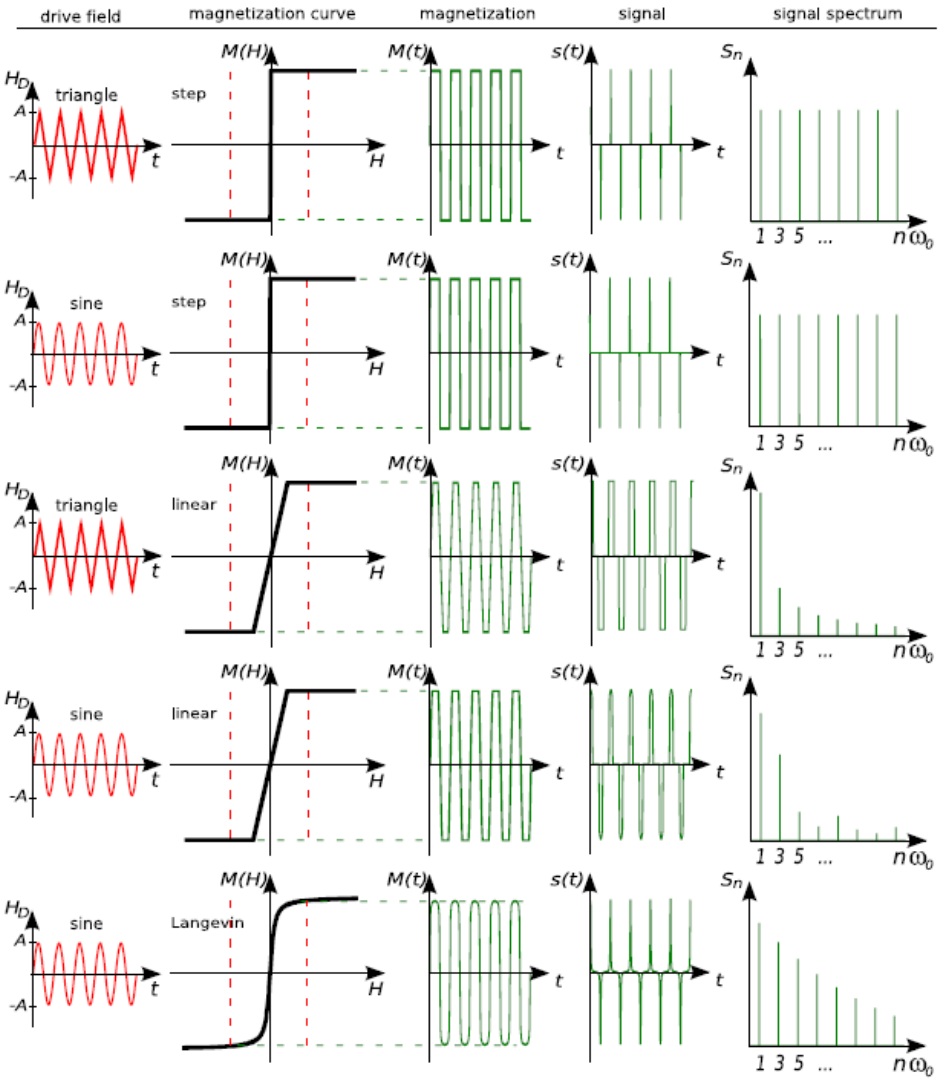

Figure 13. Particle magnetization response $M(t)$, acquired signal $s(t)$, magnitude spectral components Sn for different drive fields and particle magnetization curves [RAH09].

3.4.2 Signal Reception

Now that the signal generation has been discussed the detection method of the characteristic signal of the particles should be derived.

According to Faraday's law of induction and by using the law of reciprocity as mentioned in section 1.6.2 the voltage u_M induced by a time varying magnetization $\vec{M}(\vec{r},t)$ in a receive coil with sensitivity $\vec{p}(\vec{r})$ is given by the expression (1.44). Thus, when a distribution of SPIO particles is exposed to an external magnetic field H, voltage u_p given by (1.44)

$$u_p(t) = -\mu_0 \int_{V^M} \frac{\partial}{\partial t} \vec{M}(\vec{r},t) \cdot \vec{p}(\vec{r}) d^3\vec{r} \tag{3.2}$$

is induced in receive coils. To determine the voltage induced by the superparamagnetic nanoparticles in a receive coil an integration of the magnetization over the volume of interest needs to be done.
However, particles' signal detection is not that easy, since not only the induced voltage from the particles is picked up by the receive coils. The time-varying external magnetic field directly couples into the receive coil and induces an excitation signal

$$u_E(t) = -\mu_0 \frac{d}{dt} \oint_{\partial S} \vec{H}(\vec{r},t) \cdot d\vec{S} \tag{3.3}$$

As a result, the induced voltage in the receive coil is the superposition of the particle signal u_P induced by the time-varying magnetization and the excitation signal u_E induced by the time-varying magnetic field [GRA13], i.e.

$$u(t)=u_p(t) + u_E(t) \tag{3.4}$$

One would think that the separation of the two signal components could be done by the obvious procedure that is to measure the signal induced by the excitation field in an empty scanner, proceed to the regular MPI measurement and then obtain the particle signal by subtracting the first measurement. This is not possible in practice, since the particle signal is much lower compared to the induced signal by the excitation field. For typical particle concentrations and coil sensitivities, the particle signal is more than six orders of magnitude lower than the induced excitation signal [KNO12]. Additionally, the voltage induced by the particles' magnetization change has frequency components with an amplitude 10^{10} times lower than the excitation signal. Even advanced ADCs, which are used to convert the analog signal into a digital signal, can only determine a range of about 10^5 V.

In conclusion, it is not possible to distinguish the two signals, u_E and u_p. By a simple post-process of the data. The excitation signal must be carefully chosen so that it will be possible be filtered prior to digitization [KNO12], [STR15].

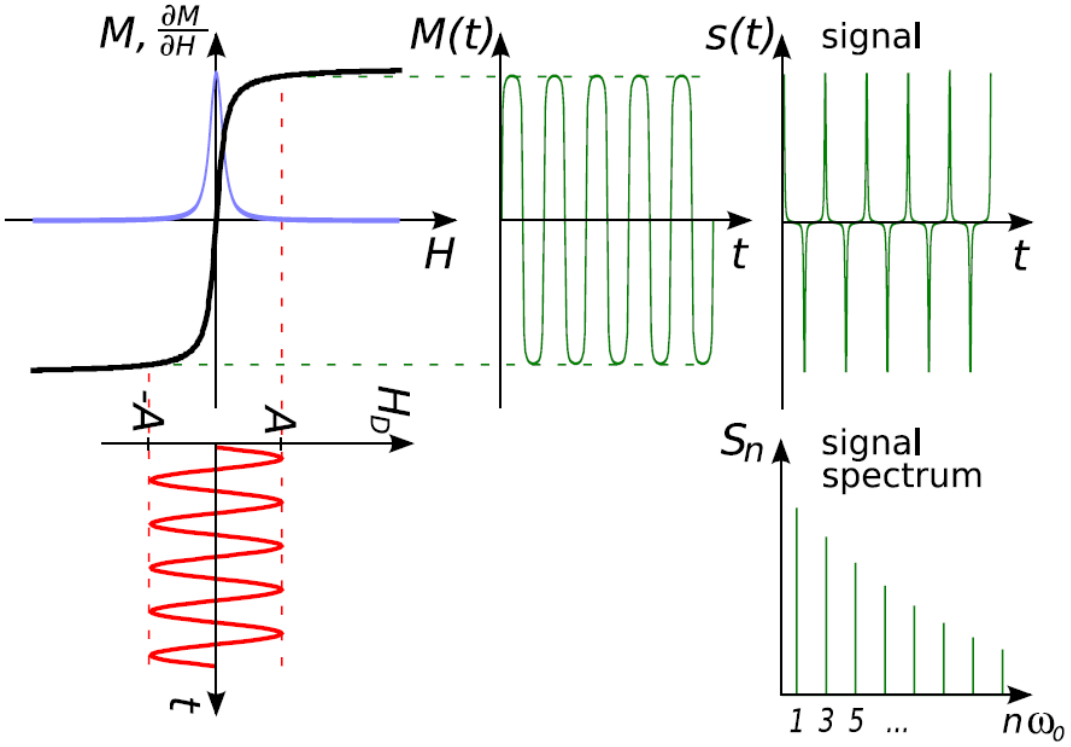

Figure 14. Particle magnetization response, $M(t)$, to a sinusoidal time-varying applied magnetic field H_D, acquired time signal $s(t)$, and magnitude spectral components Sn [RAH09].

There are some conditions related to the magnetization curve of the SPIO tracer material as well as on the external magnetic field, under of which MPI signal is positively affected.

Equation (3.2) could be simplified under the following assumptions [ERB14]:

- ✓ The external magnetic field H and the receive coil sensitivity p are homogeneous over the volume of interest V, this means there is not dependency over position r, $\vec{p}(\vec{r})=\vec{p}$ and $\vec{H}(\vec{r},t)=\vec{H}(t)$.
- ✓ The external magnetic field H and the receive coil sensitivity p are parallel over V, hence, the magnetization M will also be parallel to the receive coil sensitivity p, meaning that $\vec{M}(\vec{r},t)\cdot\vec{p}(\vec{r})$=M(t)p
- ✓ M denotes the magnetization component picked up by the receive coil, and

- ✓ The particle distribution is approximated by a δ-distribution.

Then eq. (3.2) is simplified

$$u_p(t) = -\mu_0 p \frac{d}{dt} M(\vec{H}(t)) \tag{3.5}$$

Neglecting the constant factors (3.5) is formulated

$$u_p(t) = -\frac{d}{dt} M\left(\vec{H}(t)\right) = -\frac{\partial M}{\partial H}\frac{dH(t)}{dt} \tag{3.6}$$

From equation (3.6) is shown that in order to achieve high signal the magnetization should change as fast as possible with respect to the excitation field H and the excitation field should change fast with respect to time. In other words, for high MPI quality steep magnetization curve and high excitation frequency is needed.

3.4.3 Signal Spectrum

The differences between the excitation signal and the particle signal is more obvious if one considers the signals in frequency space.

Due to the periodicity of the excitation field, both of the induced signals are periodic. The excitation signal, as a purely sinusoidal function, shows up as a single peak at the frequency f_E. Regarding the particles' signal, their non-linear magnetization behavior, results to a modulated sine response. This is why the Fourier series of the measured voltage u(t) contains higher harmonics of the excitation frequency f_E. Expanding the signal into a Fourier series

$$u(t) = \sum_{k=-\infty}^{\infty} \hat{u}_k e^{2\pi i k f_E t} \tag{3.7}$$

The spectrum consists of discrete lines which are multiples of the fundamental frequency f_E, called harmonic frequencies or harmonics (fig.14).

$$f_k = k f_E \,, k \in \mathbb{Z} \tag{3.8}$$

with the period $T_R = 1/ f_E = 2\pi / \omega$, the Fourier coefficients can be calculated by

$$u(t) = \frac{1}{T_R}\int_0^{T_R} u(t) e^{-2\pi i k f_E t}\, dt = \frac{1}{T_R}\int_0^{T_R} \left(u(t) e^{2\pi i k f_E t}\right)^*\, dt = (\hat{u}_{-k})^* \tag{3.9}$$

Negative frequencies are usually neglected in MPI as they do not carry any supplementary information.

Expanding the Langevin function into a Taylor series the higher harmonics for the nonlinear magnetization curve can be mathematically derived

$$\mathcal{L}(\xi)=\frac{1}{3}\xi-\frac{1}{45}\xi^3+\frac{2}{954}\xi^5-\frac{1}{4{,}725}\xi^7+\ldots \tag{3.10}$$

Considering SPIO nanoparticles magnetization as given by (2.12)
$\vec{M}(\vec{H},t)=c\vec{m}\mathcal{L}(\beta)$ with $\beta:=\frac{\mu_0\vec{m}\cdot\vec{H}}{K_BT_p}$ and
an excitation field $H_D = -A_D \cos(2\pi f_E t)$, 3.10 will give

$$\mathcal{L}(\tilde{\xi}\cos(2\pi fEt))=\frac{1}{3}\tilde{\xi}\cos(2\pi f_E t)-\frac{1}{45}\tilde{\xi}^3\cos(2\pi f_E t)^3+\frac{2}{954}\tilde{\xi}^5\cos(2\pi f_E t)^5$$
$$-\frac{1}{4{,}725}\tilde{\xi}^7 cos\,(2\pi f_E t)^7+\ldots \tag{3.11}$$

where

$$\tilde{\xi}=\frac{-\mu_0\vec{m}\cdot A_D}{K_BT_p} \tag{3.12}$$

Using the relation

$$cos^3(x)=\frac{1}{4}(3\cos(x)+\cos(3x)) \tag{3.13}$$

$$\mathcal{L}(\tilde{\xi}\cos(2\pi f_E t)))=\frac{1}{3}\tilde{\xi}\cos(2\pi f_E t)-\frac{1}{60}\tilde{\xi}^3\cos(2\pi f_E t)\quad+\frac{1}{180}\tilde{\xi}^3\cos(2\pi f_E t)\quad+$$
$$\ldots=\frac{20\tilde{\xi}-\tilde{\xi}^3}{60}\cos(2\pi f_E t)\quad+\frac{\tilde{\xi}^3}{180}\cos(2\pi\,(3f_E)t) \tag{3.14}$$

It is now obvious that except the excitation frequency the third harmonic $3f_E$ is present in the spectrum of the induced voltage for a sinusoidal excitation. In this way one could validate that all the odd harmonics are present in the signal spectrum with most of the signal content being in the excitation frequency and third harmonic [GLE13], [FIC15].

3.5 Spatial Encoding

The signal produced by the particles when they are exposed to the drive field indicates the existence of SPIO nanoparticles in the examined volume. Up to this point, no spatial information is provided. In order to be able to distinguish among particles at different spatial positions, a spatially varying magnetic field should be superimposed to the drive field.

In MPI spatial encoding could achieved by applying constant gradient fields, i.e. static magnetic fields, zero in the center and with a linearly increasing magnetic field strength in all spatial directions. In MPI such a field is called selection field. Selection fields enable spatial selection of a certain region, in which particles contribute to the measured signal [ERB14]. The gradient fields create a central region with almost zero magnetic field, called field field-free region (FFR) [GLE05]. The increasing magnetic field strength of the selection field should be high enough to achieve saturation of the particles' magnetization all around the FFR.

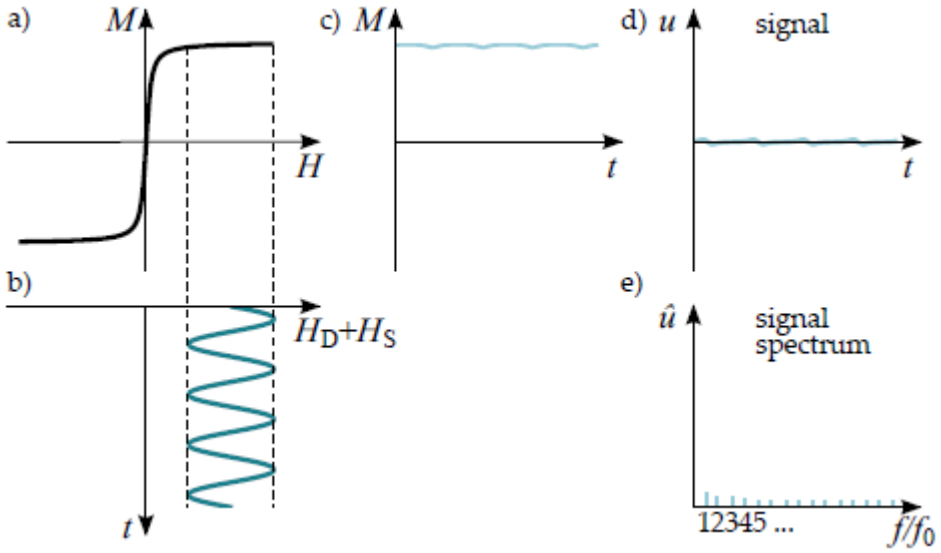

Figure 15. MPI signal generation for the superposition of the drive field and an offset field (b). The field strength is high enough to keep the SPIO particles in a state of saturation (c). Almost no signal will be detected in the receive coil (d) since the change of the magnetization over time insignificant thus no signal spectrum is observed (e) [ERB14].

Only particles close or at the FFR are able to change the orientation of their magnetic moments, meaning that only these particles will experience a magnetization change, when excited by the drive field. Each particle distribution at a specific area will lead to a specific signal, this is because the external magnetic fields applied to each distribution is different and as a result not all of these particles exhibit the same magnetic behavior. Their magnetization characteristics depend on the strength and shape of the selection field. Working on a different point on the magnetization curve of the particle distribution will lead to a different induced voltage and the signal spectrum of it as shown in figure 16.

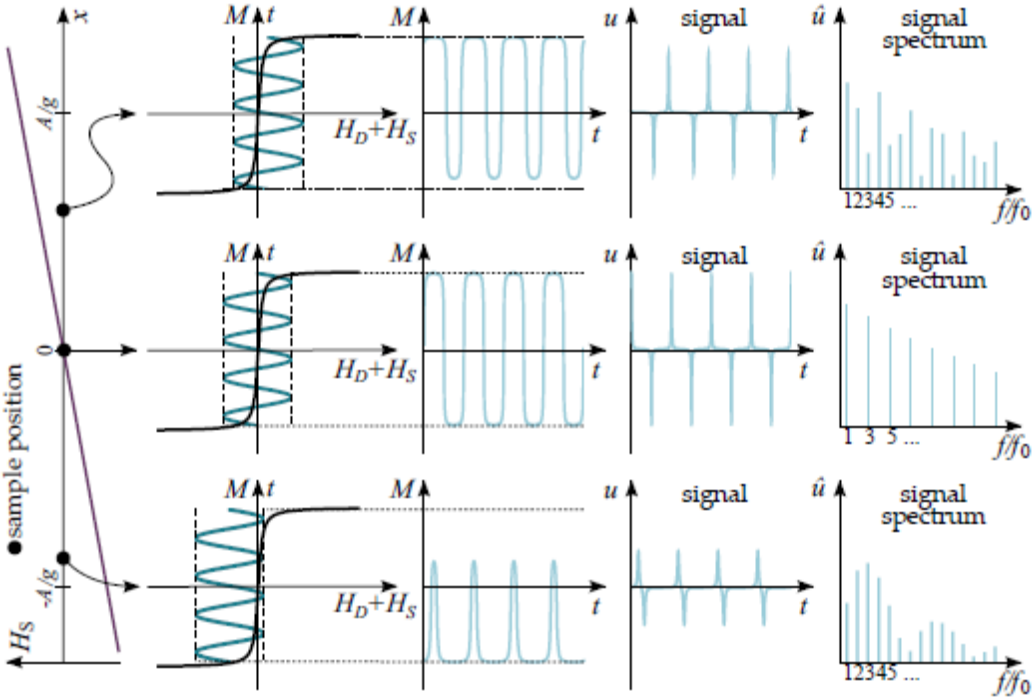

Figure 16. Spatial encoding in MPI regarding three different spatial positions [ERB14].

By moving FFR through the volume of interest, only the magnetization of the SPIO nanoparticles in this area changes. As a result, only particles in this specific region contribute to the measured signal. Spatial encoding can be achieved either by implementing a Field Free Point (FFP) or a Field Free Line (FFL) technique.

3.5.1 Field Free Region Characteristics

The gradient strength of the selection field varies in different directions the gradient strength in y-direction is $G_y := \frac{\partial \vec{H}_y}{\partial y}$ in the x-direction $G_x := \frac{\partial \vec{H}_x}{\partial x}$ and in z-direction is $G_z := \frac{\partial \vec{H}_z}{\partial z}$

Based on Gauss's law for magnetism it is

$$\nabla \cdot \vec{H} = 0 \;\Leftrightarrow\; G_x + G_y + G_z = 0 \qquad (3.15)$$

Due to (3.15) the gradient strength of the magnetic field will never be equal in all three spatial directions.

One way to fulfill this relation is to choose the gradients

$$G_z = g \text{ and } G_y = -\frac{1}{2} G_z = -\frac{1}{2} g = G_x \qquad (3.16)$$

In this case an elliptically shaped Field Free Region with its main axis on the z-direction is generated and it is called Field Free Point. The selection field can now be written

$$\vec{H}_S(\vec{r}) = \begin{pmatrix} G_x & 0 & 0 \\ 0 & G_y & 0 \\ 0 & 0 & G_z \end{pmatrix} \vec{r} = g \begin{pmatrix} -\frac{1}{2} & 0 & 0 \\ 0 & -\frac{1}{2} & 0 \\ 0 & 0 & 1 \end{pmatrix} \vec{r} = \vec{g} \cdot \vec{r} \qquad (3.17)$$

where g is the steepest gradient of the field $\vec{g} := \begin{pmatrix} G_x & 0 & 0 \\ 0 & G_y & 0 \\ 0 & 0 & G_z \end{pmatrix}$ the gradient matrix.

An FFP could be generated by a pair of permanent magnets with opposite polarity or by a Maxwell coil pair which will be discussed in chapter 4.

The size around the FFP area depends on the gradient strength g. The gradient strength should be high enough for a sufficiently small area to be formed. Additionally, as it will be explained later on, the size of the Field of View (FOV) partially depends on the size of the gradient strength. Considering a fixed field of view size, the coil pair generating the homogeneous field should be chosen as large and far away, to ensure homogeneity. The coil pair generating a gradient field should be chosen and as thin as possible to achieve gradient linearity of the field.

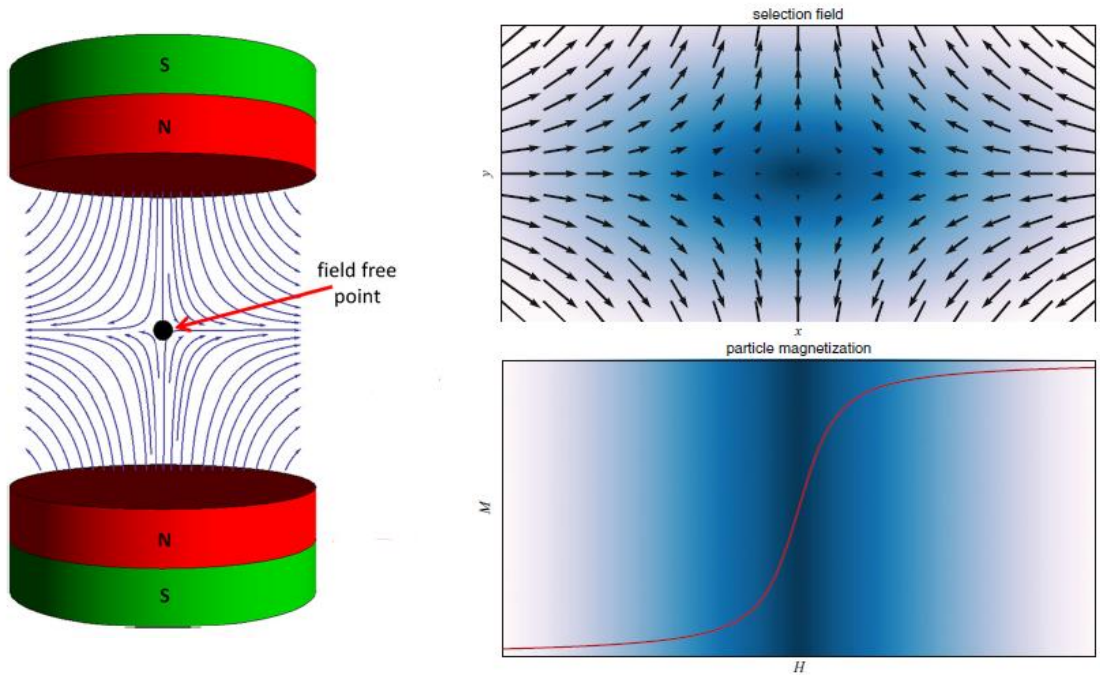

Figure 17. An FFP selection field [BOR12], [KNO12].

For small scanner devices gradient strengths of more than $10 Tm^{-1}\mu_0^{-1}$ are feasible. For a human sized scanner, the highest feasible gradient strength is about 3 $Tm^{-1}\mu_0^{-1}$ for a system realized by resistive coils or permanent magnets, while superconductors would allow for up to 6 $Tm^{-1}\mu_0^{-1}$ gradient strength [KNO12].

Another way to fulfil the relation (3.15) is to chose

$$G_z=0 \text{ and } G_y=-G_x \tag{3.18}$$

In this case a field free line along the z-direction will be generated.

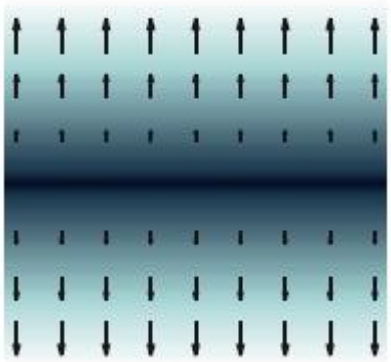

Figure 18. An FFL selection field [ERB14].

The selection field is now given

$$\vec{H}_S(\vec{r}) = \begin{pmatrix} G_x & 0 & 0 \\ 0 & G_y & 0 \\ 0 & 0 & G_z \end{pmatrix} \vec{r} = g \begin{pmatrix} -1 & 0 & 0 \\ 0 & 1 & 0 \\ 0 & 0 & 0 \end{pmatrix} \vec{r} = \vec{g} \cdot \vec{r} \tag{3.19}$$

FFP is the conventional approach used in MPI, FFP provides improved signal-to-noise ratio (SNR) since there is larger number of responsive magnetic nanoparticles in the field free region thus higher signal is produced.

3.5.2 Field Free Region movement

In order to manage data acquisition from the whole region of interest, the aforementioned should be scanned by the FFR. The movement of the FFR could be done mechanically or dynamically.

The mechanic movement refers to the movement of the object or the scanner set up. Moving the scanner set up is easily feasible in small

scanners, however, for large scanners, such as a human-sized scanner, the mechanic parts are too heavy and the mechanic movement is not that simple. One could move the examined object, for a scanner intended for humans though this would not be an option. So, even though the mechanic movement is feasible in most cases, restrictions arise.

Dynamic movement is based in the variety of current combinations in electromagnetic field generating coils and the suitable coil assembly. When applying a drive field with high amplitude the FFP moves among a line. The FFP is moved during the measurement.

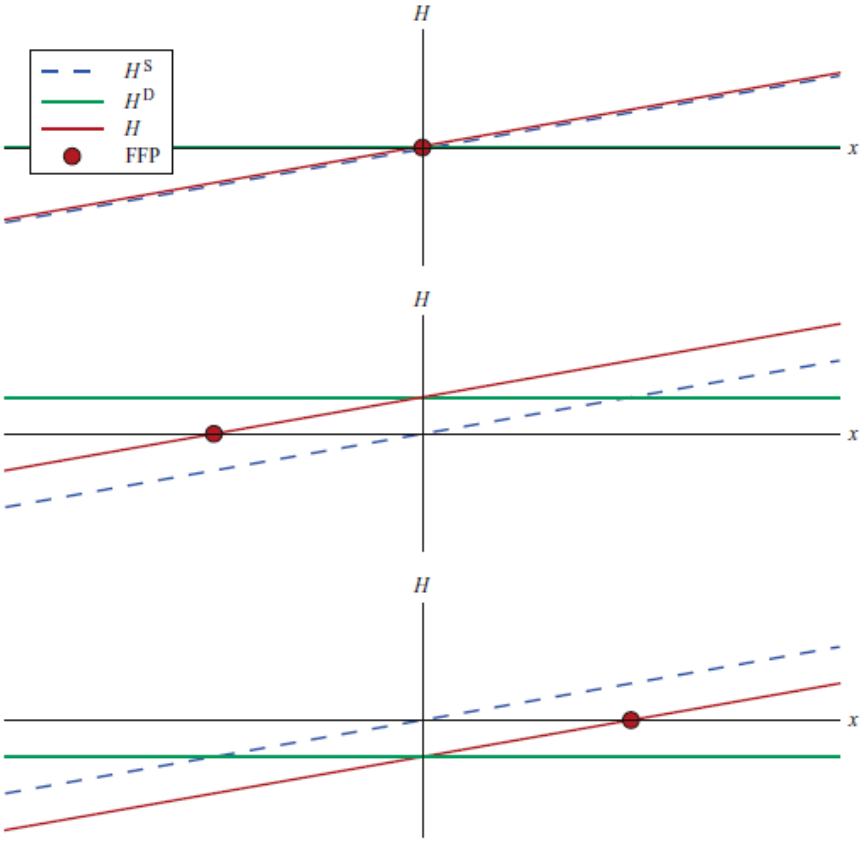

Figure 19. 1D translation of the FFP [KNO12].

Considering that the total magnetic field in x-direction is given

$$\vec{H}_x(t) = -A_x^D \cos(2\pi f_E t) + G_x x \tag{3.20}$$

For the FFP is $\vec{H}_x(t) = 0$, thus it will be located at the position

$$x^{FFP}(t) = \frac{A_x^D}{G_x} \cos(2\pi f_E t) \tag{3.21}$$

The FFP oscillates on the x-axis along a line within the interval

$$\left[-\frac{A_x^D}{G_x}, \frac{A_x^D}{G_x}\right] \quad (3.22)$$

For a 2-dimensional movement of the FFP an additional coil pair in the y-axis generating homogenous time-varying field could applied. Consequently, the FFP trajectory depends on the currents $i_x(t)$ and $i_y(t)$ applied in both pairs of coils. The limits of the FOV would then be $\left[-\frac{A_x^D}{G_x}, \frac{A_x^D}{G_x}\right]$ in x-direction and $\left[-\frac{A_y^D}{G_y}, \frac{A_y^D}{G_y}\right]$ in y-direction. The FFP has its highest speed at the center of the FOV and its lowest speed at the edges as a result image quality can be slightly higher in the center [KNO09].

There are different trajectories an FFP could follow such as the Lissajous, Cartesian, Cartesian improved, Radial and Spiral trajectory. Lissajous trajectory is most commonly used as it is found to be more efficient considering both image quality and hardware requirements.

In the early beginning of MPI single-voxel MPI method was also used for the sampling of the volume. By moving either the object or the FFP in space, different voxels in space could be selected, measurements were taken in one voxel at a time. For dynamic movement of FFP the amplitude of the drive field should be sufficiently low in order to ensure that the FFP will stay within an image voxel. This kind of measurements resulted in high acquisition time of samples of very limited size or in very coarse spatial sampling of the object, thus single-voxel MPI is not the preferred method.

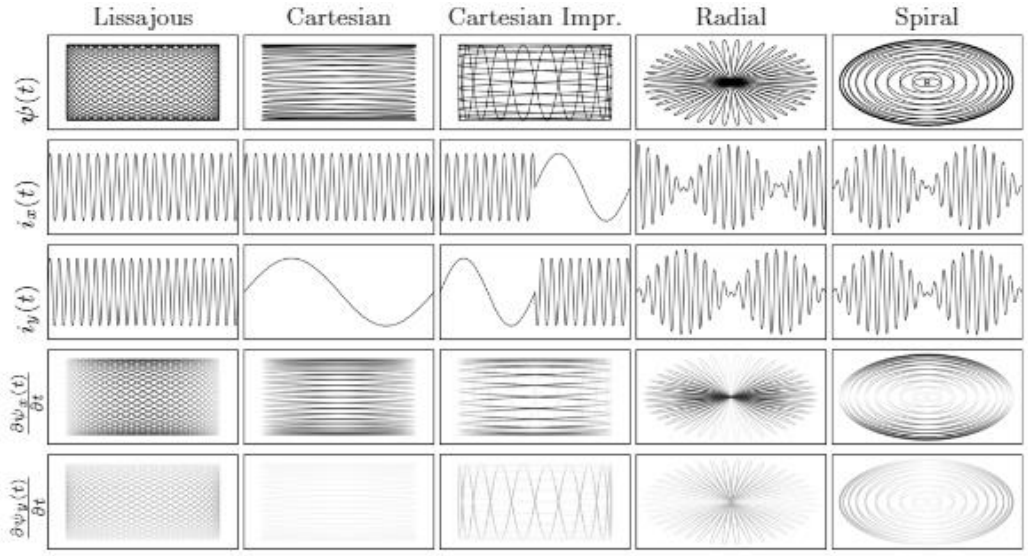

Figure 20. FFP-trajectories for sinusoidal excitation, the corresponding currents in the drive field coils, and the trajectory speed in the x-and y-directions encoded as gray values, where dark values denote fast and bright values slow FFP movement [KNO09].

For FFL imaging both mechanical and dynamic movement of the FFL could be applied, in any case rapid translation as well as 180◦ rotation of the FFL with respect to the object is required for the reconstruction of the object. In the case of dynamic movement, the rotation is feasible only by applying appropriate currents in the field generating coils. Rotation of the FFL is possible when suitable coil set up is used, an example shown in fig.21, and the translation of the FFL is realized in a similar way as in FFP imaging.

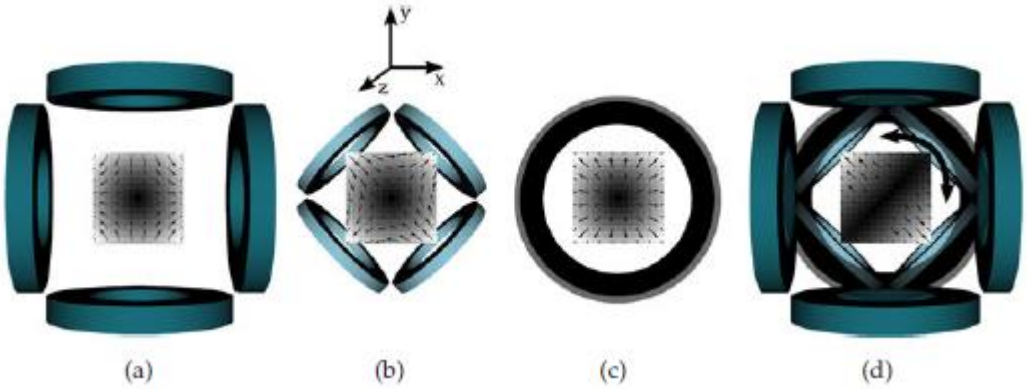

Figure 21. The superposition of the three fields, generated by setup (a), (b) and c provides a rotating FFL field. The combination of these three components adds up to setup (d) [ERB14].

An example of an FFL generation rotation and translation as provided by [ERB14] will be presented in more detail and followed by a simulation in chapter 4.

Figure 22 shows some of the FFL trajectories Radial trajectory, Spiral trajectory, Uniform Spiral trajectory, Flower trajectory, Lissajous trajectory.

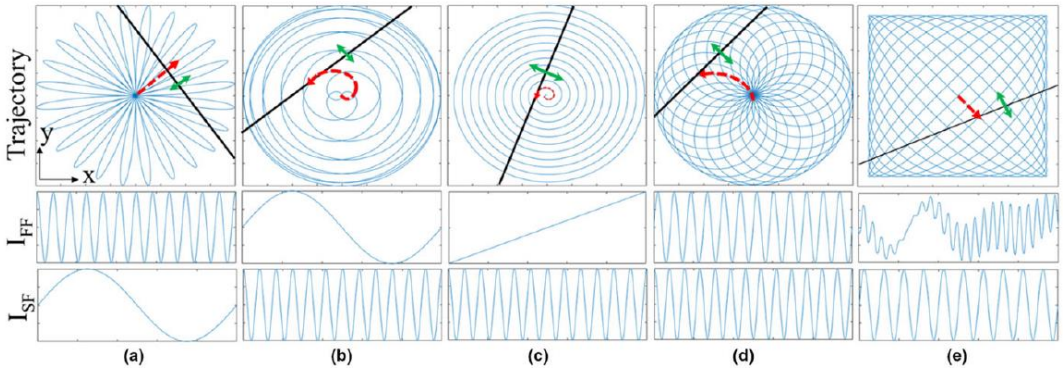

Figure 22. FFL-trajectories for sinusoidal excitation [TOP19].

3.5.3 The Focus Field

For a drive field with field strength about $20mT\mu_0^{-1}$ at 25 kHz, which is commonly used in MPI, the field of view (FOV) according to (3.22)

would be too small for medical applications. For a selection field of $2T\mu_0^{-1}$ m^{-1} the FOV would be roughly 2 × 4 × 4 cm^3 [GLE13]. An obvious solution to enlarge the FOV would be to increase the field strength of the drive field, even though this is feasible, in practice drive field strength could not exceed $20mT\mu_0^{-1}$ since fields of several hundred mT μ_0^{-1} at frequencies 25kHz or more could result to SAR values above the acceptable limits and lead to peripheral nerve stimulation. For that reason, the Focus Fields were introduced.

Focus fields are a set of orthogonal homogeneous fields applied in addition to the drive field. These homogeneous fields move the field free point combined to the drive field and should be quite strong, about 200 to $300mT\mu_0^{-1}$. To remain within the physiological limits, the increase in amplitude has to be compensated by a decrease in frequency. The frequency of the focus field is in the area of a few Hertz and can not be used for imaging.

The movement of the FFP could be done in a multi-station mode or a continuous mode. In multi-station mode the focus field is used to move the whole volume that is covered by the drive field, called cuboid or patch, to a certain position within the FOV. Continuous mode combines a simultaneous variation of both, the focus and the drive field, to produce a continuous movement of the FFP, in contrast to the multi-station mode, the resulting image is rather one complete image that covers the volume of interest than a combination of small patches [KNO12].

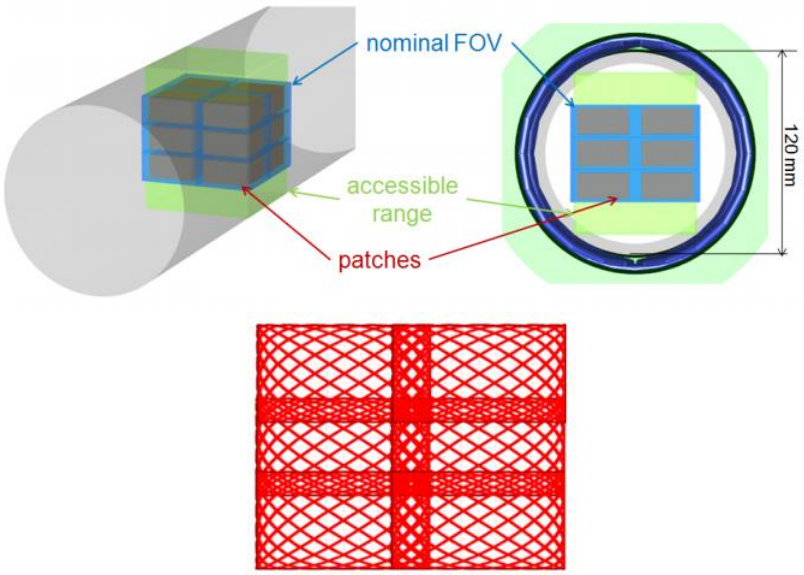

Figure 23. Several patches, as generated by drive-field induced movement of the FFP, stacked together by a slowly varying focus-field for encoding an extended FOV (up). For visualization, the patches are drawn smaller than they are. The overlapped patches (down) [SCH15].

CHAPTER 4. COMSOL MULTIPHYSICS SIMULATIONS

4.1 Introduction

In this chapter a brief mention in COMSOL Multiphysics software platform and the basic concept of setting up a simulation in the platform is provided. Simulation results using COMSOL Multiphysics for generating and evaluating magnetic fields of Helmholtz and Maxwell coil pairs are presented. A simulation of two MPI scanner topologies, one for FFP and one for FFL encoding scheme, was also conducted and simple trajectories of the respected field free regions are presented. At last, the results of simulating the superparamagnetic behavior of SPIO nanoparticles using Langevin's model, are discussed.

4.2 COMSOL Multiphysics

COMSOL Multiphysics is a general-purpose software platform for modeling and simulating scientific and engineering problems via finite element analysis.

In COMSOL Multiphysics Core package there are two main components, the Model Builder and the Application builder. Model builder is the tool where one can set up, build, compute a model and analyze the results. The Application builder allows to turn the created model into o simulation application with a specialized user interface that is easy to use. The Application Builder provides two important tools for creating applications, the Form editor and the Method editor. The Form editor includes drag-and-drop capabilities for easily accessing and including user interface components. The Method editor is a programming environment that allows the modification of model represented by the model object data structure.

The platform product can be used on its own or expanded with the several add-on modules provided for simulating across a wide range of different areas. Electromagnetics, structural mechanics, acoustics, fluid flow, heat transfer, and chemical engineering modules are available. Any of these could be coupled to one another to simulate a Multiphysics model. Every module comes with specialized physics interfaces and boundary conditions for the respected area. Additionally, there are several multipurpose modules as well as interface modules that enable to interface with external software, such as a CAD program.

To set up a simulation, after opening the software, there are two options to choose from, the Model Wizard and the Blank Model. Model wizard provides a guided approach.

After choosing the Model Wizard one should select the space dimension that wants to work on that is 0D, 1D, 1D Axisymmetric, 2D, 2D Axisymmetric or 3D.

Then the Select Physics window will open and so the physics that is planned to be included in the simulation should be selected, for example AC/DC, Electrochemistry, Acoustics, Fluid Flow, Heat transfer, etc.

The next step is to select the preferable study type for the model analysis. There are several options such as stationary, time dependent, frequency-domain study, etc.

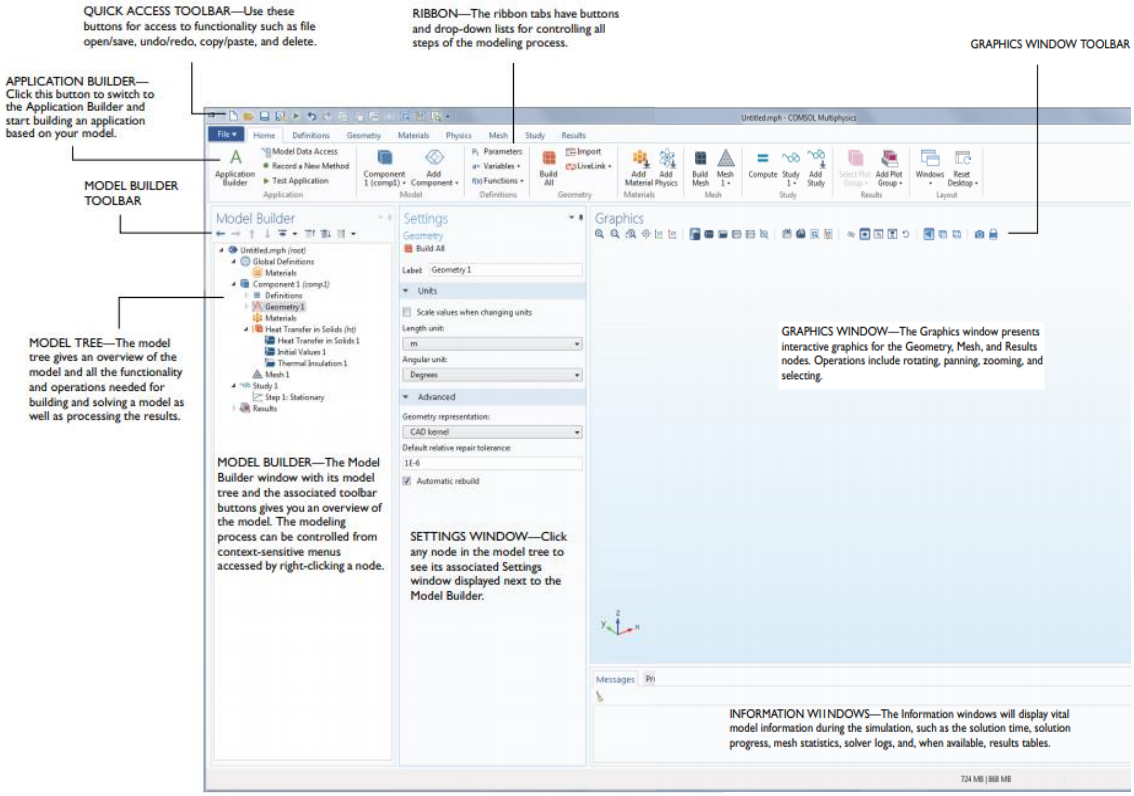

Figure 24. COMSOL desktop using Model Builder [COM].

After selecting and adding the study, COMSOL desktop appears as shown in figure 24. The model can be constructed either by using the Model builder toolbar or the Ribbon. The Ribbon enables quick access to available commands and complements the model tree in the Model Builder window. Now one can create definitions such as variables, parameters, function etc., create or import the model geometry, set up

the physics where the option to work with customized equations is provided, chose the desired material for the model or even create one, built up the mesh and compute. Post processing of the results is also available.

The Blank Model option will open the COMSOL Desktop interface without any Component or Study. By right-clicking the model tree one can add a Component of the desired space dimension, a physics interface, or a Study.

4.3 Simulation of a Helmholtz and a Maxwell Coil Pair

As previously mentioned in chapter 3, the drive field applied in MPI should be homogenous in space. A way to produce a region of nearly uniform magnetic field is by using a Helmholtz coil pair. A Helmholtz coil pair consists of two identical, circular, coaxial, parallel electromagnetic coils whose midplane separation is equal to their mean radius R. Due to the geometric symmetry of the coils a field of high uniformity near their center is produced. Reduction in symmetry reduces the field uniformity.

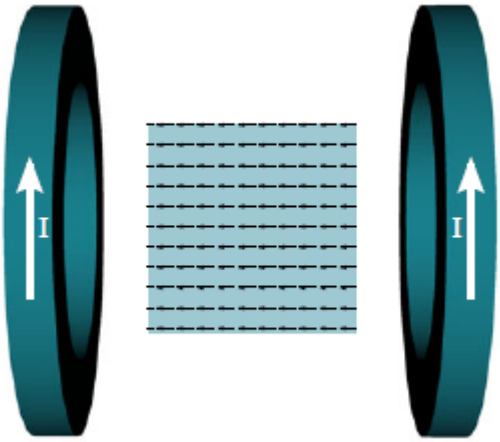

Figure 25. Helmholtz coils generating spatially homogeneous magnetic field in the central region [ERB14].

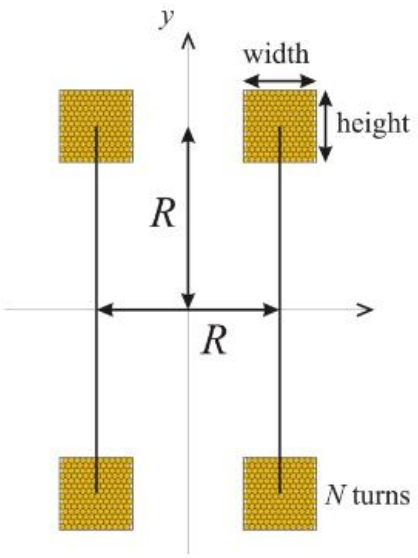

Figure 26. Helmholtz coil pair [FON19].

To evaluate the uniformity of the magnetic field produced, a Helmholtz coil pair using COMSOL Multiphysics was simulated.

A 3D model was built with the parameters seen in the table below

Coil Parameters	
I	10.820 A
R_{ext}	0.0828 m
R_{int}	0.0750 m
R	0.0789 m
Distance	0.0789 m
Width	0.0062 m
N	130 turns

Table 1.

where R is the mean radius $R = \frac{R_{ext}+R_{int}}{2}$ (4.1)
with R_{ext} and R_{int} being the external and the internal radius of the coil respectively, N the number of turns of each coil and I the current flowing in the longitudinal direction. Coils are perpendicular to Z axis as indicated in fig. 27.

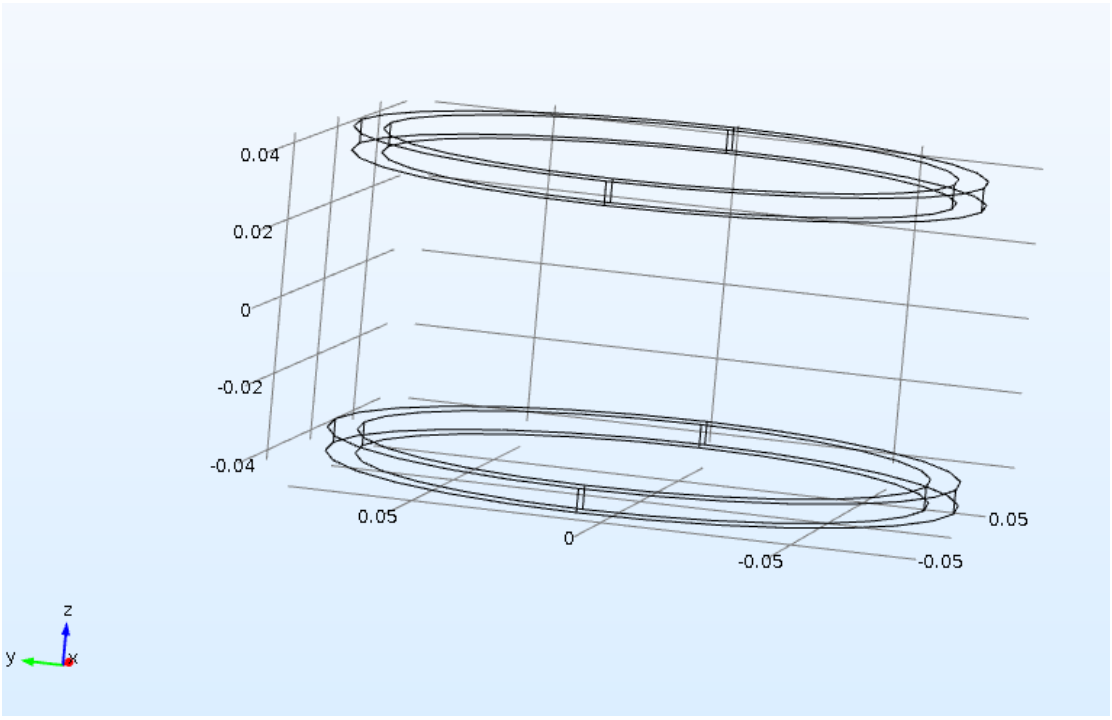

Figure 27. 3D view of Helmholtz Coil pair.

A DC current of 10.82 A was applied and the generated magnetic field is shown in fig. 28.

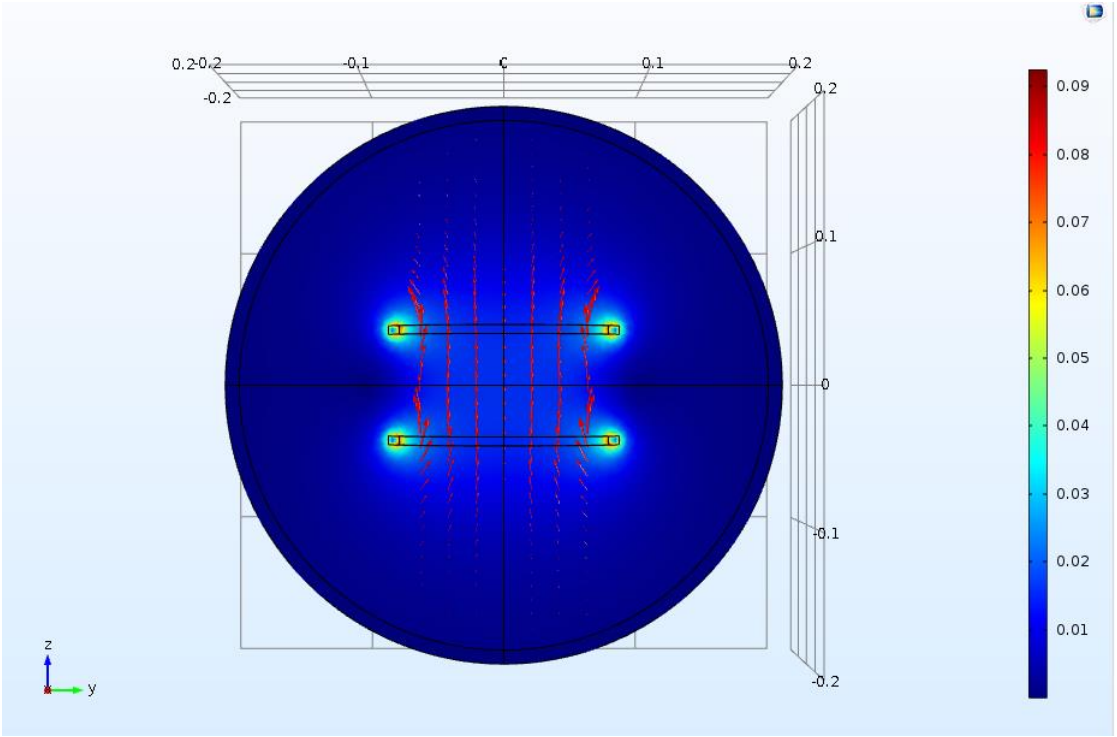

Figure 28. 2D view of generated magnetic field of the Helmholtz Coil pair in Y-Z plane. The magnetic flux density represented by color, magnetic field $\vec{H}$ represented by red arrows.

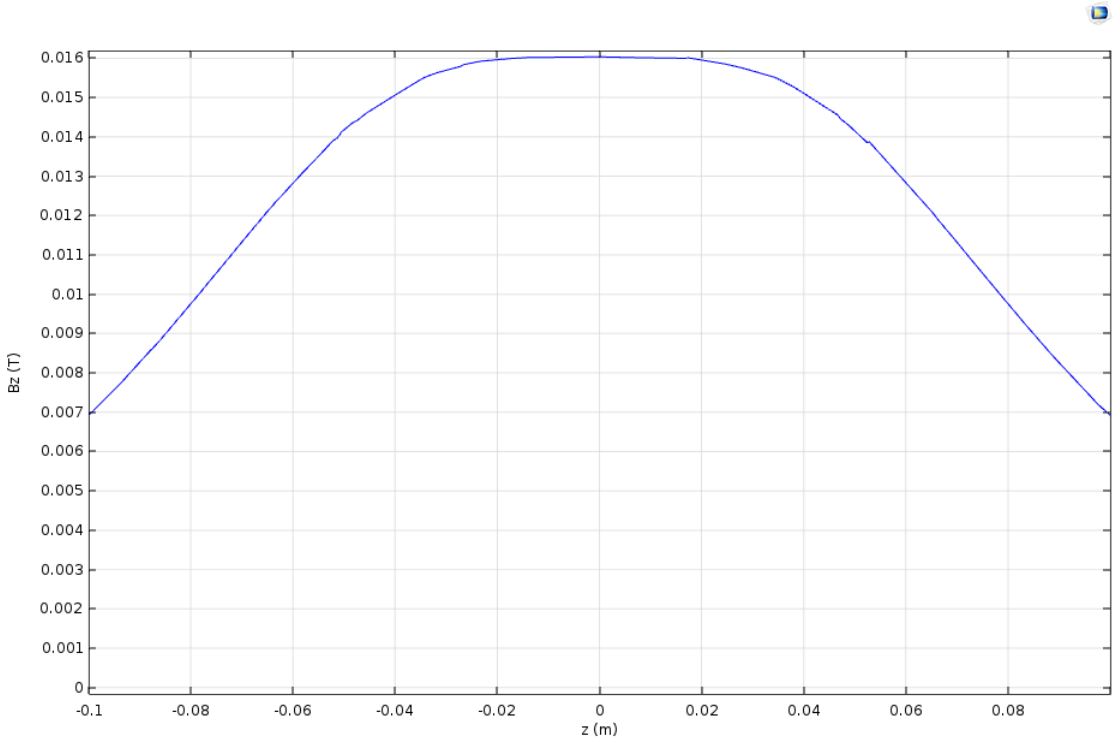

Figure 29. Z component of magnetic flux density $\vec{B}$ with respect to x axis.

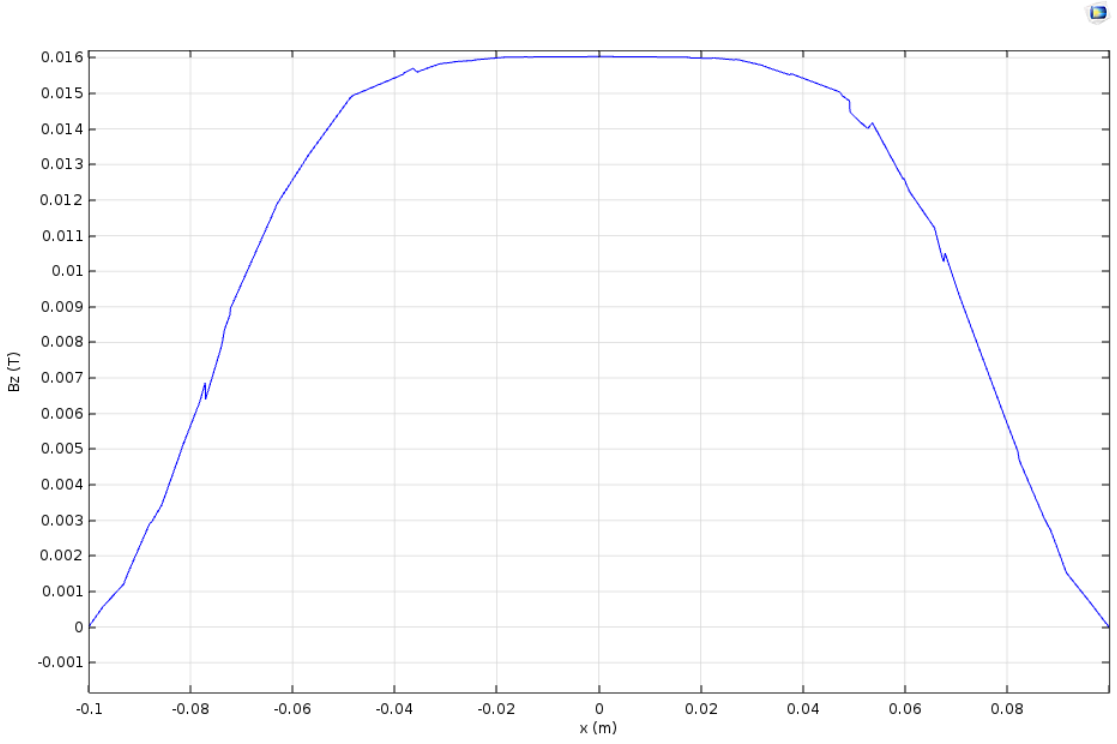

Figure 30. Z component of magnetic flux density $\vec{B}$ with respect to y axis.

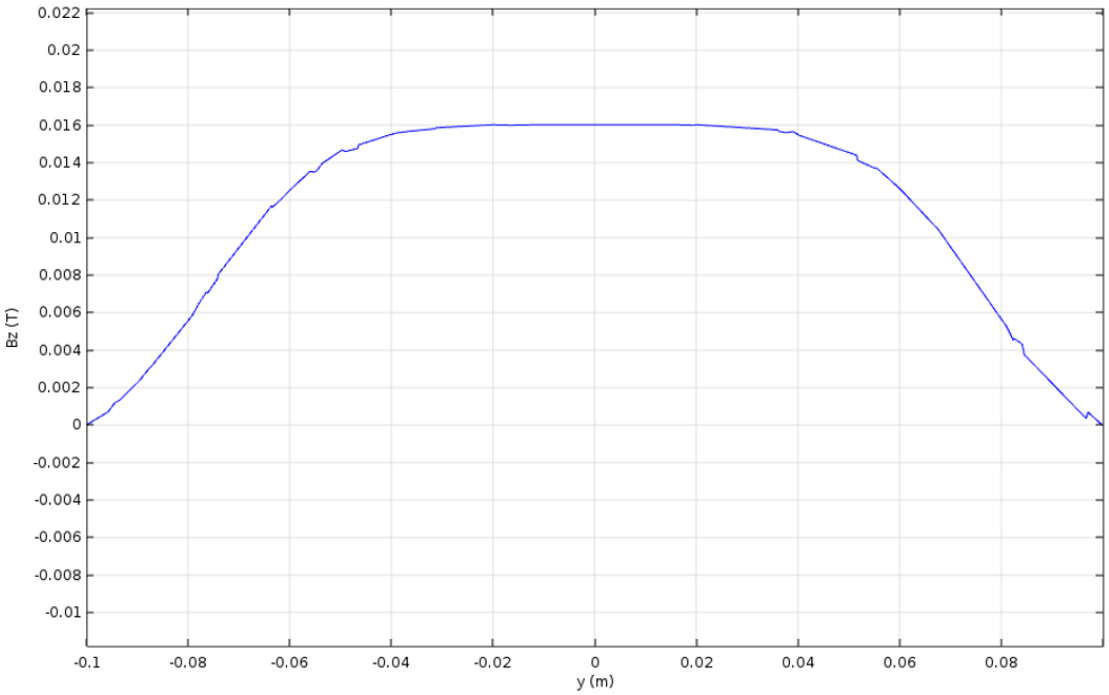

Figure 31. Z component of magnetic flux density $\vec{B}$ with respect to z axis.

As shown by the above plots, the magnetic flux density and thus the magnetic field generated from the coils is homogeneous in the central region of the coils from -0.02m to 0.02m.

An analytical expression to calculate the magnetic field produced near the center of the Helmholtz coils is given by [CRO10].

Considering ideal Helmholtz coils with width=w and height=h, perpendicular to Z axis, the Z component of the magnetic flux density in the center is approximately given by

$$B_z(0,0,0) = \frac{8\mu_0 NI}{5\sqrt{5}R}\left(1 - \frac{h^2}{60R^2} - \frac{18w^4+13h^4}{1250R^4} + \frac{31h^2w^2}{750R^4}\right) \quad (4.2)$$

The calculated magnetic field by equation (4.2) and the result from the simulation with COMSOL Multiphysics were found

	B_z(T)
Theoretical result	0.016028
Simulated result	0.016026

Table 2.

$$|B_{theor}-B_{sim}/B_{theor}|\% = 0.01\%$$

The resulted deviation is less than 1%, thus the simulation results are acceptable.

The other components of the magnetic flux density, B_x and B_y, are expected to be zero in the center of the coils. The components B_x and B_y as resulted from the simulation, were 4 orders of magnitude lower than the main component B_z. Hence it is acceptable to consider these values close to zero.

The same calculations were made for another coil pair placed with their axis along the y axis, since these coil pairs will later be used to set up an MPI scanner. The characteristics of the second Helmholtz coils are shown in table 3.

Coil Parameters	
I	10.82 A
R_{ext}	0.0456 m
R_{int}	0.0425 m
R	0.04405 m
Distance	0.04405 m
Width	0.00310 m
N	30 turns

Table 3.

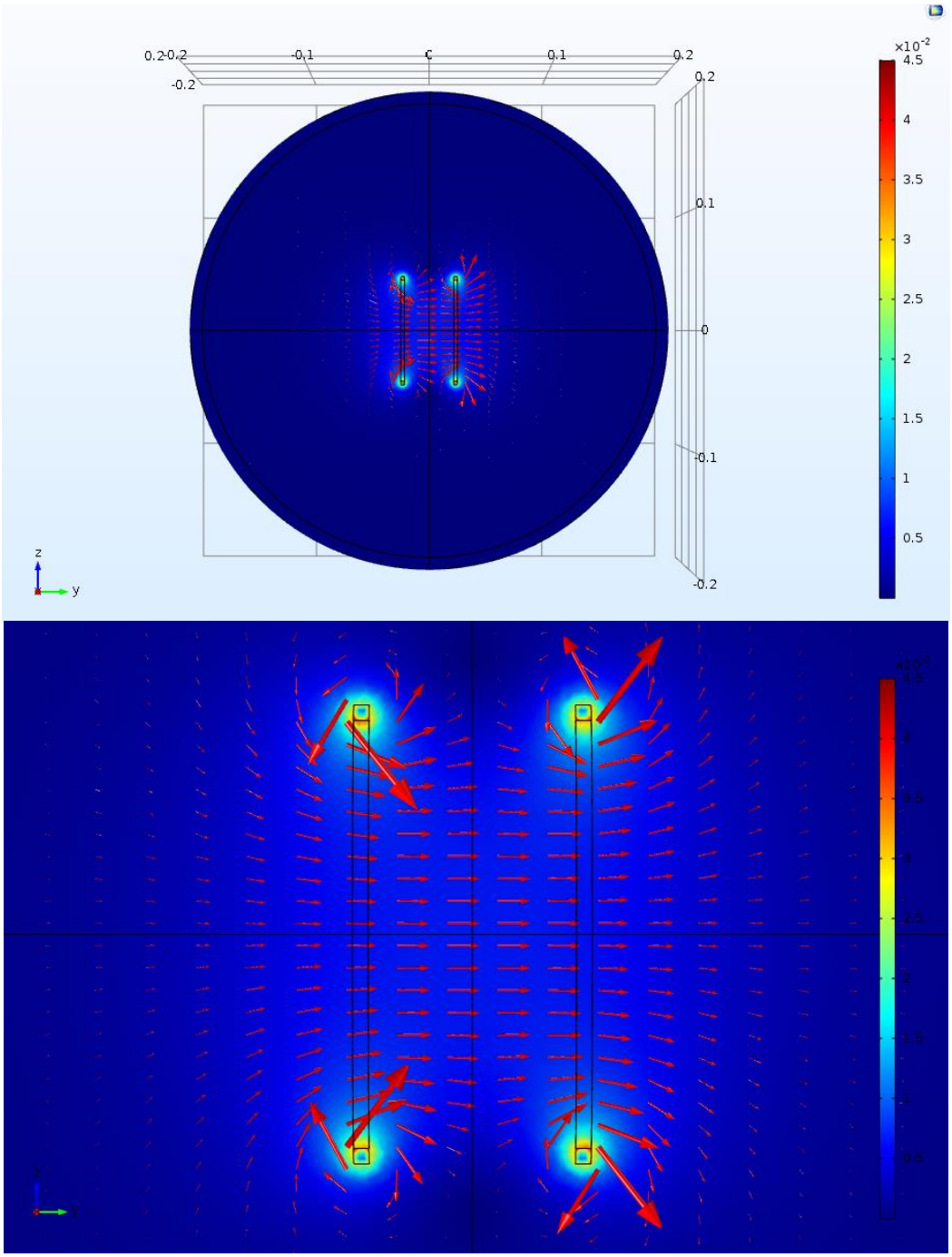

Figure 32. 2D image of generated magnetic field of the Helmholtz Coil pair in Y-Z plane. The magnetic flux density represented by color, magnetic field $\vec{H}$ represented by red arrows.

The results of the magnetic flux density calculation are shown in the following table 4:

	B_y(T)
Theoretical result	0.006625
Simulation result	0.006624

Table 4.

$$|B_{theor}-B_{sim}/B_{theor}|\% = 0.02\%$$

Again, a very small deviation between the two values derives, since the deviation is less than 1% the results are valid.

Next, a Maxwell coil pair was simulated. Maxwell coils have the same geometry with Helmholtz coils, the properties of the two coils are identical the only difference is that the current that flows in the coils is orientated antiparallel. The resulted field is not uniform but it changes linearly in space. Additionally, it can be proved that optimal linearity of the generated field is achieved when the coils are at a distance of $\sqrt{3}R$. Maxwell coils are useful for creating gradient fields; hence they are used as selection fields in MPI.

A Maxwell coil pair, as seen in figure 33., was simulated.

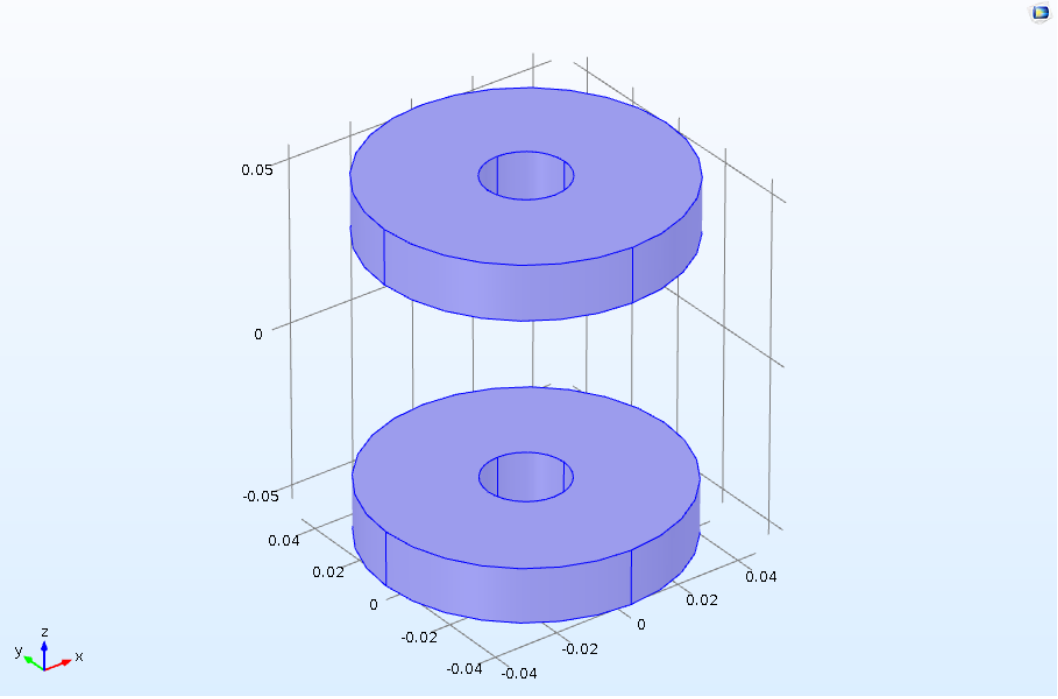

Figure 33. 3D view of Maxwell coil pair.

The characteristics of the coils are given in the following table

Coil Parameters	
I	5.41 A
R_{ext}	0.04600 m
R_{int}	0.01250 m
R	0.02925 m
Distance	0.09200 m
Width	0.01200 m
N	1000 turns

Table 5.

The vector of the z component of the magnetic field is illustrated as red arrows in figure 34, where one can observe the resulted field free region in the center of the coils.

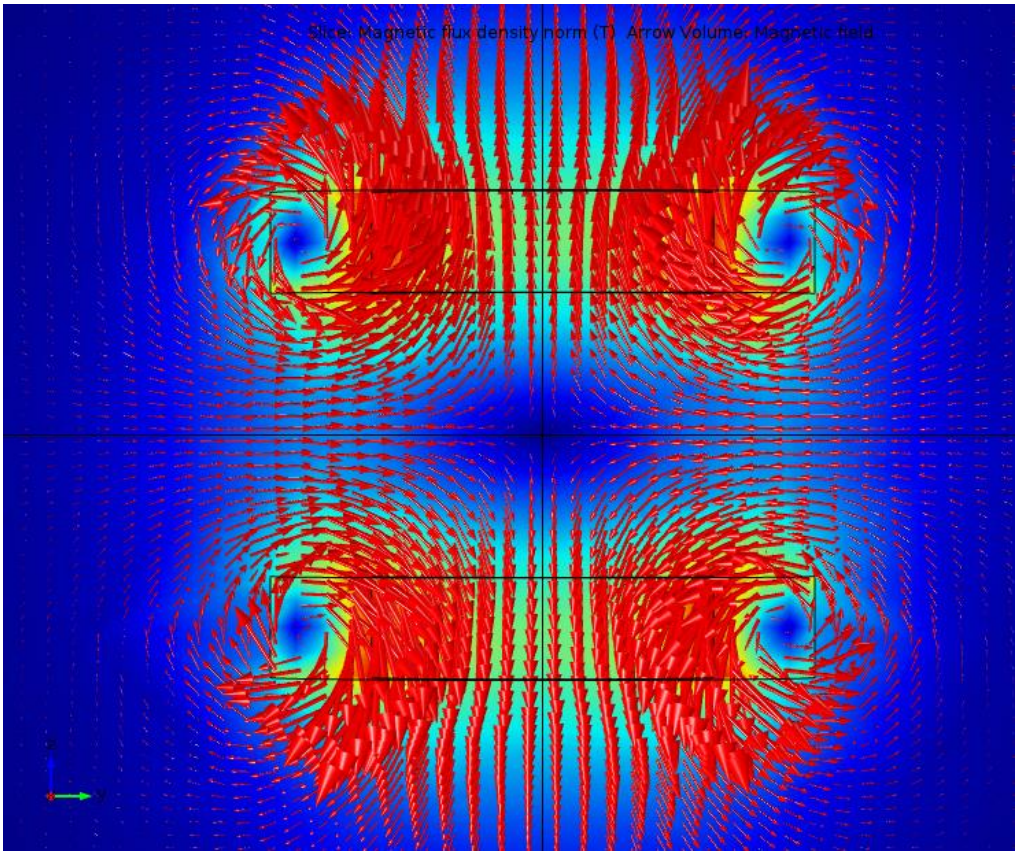

Figure 34. 2D image of the Maxwell coil pair and the projection of the magnetic flux density in Y-Z plane with the vectors of the generated magnetic field.

In the center magnetic flux density is theoretically zero, in reality is expected to be close to zero. The simulation gives a magnetic flux

density of about 10^{-4} T for the z component, and much lower for the other two components. The results are the expected.

4.4 Simulation of an FFP and an FFL MPI Scanner Topology

Subsequently, based on coil design suggested by [WAL12] for an MPI scanner, an FFP MPI scanner topology was simulated using COMSOL Multiphysics.

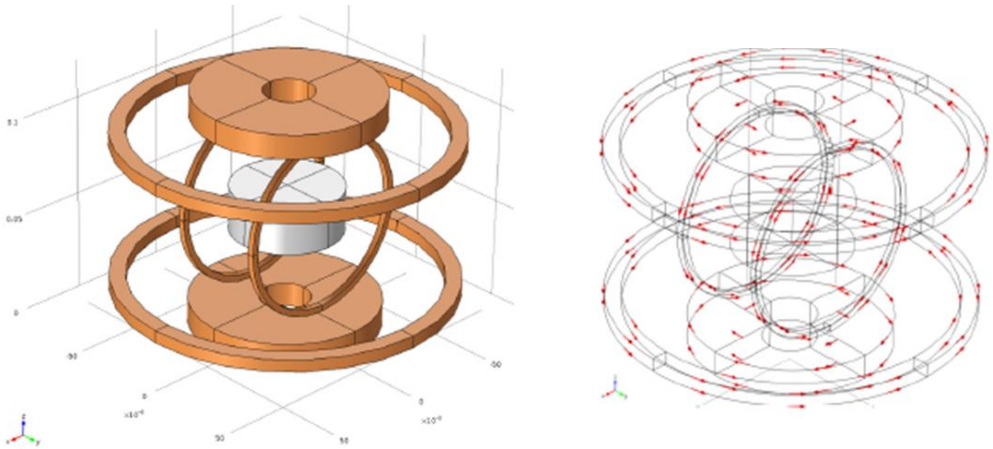

Figure 35. 3D View of coils setup by [WAL12].

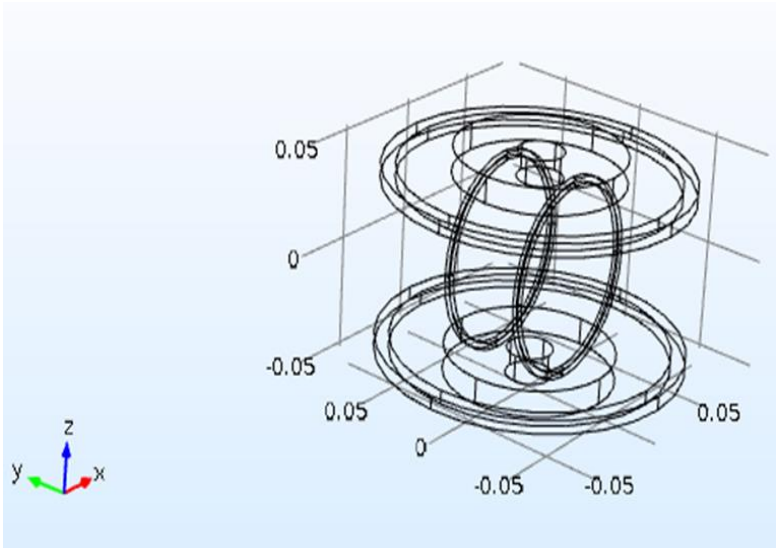

Figure 36. 3D View of simulated coils setup.

The suggested MPI scanner consists of two Helmholtz coil pairs oriented in the Z and Y axes. These coils generate the drive field and enables the motion of the FFP in one Y-Z plane of the volume of interest. The FFP results from the magnetic field generated by the Maxwell coil pair oriented in the Z axis.

The properties of the coils are the same as mentioned in the previous section, shown in tables 1,3 and 5. In table 1 are given the properties

of the Z-oriented drive coils, in table 3 the parameters of Y-oriented drive coils and in table 5 the properties of the selection gradient coils in the Z axis, the distance between the coils is equal to the coil outer diameter.

The simulated results of the magnetic flux density in the center of the device, from the superposition of the three generated field mentioned above are

B_z (T)	B_y(T)	B_x(T)
0.016036	0.007459	2.3343·10^-5

Table 6.

Magnetic flux density resulted from the superposition of the gradient selection field and the drive fields calculated by COMSOL software is illustrated in the figures below.

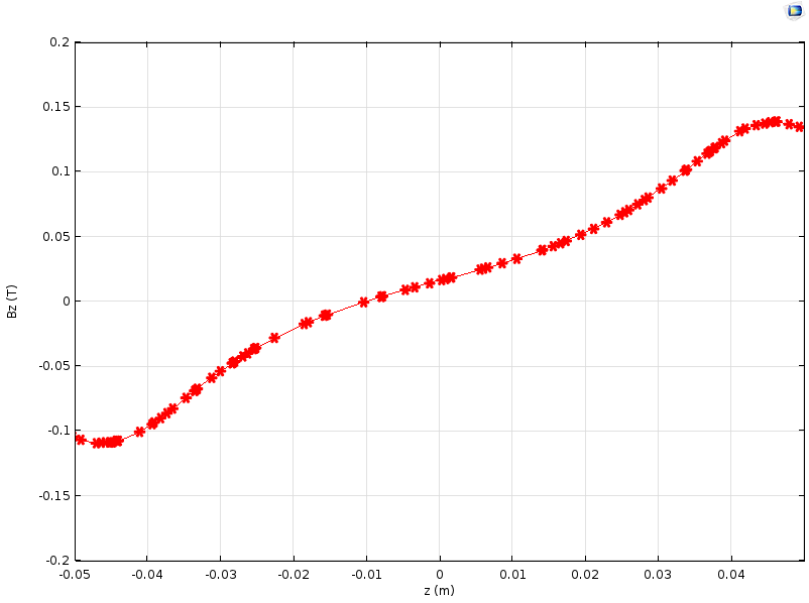

Figure 37. Magnetic flux density, Z-component in respect with Z coordinate.

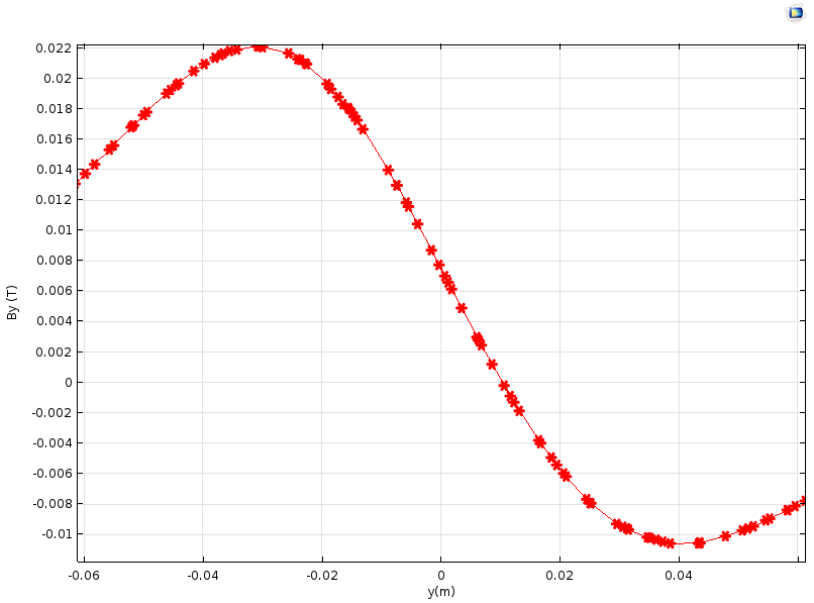

Figure 38. Magnetic flux density, Y-component in respect with Y coordinate.

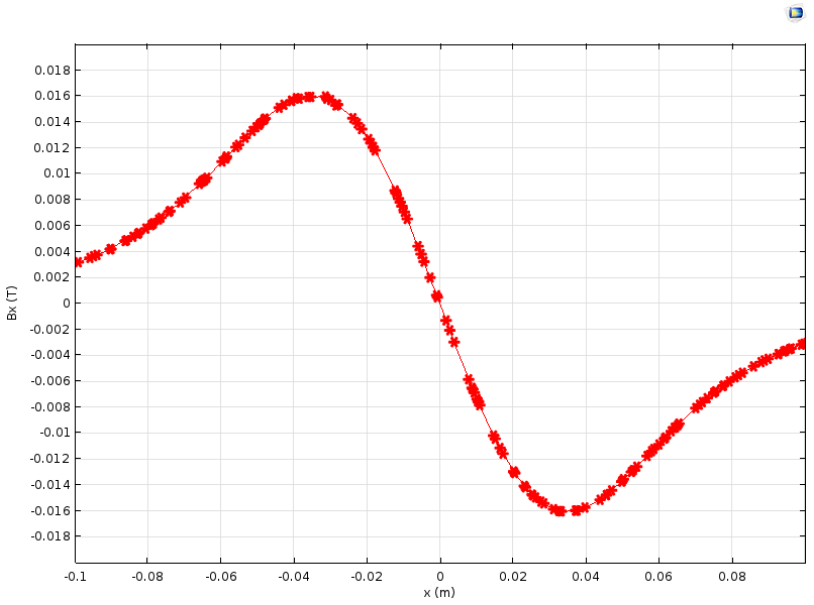

Figure 39. Magnetic flux density, X-component in respect with X coordinate.

There is sufficient magnetic field linearity in the central region within -0.02 m to 0.02 m in all directions.

The field gradient strength G_z was about 1.5 $Tm^{-1}\mu_0^{-1}$ in Z-axis and $Gx \approx G_y \approx -0.75\ Tm^{-1}\mu_0^{-1}$ in Y-axis.

The values of the magnetic field as resulted from the simulation were $H_z \approx 0.016\ T/\mu_0$ and $Hy \approx 0.0075\ T/\mu_0$.

Hence as shown in section 3.5.2 for sinusoidal oscillating magnetic fields in Z and Y axes, with amplitude A_z^D=0.016 T/μ_0 and A_y^D=0.0075 T/μ_0 respectively, the FOV will be a Z-Y plane with side lengths

$$l_z=2\frac{A_z^D}{G_z}\approx 0.02 \text{ m and } l_y=2\frac{A_y^D}{G_y}\approx 0.02 \text{ m}$$

Next, Lissajous trajectory sampling schemes to cover the FOV were simulated.

The Lissajous trajectory describes in general complex harmonic motion.
For the FFP to follow a 2D Lissajous trajectory, sinusoidal currents in each drive-field coil should be used and the frequencies should be chosen to be similar.

$$f_z \approx f_y \tag{4.3}$$

To obtain similar frequencies, the frequency ratio can be chosen as

$$\frac{f_z}{f_y}=\frac{N_D}{N_D+1} \tag{4.4}$$

so that the repetition time

$$T_R=\frac{f_z}{f_y} \tag{4.5}$$

remains finite.

Considering (4.4) relation (4.5) could be written

$$T_R=\frac{N_D+1}{f_y}=\frac{N_D}{f_z} \tag{4.6}$$

Increasing N_D leads to more similar frequencies and a longer repetition time [KNO12].

First, by applying sinusoidal currents in both drive fields with the same frequency, 25kHz, same amplitude, and with zero phase difference, i.e.

$$I_z = 10.82\sin(2\pi 25000t) = I_y$$

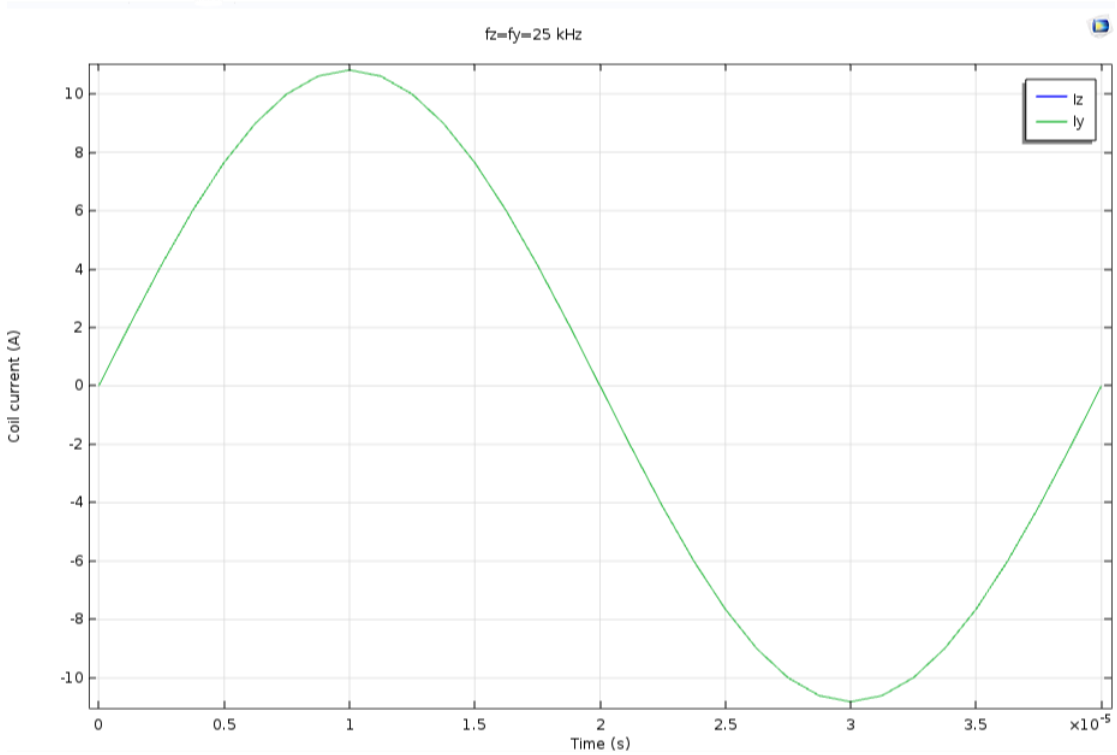

Figure 40. Coil currents I_z and I_y applied in the respective Drive coils

FFP moves across a line as expected. In figure 41. six snapshots of the FFP movement are shown.

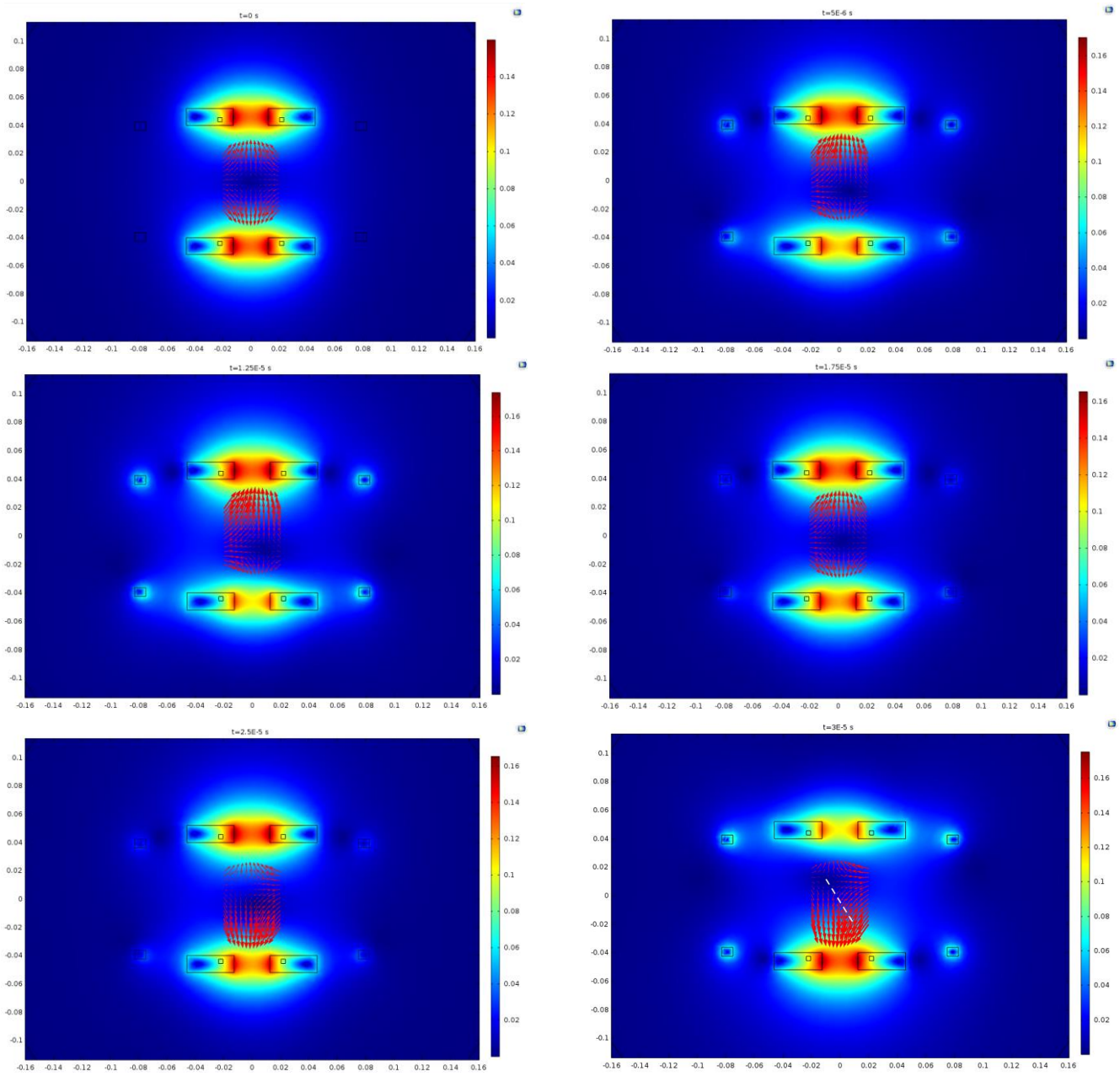

Figure 41. Snapshots of FFP movement along a line. The red arrows indicate the magnetic field vector $\vec{H}$, the color legend refers to the magnetic flux density B with blue being almost zero. For visualization the dashed line implies the FFP trajectory.

Next, sinusoidal currents applied in both drive fields with the same frequency, 25kHz, same amplitude, and $\pi/2$ phase difference, i.e.

$$I_z = 10.82\sin(2\pi 25000t) \text{ and } I_y = 10.82\sin(2\pi 25000t + \pi/2)$$

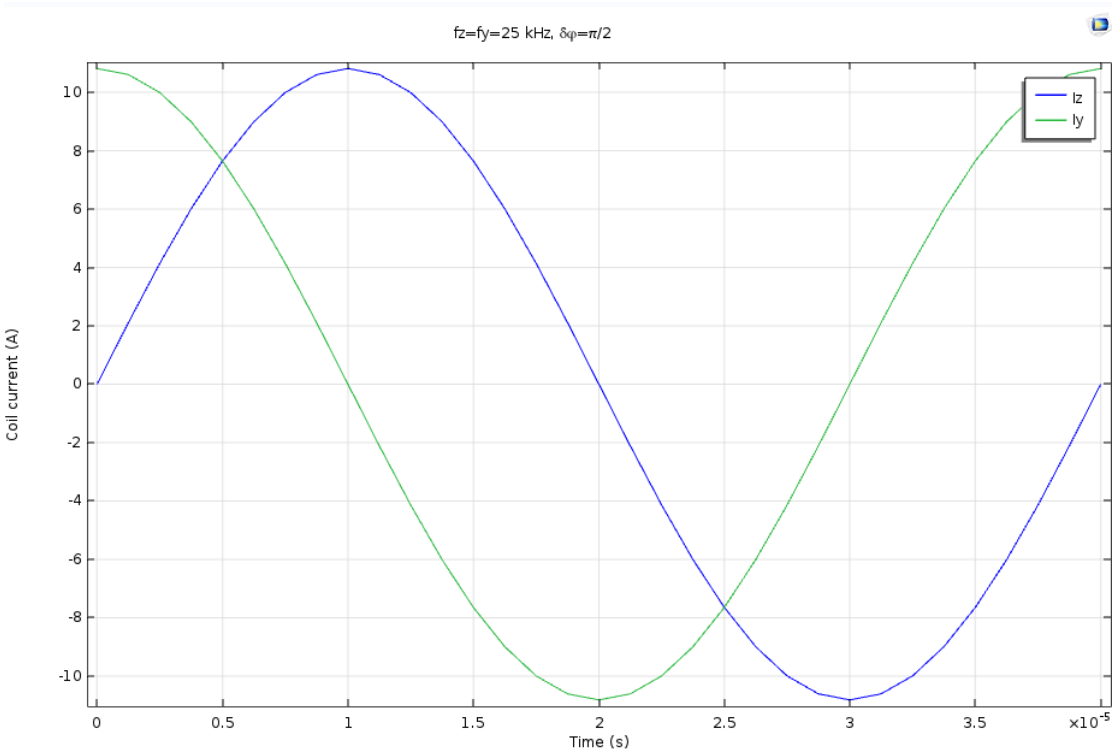

Figure 42. Coil currents I_z and I_y applied in the respective Drive coils

The FFP moves in a circle.

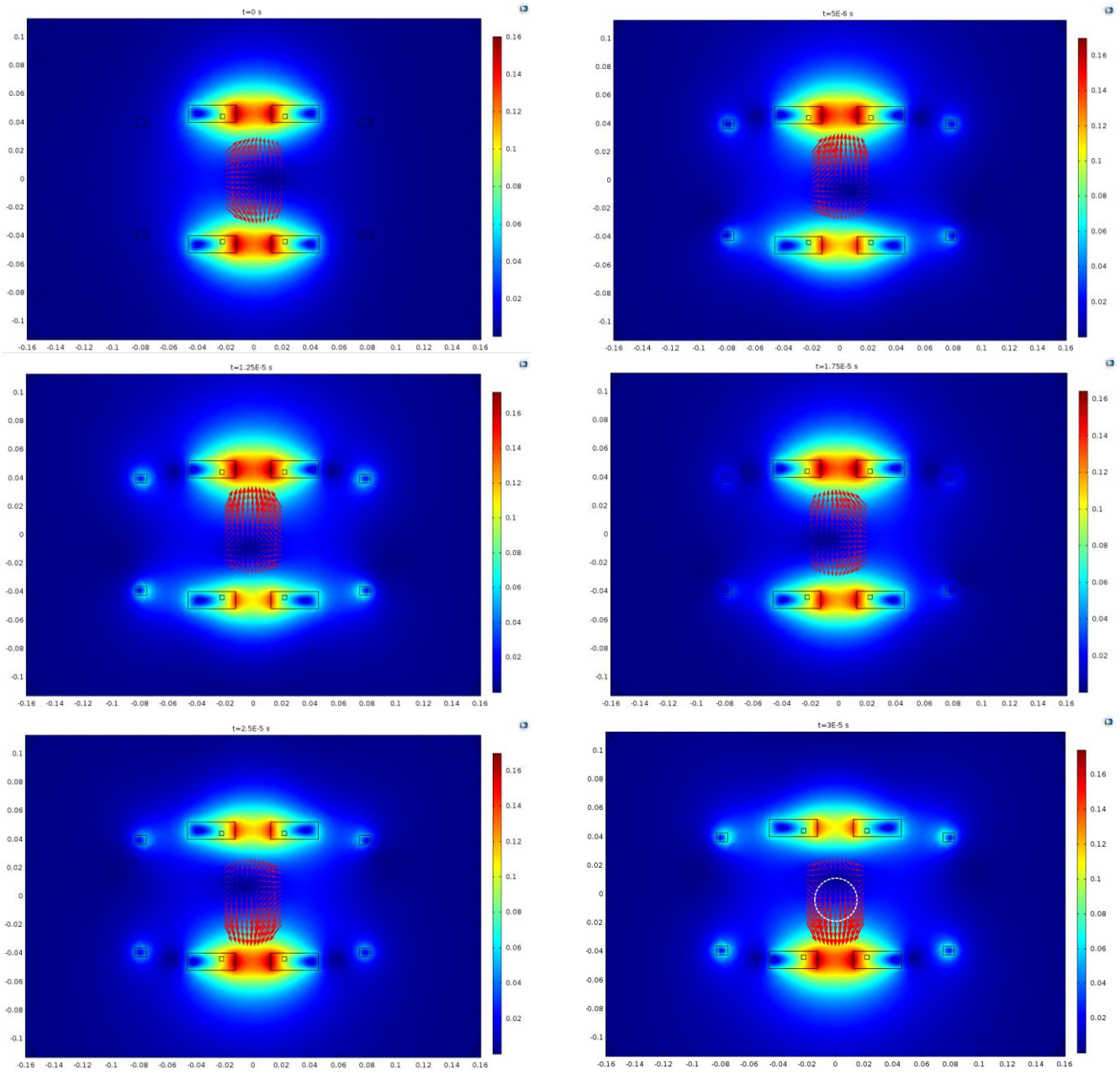

Figure 43. Snapshots of FFP movement along a circle. The red arrows indicate the magnetic field vector $\vec{H}$, the color legend refers to the magnetic flux density B with blue being almost zero. For visualization the dashed line implies the FFP trajectory.

Next, sinusoidal currents applied in both drive fields with the same frequency, 25kHz, same amplitude, and $3\pi/4$ phase difference, i.e.

$$I_z = 10.82\sin(2\pi 25000t) \text{ and } I_y = 10.82\sin(2\pi 25000t + 3\pi/4)$$

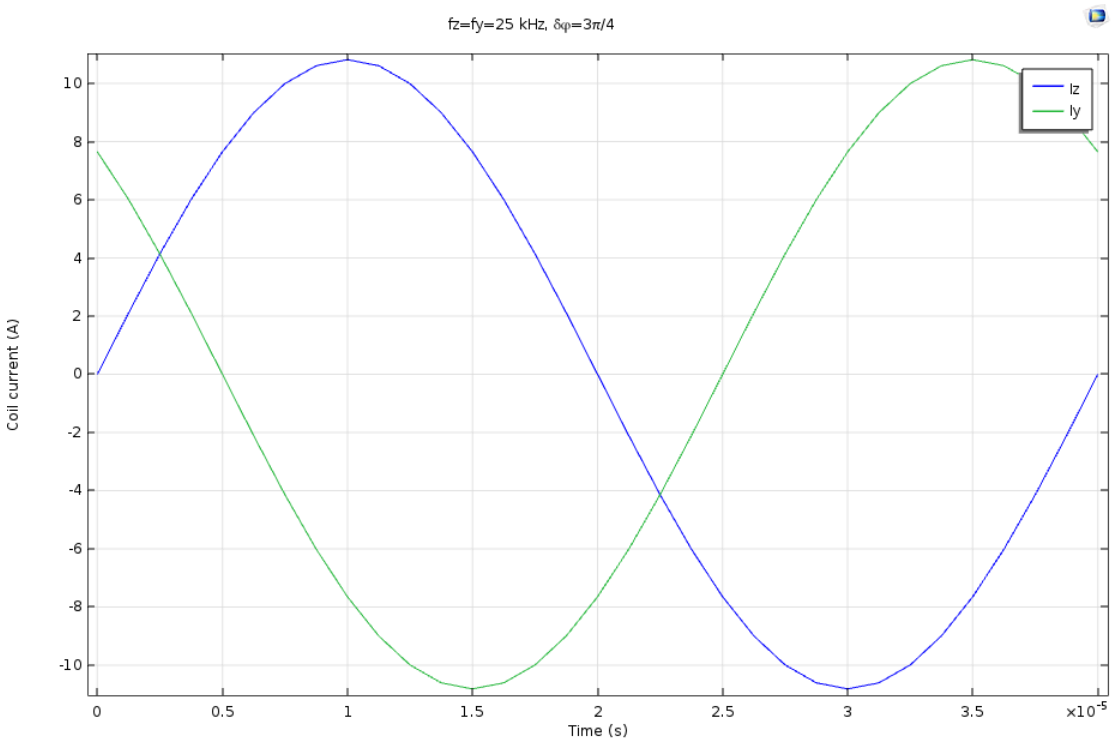

Figure 44. Coil currents I_z and I_y applied in the respective Drive coils

The FFP moves in an ellipse.

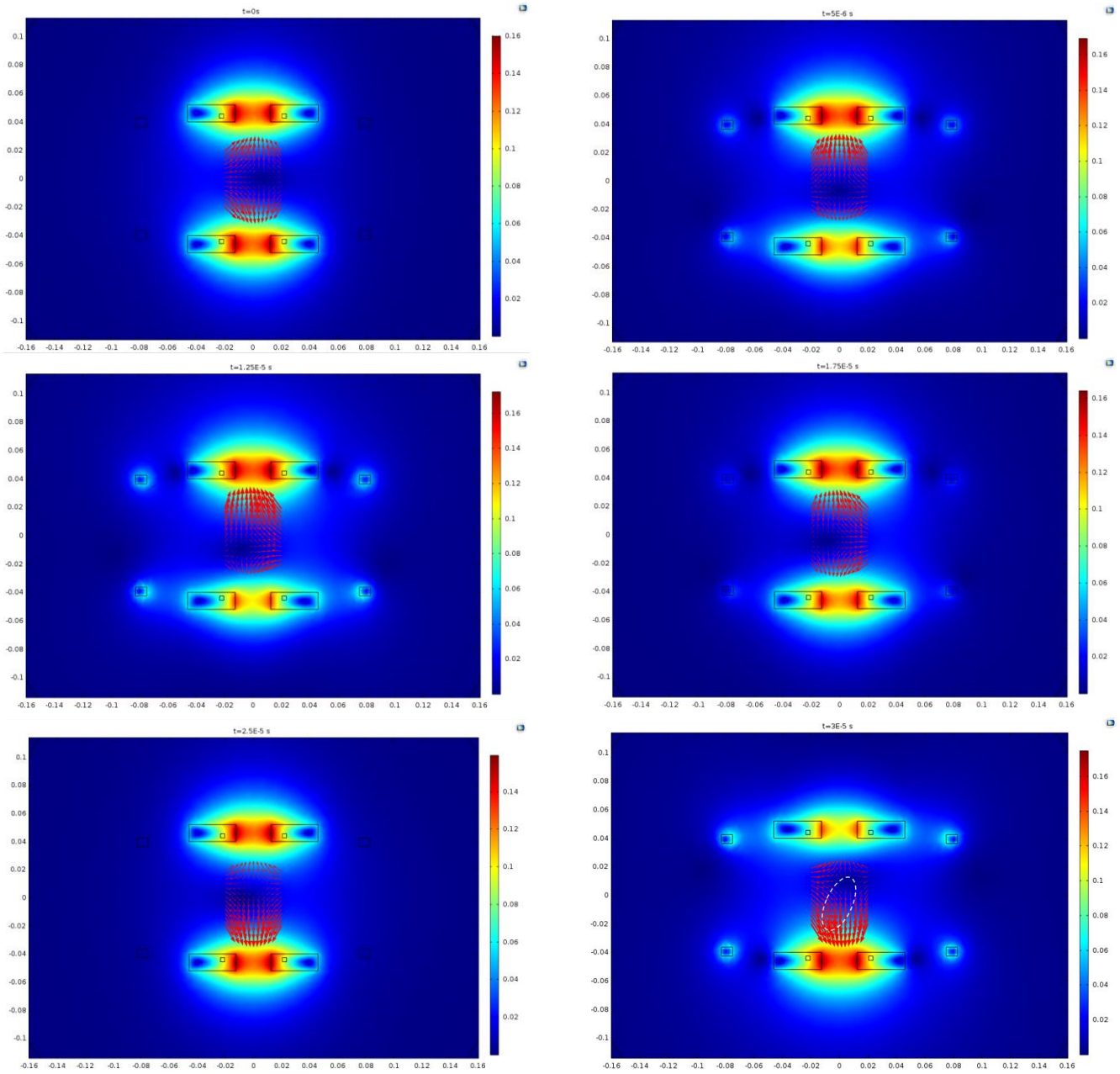

Figure 45. Snapshots of FFP movement along an ellipse. The red arrows indicate the magnetic field vector $\vec{H}$, the color legend refers to the magnetic flux density B with blue being almost zero. For visualization the dashed line implies the FFP trajectory.

Of course, more complex Lissajous trajectories that is difficult to be presented in a few static images, are used in reality. These simple cases aimed to verify the motion of the FFP.

As the density of the trajectory increases so does the quality of the reconstructed image.

An FFL MPI scanner suggested by [ERB14] was also simulated using COMSOL Multiphysics.

To make reconstruction feasible using an FFL, a rotation of at least 180◦ as well as translation of the FFL is necessary. Using a dynamic FFL imaging device a slow rotation and a fast translation of the FFL leads to a radial trajectory. This is possible by rotating the selection field with a frequency f_S that is much lower than the excitation frequency f_E. The frequency of the selection field in this simulation was set at 100 Hz and the drive field frequency remained at 25 kHz as used in FFP MPI. The scanning density of the FFL trajectory is determined by the ratio f_E/f_S

The simulated setup consists of five Maxwell coil pairs. The outer coil pairs placed in X and Y-axis and the inner coil pairs generate the dynamic part of the selection field. The outer Z-coil pair generates the static part of the selection field. The superposition of these fields results in an FFL field rotated by an arbitrary angle θ in the XY-plane.

The external diameter of the outer coils is 92 mm, the internal diameter is 50 mm, and the width is 12 mm. The coils consist of 54 windings each and the current amplitude for the generation of the selection field is $I_{outer} = 6.76[A]\cos(2\theta)$. For the FFL translation, an additional current equally orientated in opposing coils should be applied to the outer coils.

The external and internal diameter of the inner coils is 58 mm and 19 mm respectively. The width is 6 mm and they consist of 34 windings each. The applied current is $I_{inner} = 4.54[A]\sin(2\theta)$.

The outer Z-coil pair has an external dimeter of 92 mm and the internal diameter is 50 mm. The width is 16 mm and they consist of 72 windings. The applied current is $I_Z = 9.1A$.

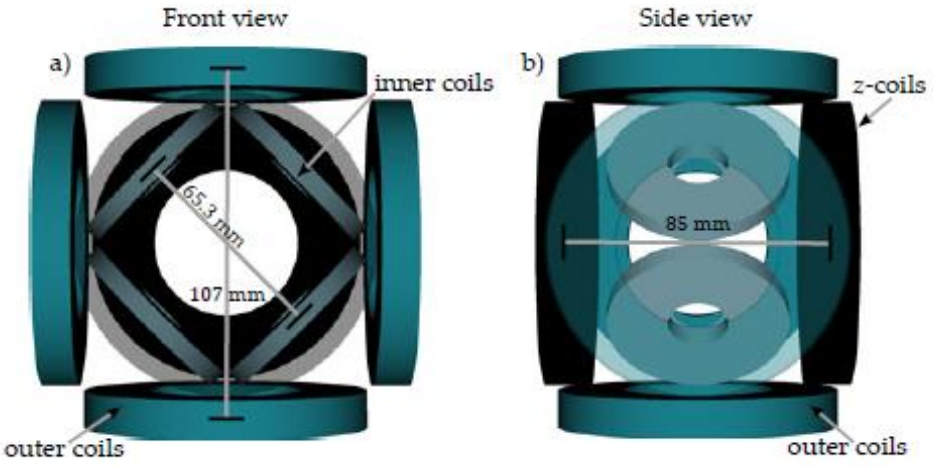

Figure 46. MPI scanner topology and characteristics by [ERB14].

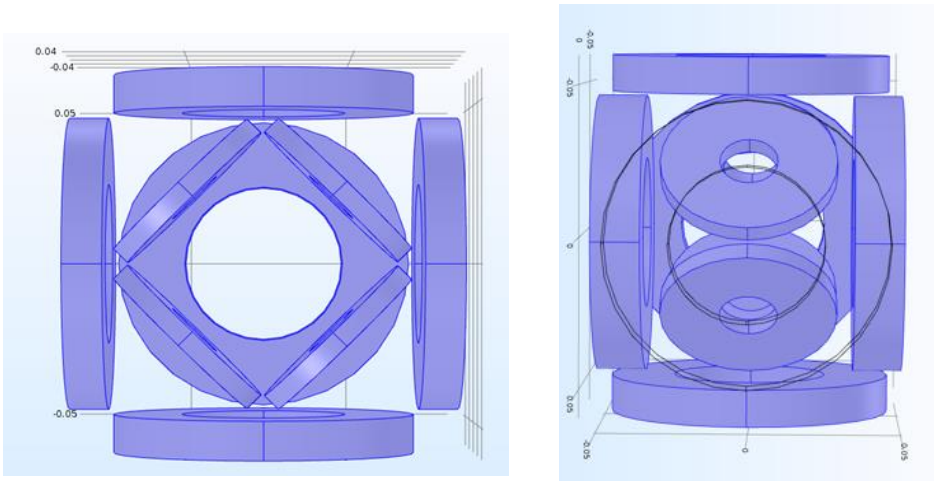

Figure 47. Simulated FFL MPI scanner.

The rotation of the FFL is shown in figure 48. XY-plane is shown. The color legend refers to magnetic flux density generated by the set of coils, with blue being close to zero and red the maximum value.

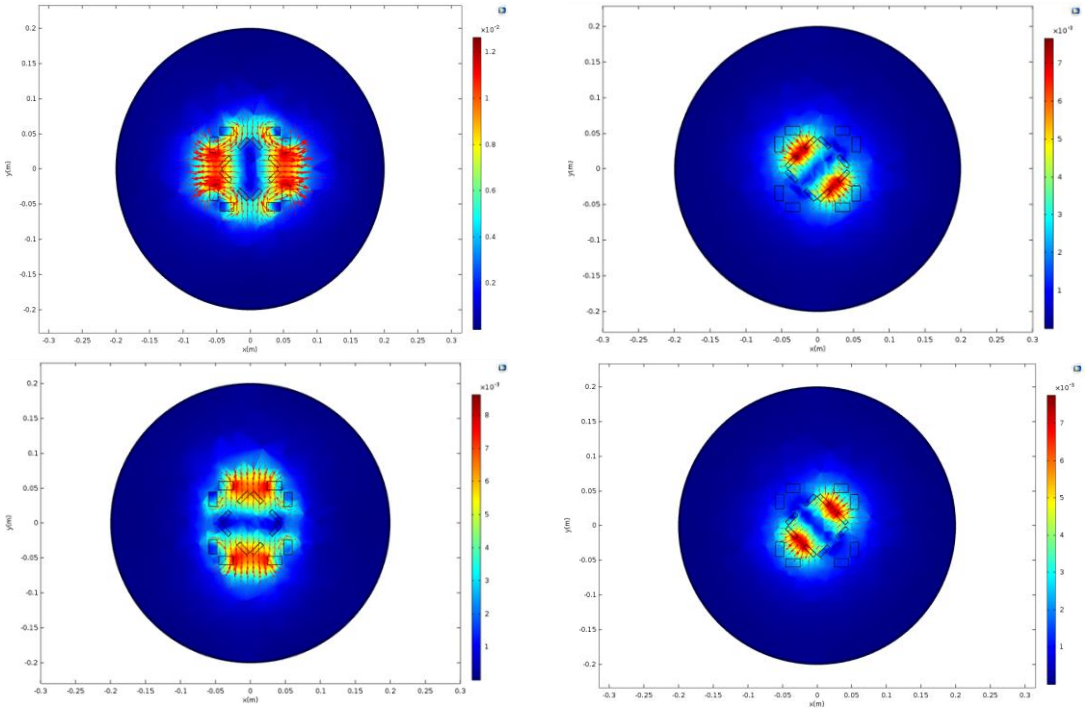

Figure 48. FFL moving along a circle in the Y-X plane.

4.5 Simulation of SPIO Nanoparticles' Magnetic Behavior

The behavior of SPIO nanoparticles when exposed to the magnetic field generated by an MPI setup was simulated using COMSOL Multiphysics. Nanoparticles of Fe_3O_4 with a diameter of 30nm, saturation magnetization $M_s \approx 477 kAm^{-1} \approx 0.6 T\mu_0^{-1}$ and with a magnetization described by Langevin function, were considered. As a phantom, a cylinder with a diameter of 0.5mm and length of 1mm including the nanoparticles was placed in the center of the FFP MPI scanner setup presented in the previous section. The rest of the space is field with air which has zero magnetization. For the simplicity of the calculations only magnetization in the Z direction was considered. The resulted magnetization curve is shown below.

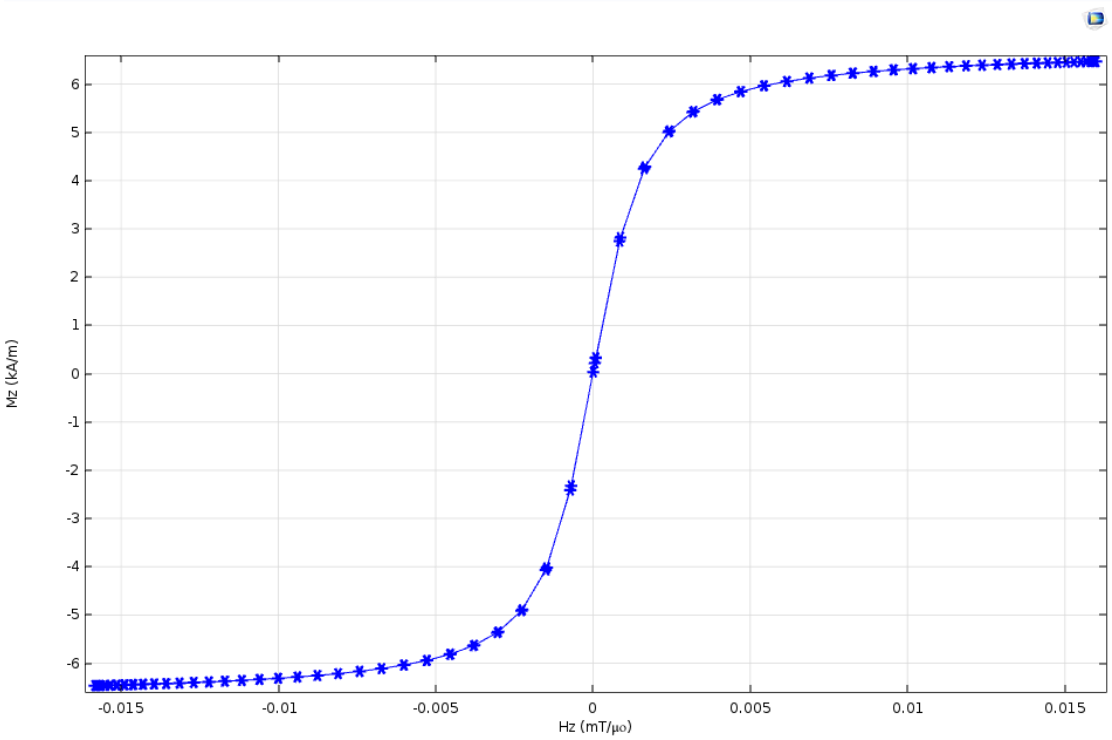

Figure 49. Magnetization curve of SPIO nanoparticles with a diameter of 30nm at a temperature of 300K.

The results are the expected. As figure 49 indicates, the magnetization of the nanoparticles reaches saturation at about 5mT.

Next, another two cylinders of nanoparticles were placed into positions away from the center. The Magnetization change and the magnetic flux density with respect to time are shown in figures below for four different point positions inside the FOV (fig. 50,51,52) and one out of the FOV (fig. 53). FFP is moving across a line as indicated in figure 41.

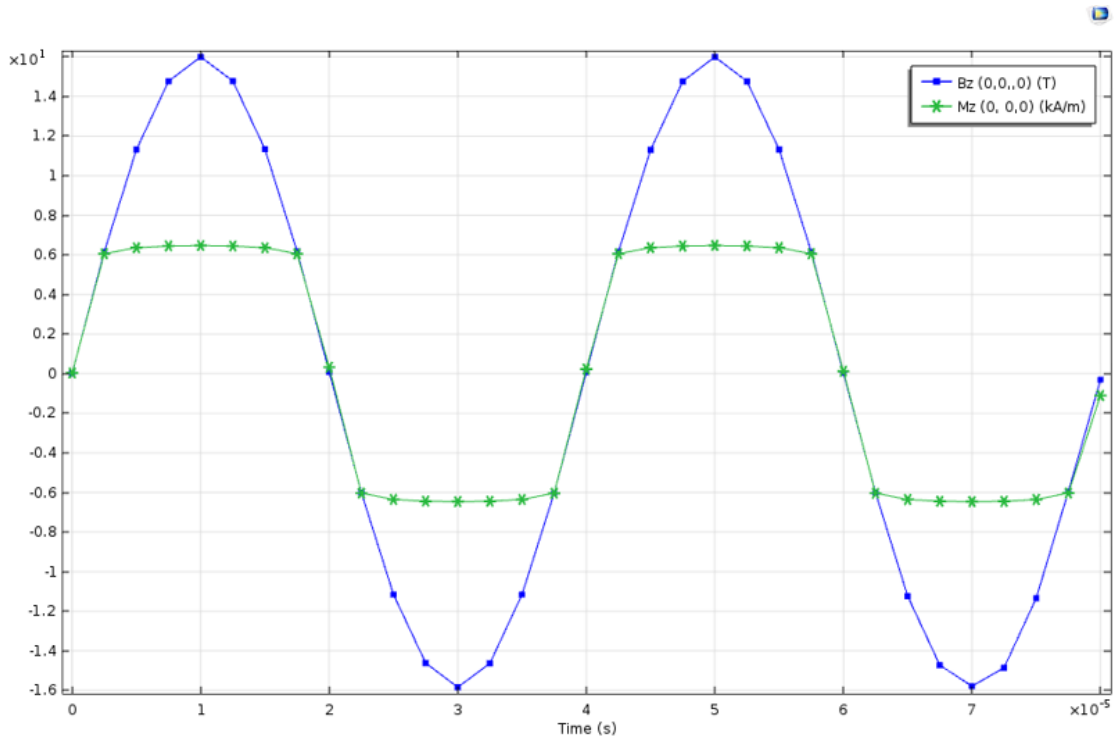

Figure 50. Magnetization and magnetic flux density change with respect to time in position (0,0,0)

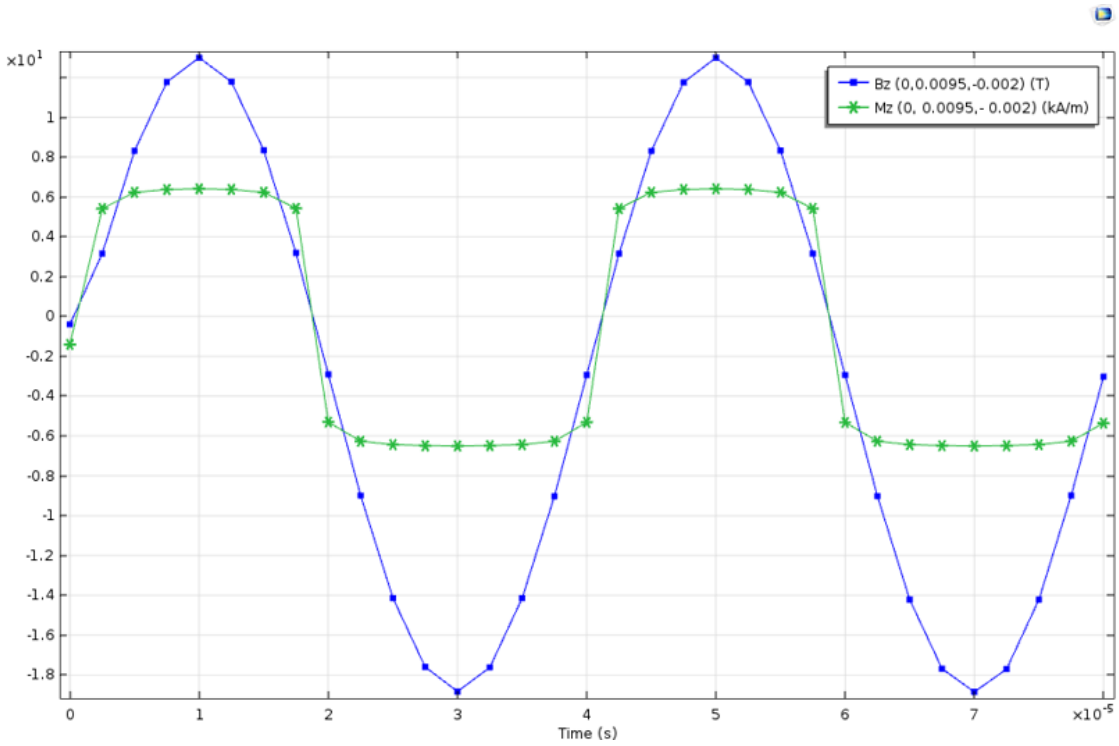

Figure 51. Magnetization and magnetic flux density change with respect to time in position (0,0.0095, -0.002).

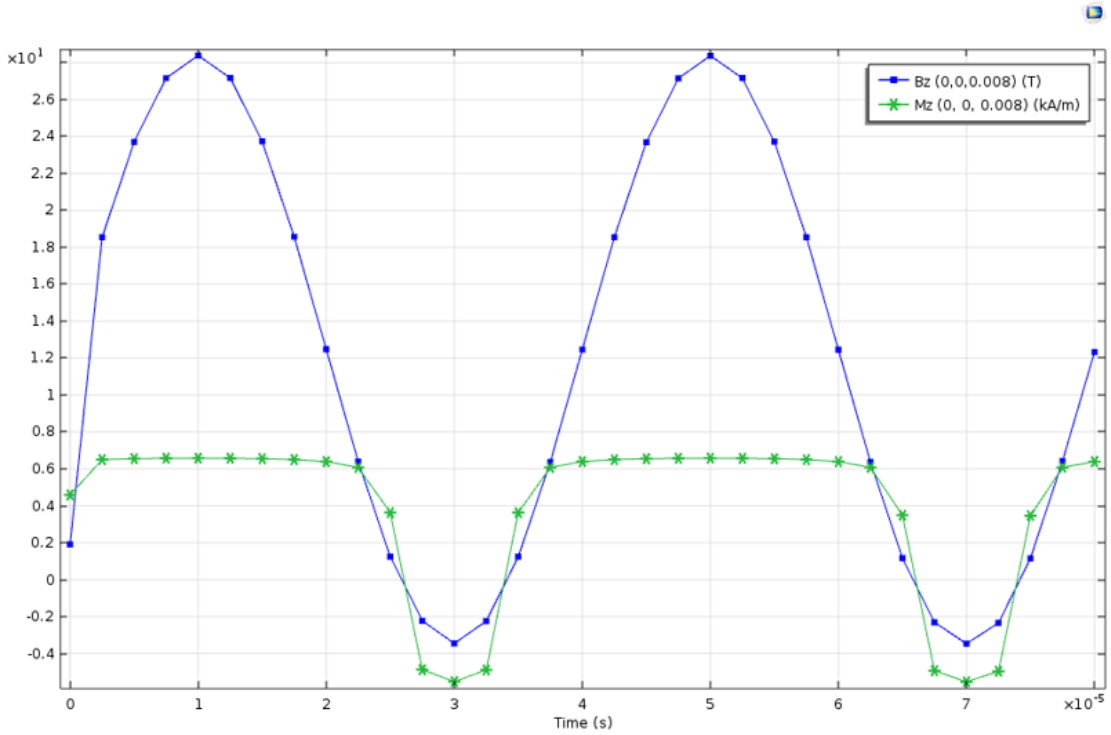

Figure 52. Magnetization and magnetic flux density change with respect to time in position (0,0,0.008).

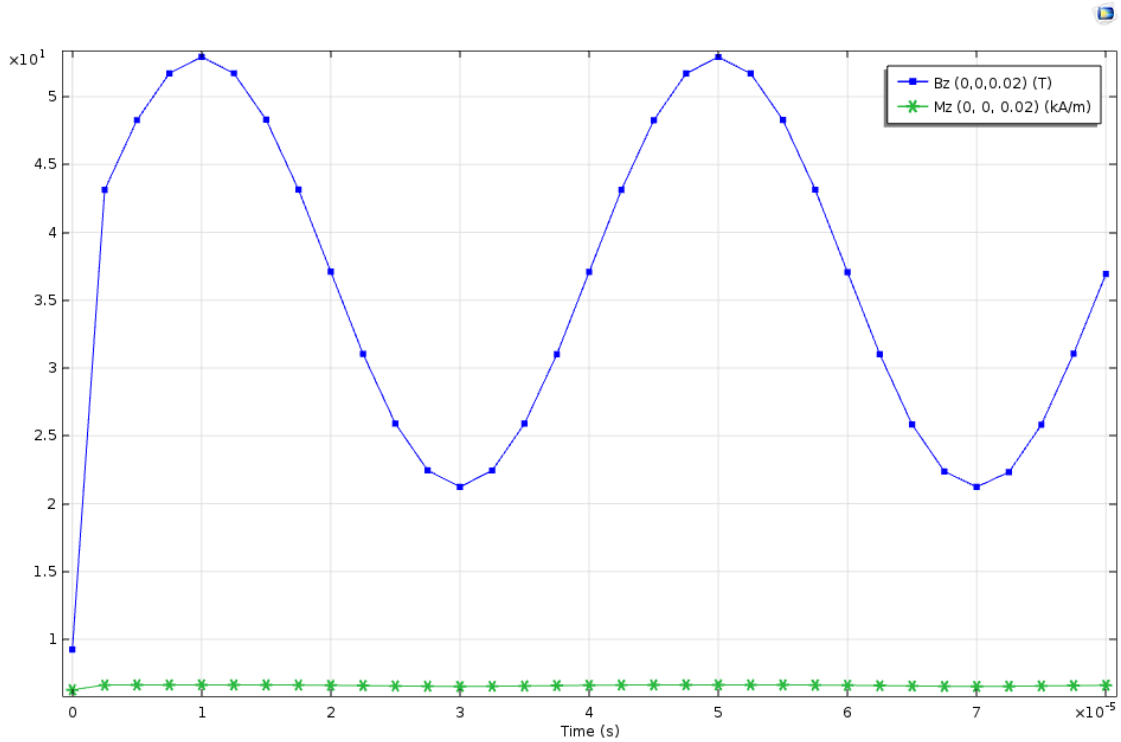

Figure 53. Magnetization and magnetic flux density change with respect to time in position (0,0,0.02).

The way that the magnetization changes with respect to time is different in the different positions since the magnetic field is also different. This leads to different signal generation enabling spatial

encoding. Anything outside the FOV reaches magnetization saturation and does not provide any signal.

Considering simplified equation (3.6) the form of the expected induced signal in the receive coils due to the particles' magnetization change is given in the figure below for the aforementioned positions.

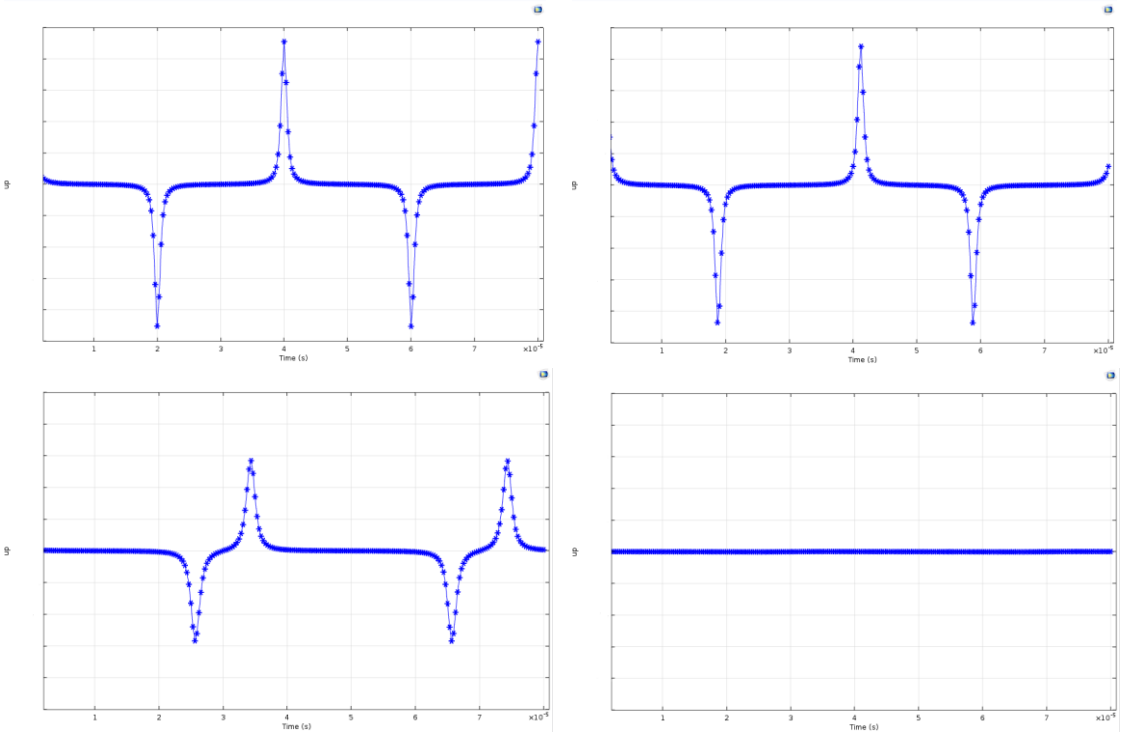

Figure 54. Voltage induced by particles' magnetization change with respect to time in positions (0,0,0) upper left, (0,0.0095, -0.002) upper right, (0,0,0.008) lower left and (0,0,0.02) lower right.

As mentioned in section 3.4.3 it is common to consider the received signal in frequency space so that the difference between the excitation signal and the particle signal becomes more obvious. The Fourier series of the measured voltage u(t) contains higher harmonics of the excitation frequency f_E. Expanding the signal into a Fourier series using formula (3.7). The spectrum consists of higher harmonics which are multiples of the fundamental frequency f_E. For example, considering the expected signal from a δ-like particle distribution in position (0,0,0) the frequency spectrum would be expected to have the form shown in the figure 55.

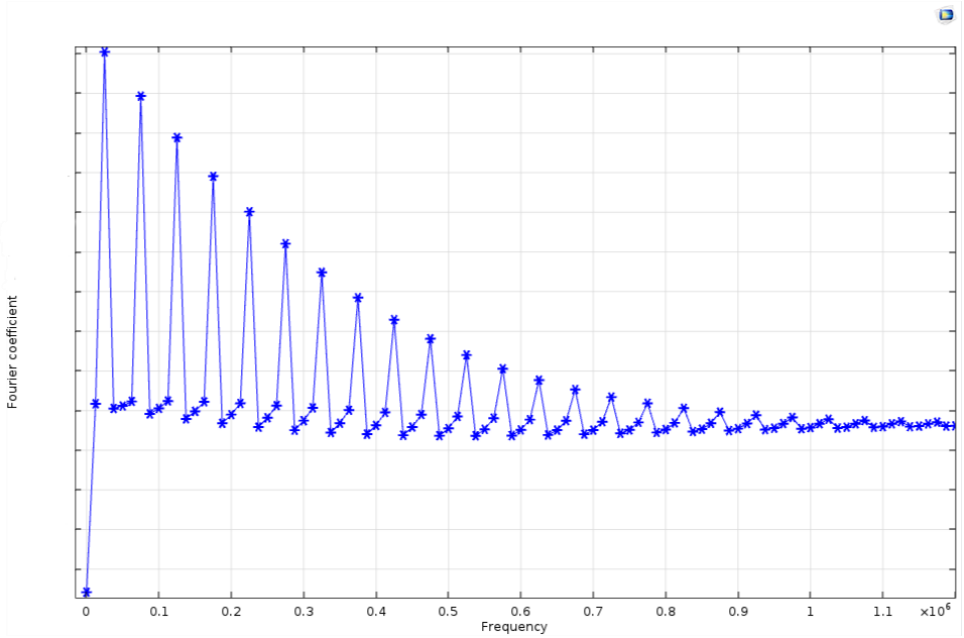

Figure 55. Frequency spectrum of the particle signal as given by (3.6).

The fundamental frequency at 25kHz gives the highest peak and higher odd harmonics at 75kHz, 125kHz, 175kHz etc., can be observed in the frequency spectrum.

The induced voltage which is proportional to the change of the magnetization with respect to time is recorded by the receive coils. However, not only the particle signal but also the transmit signal directly couples into the receive coil. This signal is several magnitudes larger than the particle signal. To separate the particle signal from the excitation signal filtering is necessary, notch filters or else known as a band stop filters (BSF) could be used [GLE13]. Another way to achieve decoupling is the field-cancelation method [GRA13], this concept is similar to a gradiometer coil concept. However, the filtering damps not only the excitation frequency of the transmit coil but also the base frequency of the particles. Leaving only the higher harmonics of the particle signal leads to a loss of information. This loss has an impact to MPI reconstruction. Additionally, since the voltage induced due to the magnetization change of the SPIO tracer particles is very low a low noise amplifier (LNA) is necessary to amplify the signal. If the frequency of the magnetization change is too low, the intrinsic noise of the detector, e.g. coil resistance or amplifier noise dominates the noise.

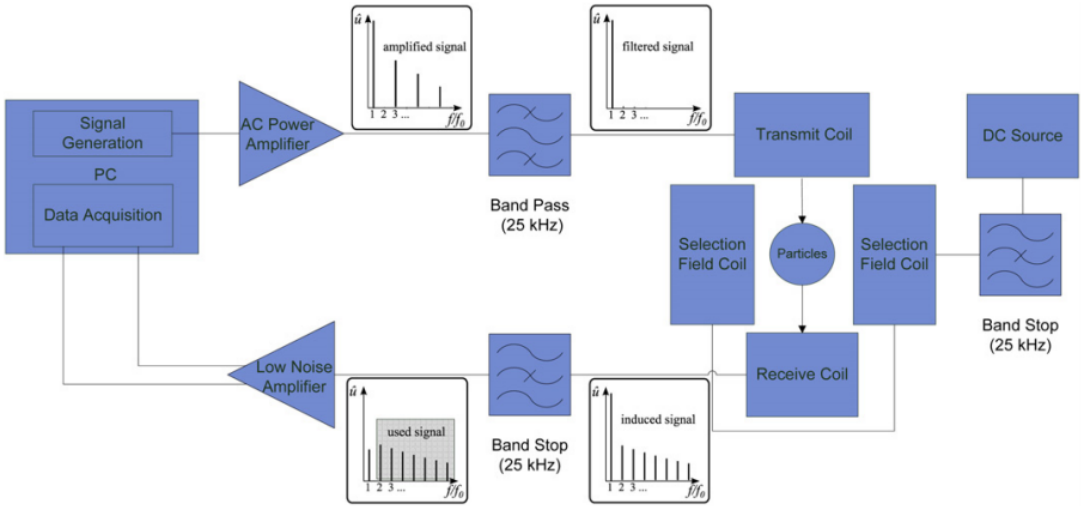

Figure 56. Signal chain of a typical MPI device [BUZ12].

Placing a receive coil in the z, y or x axis, would be mainly sensitive to field changes in the z-direction, y-direction and x-direction respectively. For 1D imaging 1 receive coil is necessary, for 2D imaging 2 and 3 for 3D imaging. It is shown that larger number of receive coils do not significantly affect the quality of the reconstructed image.

In figure 57 Reconstruction results for different receive coil numbers and different sampling densities specified by the repetition time are shown.

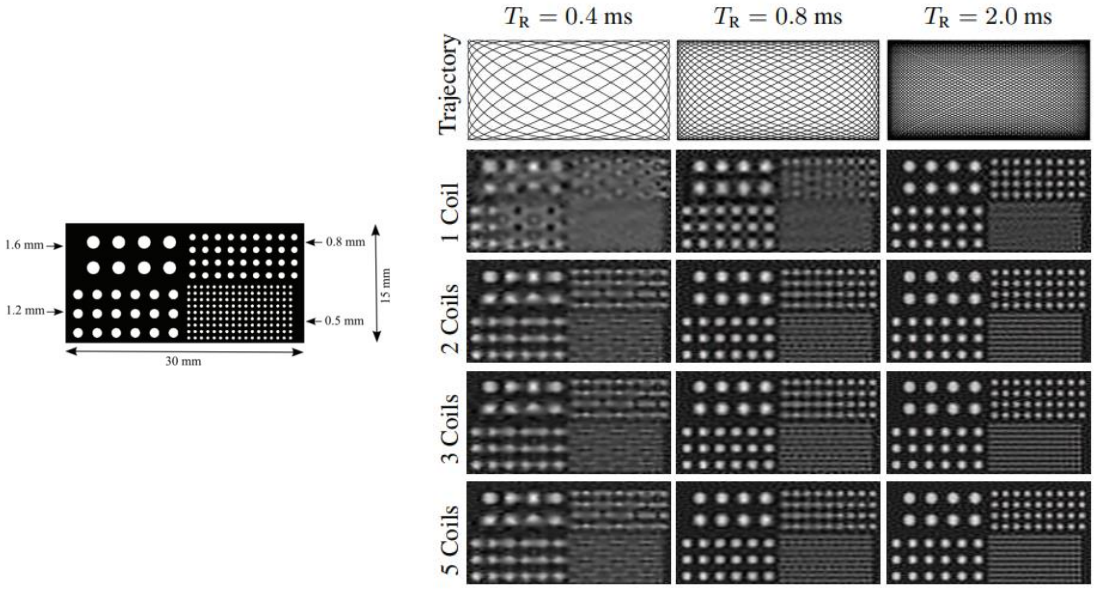

Figure 57. Phantom used in 2D MPI simulation, consisting of tubes (left). Reconstructed images for various receive coil numbers and sampling densities (right) [KNO11].

It is obvious from figure 57, that the quality of the reconstructed image directly depends on the sampling densities. There are of course several other factors that affect the reconstruction results.

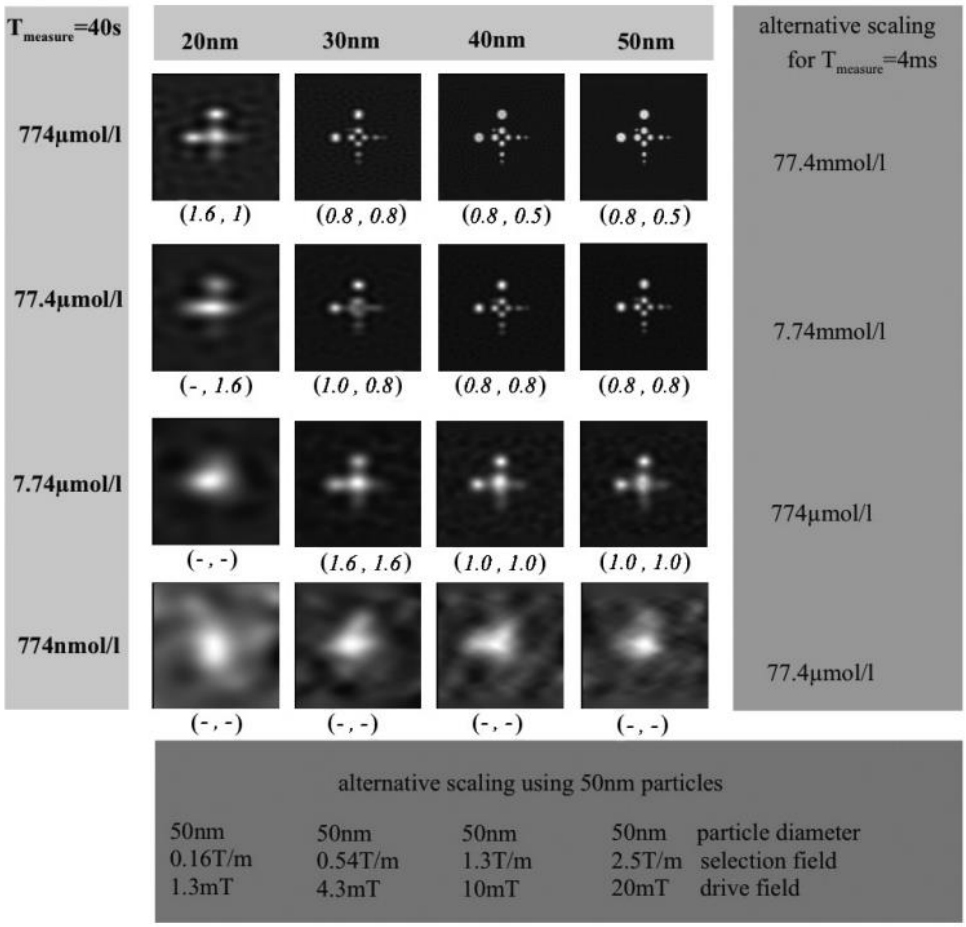

Figure 58. Reconstructed images for various particle sizes and concentrations [WEI07].

CHAPTER 5. RECONSTRUCTION

5.1 Introduction

In this chapter the general concept of reconstruction procedures in MPI is introduced. In MPI the reconstruction of a spatial map of the particle concentration is given by the solution of a linear system of equations, thus ART could easily apply for image reconstruction and is indeed a widely preferred method. Algebraic Reconstruction Technique (ART) and its advantages are briefly discussed. Next, image reconstruction of a simple phantom using ART in order to compare the quality of the reconstructed image for different number of projections is presented. Finally, the influence of noise generated in MPI, in the quality of reconstructed image is evaluated by proceeding to image reconstruction of a software phantom using ART for different noise models.

5.2 Reconstruction in MPI

Contrary to the projection data in CT, raw MPI data do not allow direct visualization. The first step for the reconstruction of an MPI image is to transform the measured voltages into particle concentration. For that to happen, the assumption that all MPI reconstruction techniques share, is that the relation among the particle concentration c(r) at any position $r \in \Omega \subset r^3$ and the measured signal u(t) is linear, as it derives from relations (2.12) and (3.2) the continuous MPI signal equation is given

$$u(t) = \int_{\Omega} S(\vec{r}, t)c(\vec{r})d^3r \tag{5.1}$$

where

$$S(\vec{r}, t) = -\mu_0 \vec{p}(\vec{r}) \frac{\partial \vec{m}(\vec{H}(\vec{r},t))}{\partial t} \tag{5.2}$$

is called the system function.

Thus, the linear relation of particle concentration and the signal u(t) can be expressed via an integral transform with the system function $S(\vec{r}, t)$ being the internal kernel [ERB14]. Since $u(t)$ and $s(r,t)$ are both periodic functions, they can be expanded into a Fourier series and the integral (5.1) is reformulated

$$\hat{u}_k(t) = \int_{\Omega} \hat{S}_k(\vec{r}, t)c(\vec{r})d^3r \tag{5.3}$$

where $\hat{u}_k(t)$ is the k_{th} Fourier coefficient of the measurement signal $u(t)$, which is usually limited by some upper frequency index K that is derived by the sampling bandwidth and $\hat{S}_k(\vec{r},t)$ is the system function in frequency space [KNO17].

Regardless of which reconstruction method is going to be used the knowledge of the system function is required. The determination of the system function could be either measurement-based or Model-based. In measurement-based system function a calibration scan prior to reconstruction occurs by placing a delta sample at a position r to measure the induced voltage u(t) and obtain the frequency component $\hat{u}_k(t)$. By shifting the delta sample through the FOV to different positions r, either by robot-based movement or a dynamic motion, data are acquired at each position and thus a set of frequencies components is available for the determination of the system function. In Model based reconstruction, as the name implies, the received signal is modeled. In this case the used model could be defined under the assumption of ideal magnetic fields and ideal magnetization behavior, or the induced voltage could be modeled more accurately in frequency space by including realistic field shapes and particle models. For ideal field conditions, the model does not account for field inhomogeneities of the drive field and nonlinearities of the selection field [KNO10], [GRU13]. In this case MPI signal, could expressed either in time space or in frequency space.

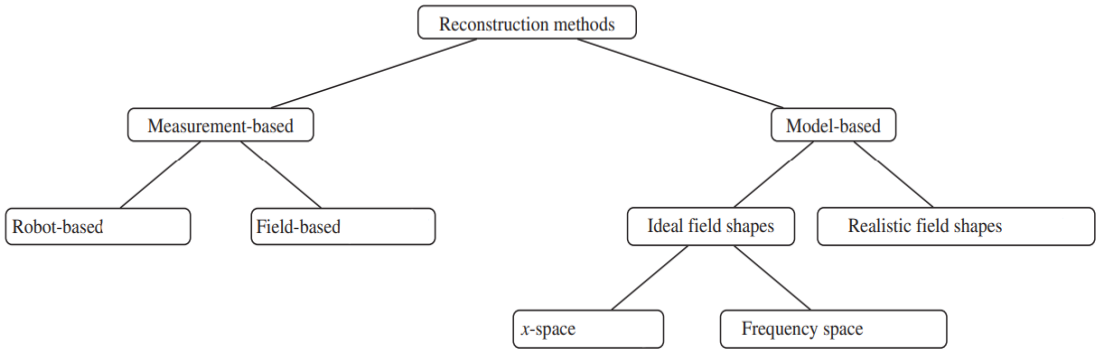

Figure 59. A schematic overview of different reconstruction methods in MPI [GRU13].

Even though a model-based MPI system function determination is faster, it leads to a lower image quality comparable to that of images reconstructed with measurement-based system function, since up to date, the existed particle models are too simple, there are no exact physical models for describing particle magnetization. Improvements in modeling of the magnetic fields and particle dynamics could have positive effects [ERB12]. The calibration scans for measurement-based system function are very time consuming. Additionally, when using a

delta sample a tradeoff between the desired voxel size and the desired SNR has to be made, since for a high resolution the delta sample should be as small as possible while the signal to noise ratio is proportional to the size of the delta sample.

Either way the system function will be acquired for a discrete number of spatial positions. If the volume of interest is subdivided into N equally sized voxels of volume ΔV, the discrete representation of the MPI signal equation in frequency space is given

$$\hat{u}_k(t) \approx \Delta V \sum_{n=1}^{N} \hat{S}_{nk}(\vec{r}, t) c_n(\vec{r}) \tag{5.4}$$

In the case of considering a finite number K of harmonics, equation (5.4) can be written in matrix vector representation

$$\boldsymbol{u} \approx \mathbf{S}\mathbf{c} \tag{5.5}$$

Solving the inverse problem

$$\boldsymbol{c} \approx \mathbf{S}^{+}\mathbf{u} \tag{5.6}$$

will lead to the final SPIO tracer distribution, where S^{+} denotes the pseudoinverse matrix of S.

To solve the linear system of equations either singular value decomposition or iterative methods like Conjugate Gradient Normal Residual (CGNR) and ART can be applied [ERB14].

The determination of the system function followed by the solution of the linear system of equations containing the relation between the particle distribution and the measured received signal holds for both FFP and FFL imaging in MPI. Using FFL and therefore line data acquisition allows implementing more efficient reconstruction algorithms since data can be transformed into Radon space. In this case, well known standard algorithms such as filtered back projection (FBP) could be used. However, transforming the measured signal into Radon space demands high magnetic field homogeneity along with the FFL and parallel to its alignment [ERB12] as well as minimization of gradient field nonlinearities otherwise artifacts arise [MED15]. In contrast to an FFP, the use of an FFL could decrease scan time by reducing image dimensionality from a 3D image to a projection image. Alternatively, in comparison to a 3D scan of equal scan time, an FFL scanner will increase SNR through more signal averages [KON11].

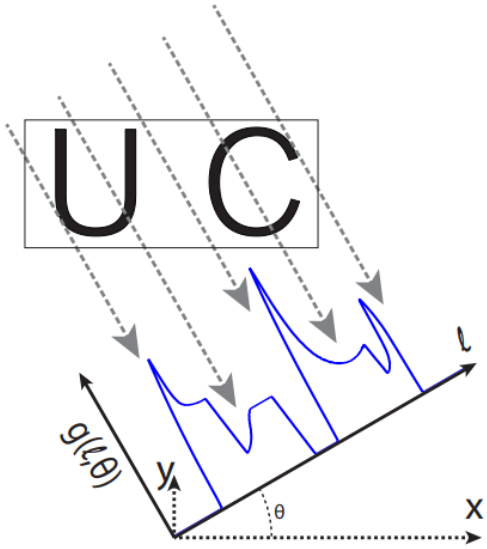

Figure 60. Diagram of projection reconstruction imaging [KON11].

As figure 60 indicates, the data of a single projection g(l, θ) are acquired at an angle θ as the Field Free Line magnetic field rotates. Multiple projections are acquired from various angles θ, and thus a projection reconstruction algorithm can be used to reconstruct a 3D image as is done in Computed tomography [KON13].

Under specific assumptions analytic reconstruction methods could be used. Instead of explicitly arranging the linear system (5.5), one could formulate an algorithm for the direct reconstruction, known as x-space reconstruction. This method was initially proposed by Goodwill and Conolly [GOO10], and it aims to reconstruct MPI data from the 1D measurements usually acquired with Cartesian trajectories under the assumption of a linear selection field, a homogeneous drive-field and particles with infinitely fast relaxation times. The elimination of these assumptions is under research [GOO11], [GOO12]. Another analytic reconstruction algorithm for 1D experiments was developed by [RAH09] called Chebyshev reconstruction. This algorithm uses the frequency space representation of the induced signal and exploits the fact that the signal can be represented by the coefficients of an efficiently and directly invertible weighted Chebyshev transformation. Grȯttner *et al* (2013) proved that x-space reconstruction and weighted Chebyshev reconstruction are mathematically equivalent, thus the same reconstruction result is provided [KNO17].

5.3 Algebraic Reconstruction Technique

The first CT scanner designed by Godfrey Hounsfield in late 1960s, used an approach based on linear algebra and matrix theory to produce images from the machine readings. Algorithms that adopt this point of view are known as Algebraic Reconstruction Techniques (ART) [FEE15]. Algebraic Reconstruction Techniques were introduced by Gordon, Bender and Herman as a way to achieve three-dimensional reconstruction from projections in electron microscopy and radiology [GOR74].

ART treats the problem of image reconstruction as a discrete problem from the start and its algorithms have a simple intuitive basis [RAP98]. Each projected density is thrown back across the reconstruction space in which the densities are iteratively modified to bring each reconstructed projection into agreement with the measured projection [RAP98]. Any image that is produced will be constructed inside a rectangular grid of picture elements, or pixels. To form an image, a specific color value is assigned to each pixel. The size and the number of the pixels N inside the FOV are determined before initializing the reconstruction procedure. The tomographic image consists of a discrete number of unknown variables f_j (j=1, 2…, n^2). The set of projections through the object can be modeled by a linear system of equations. Due to the fact that the path length through each element of the object is different, when using algebraic methods, weights that reflects how much of the pixel that is to be reconstructed is passed through by the beam with respect to the entire area of the pixel are considered, after the assumption that the X-ray beam has a certain width [BUZ08].

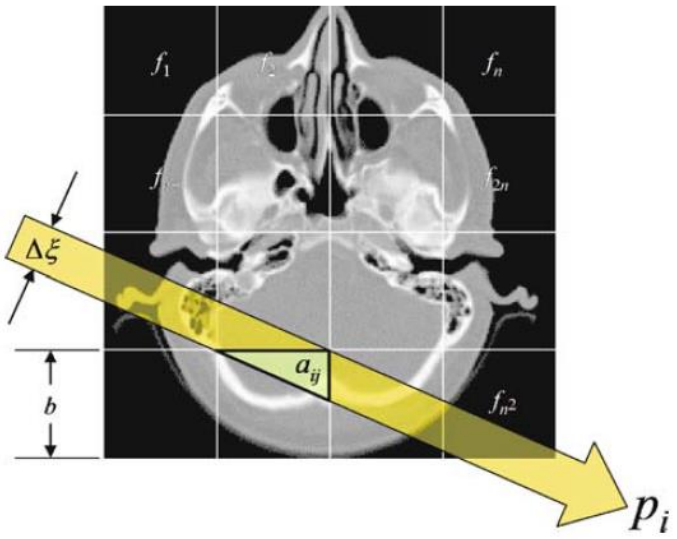

Figure 61. The X-ray beam of width passing through the tissue, illustrated by cranial tomography [BUZ08].

For $\Delta\xi$ being the beam width, and b^2 the size of the pixel, the weight α_{ij} is given

$$\alpha_{ij} = \frac{illuminated\ area\ of\ pixel\ j\ by\ ray\ i}{total\ area\ of\ pixel\ j} \tag{5.7}$$

for $0 \leq \alpha_{ij} \leq 1$.

Thus, the projection at each angle is the sum of non-overlapping, equally wide rays covering the FOV.

$$p_i = \sum_{j=1}^{N} \alpha_{ij} f_j \tag{5.8}$$

with $N=n^2$ the number of the pixels that need to be reconstructed.

Now, we could write all projections as a vector (one-column) matrix,

$$\mathbf{P} = (p_1, \ldots p_M)^T \tag{5.9}$$

with M being the number of projections multiplied with the number of rays.

Also, the values that are to be reconstructed

$$\mathbf{F} = (f_1, \ldots f_N)^T \tag{5.10}$$

The weightings are thus presented as an $M \times N$ matrix

$$\boldsymbol{A} = \begin{pmatrix} \alpha_{11} & \cdots & \alpha_{1N} \\ \vdots & \ddots & \vdots \\ \alpha_{M1} & \cdots & \alpha_{MN} \end{pmatrix} \tag{5.11}$$

and relation (5.8) would be written

$$\mathbf{P} = \boldsymbol{A}\ \mathbf{F} \tag{5.12}$$

This vector contains all values of the Radon space, which means it contains all values of the sinogram.

In conclusion, in the reconstruction procedure the intensity of each ray P_{ij} at a given angle can be calculated from the Projection Matrix A_{ij} and the Reconstructed Matrix F_j. The Projection Matrix A_{ij} is the weighting matrix, which carries the information of how much the j_{th} element of the matrix being reconstructed contributes to the i_{th}-ray. The Reconstructed Matrix F_j represents the unknown pattern of the planar image to be reconstructed and has usually the shape of a

square matrix with dimension $n \times n$, written in a vector matrix [ANG09].

There are mathematical constrains in this view on the reconstruction problem. First, the system of equations (5.12) can only be solved under idealized physical conditions, this is not the case in reality, since there is always noise that affects the acquired data. In most cases the number of projections is higher than the number of pixels leading to an over-determined system of equations. The system matrix, **A**, contains very small singular values making the reconstruction problem is an ill-conditioned problem. Additionally, the system matrix has a complicated structure, as a result no fast inversion has been found so far, and is also, very large making direct inversion impossible due to extremely instance time and memory requirements [BUZ08].

Solving eq. (5.12) using the inverse $\mathbf{A}^{-1}$ is not possible, since one could not calculate the inverse matrix. However, the solution can be found by other means. Solving the minimization problem

$$x^2 = |\boldsymbol{AF} - \boldsymbol{P}|^2 \tag{5.13}$$

always gives a solution. The solution is called the least squares minimum norm or pseudo solution [BUZ08].

Iterative ART is a reinvention of Kaczmarz's method published in 1937.

The scheme of the methods that follow iterative approaches follows the steps below. First, starting with the assumption that the realization of an image $\mathbf{F} = (f_1, \ldots, f_N)^T$ presents a point in an N-dimensional solution space, an initial image $\mathbf{F}^{(0)}$, is considered. Then a sequence of images, $\{\mathbf{F}^{(1)}, \mathbf{F}^{(2)},\ldots\}$ is calculated iteratively that converges to the desired tomographic reconstruction. Calculation of forward projection,

$$\mathbf{P}^{(k)} = \mathbf{A}\mathbf{F}^{(k)} \tag{5.14}$$

based on the k_{th} image approximation $\mathbf{F}^{(k)}$ is determined. The projection, $\mathbf{P}^{(k)}$, calculated in the k_{th} forward projection is compared with the actual measured projection, **P**. The result of this comparison between the determined and the measured projection leads to the correction specifications which will then applied to the k_{th} image approximation, $\mathbf{F}^{(k)}$, resulting in the $(k + 1)_{\text{th}}$ image approximation. This process is iteratively repeated such that with another forward projection, the projection $\mathbf{P}(k+1)$ is determined [BUZ08].

The duality of (5.12) between the matrix formalism and the backprojection leads to identification of an iteration equation. For $\mathbf{a}_i = (a_{i1}, a_{i2}, \ldots, a_{iN})$ being a certain row, i, of the system matrix $\mathbf{A}$, the image $\mathbf{F} = (f_1, \ldots, f_N)^T$ the solution vector, with $p_i = \sum_{j=1}^{N} \alpha_{ij} f_j$, this is the Radon transform, i.e., a projection value in the Radon space. The iteration equation, is given by

$$f^k = f^{(k-1)} - \frac{\mathrm{a}_i f^{(k-1)} - p_i}{\mathrm{a}_i (\mathrm{a}_i)^T} (\mathrm{a}_i)^T \qquad (5.15)$$

(Kak and Slaney 1988) [BUZ08].

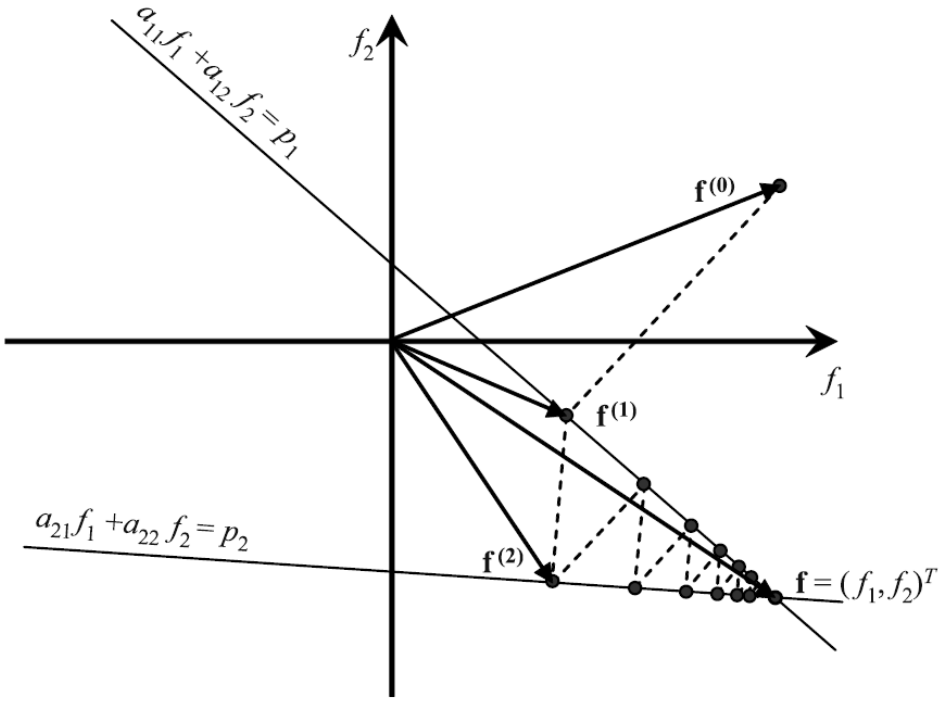

Figure 62. Iterative solution of two-dimensional system of equations as adapted from Kak and Slaney (1982) and Rosenfeld and Kak (1988) [BUZ08].

ART as an iterative method that it is has high computational requirements and is a slower approach than direct reconstruction methods, such as FBP, however, there are other advantages of the algebraic approach.

Irregular geometries of scanners or missing data in the sinogram lead to severe difficulties in the direct reconstruction methods. Using the matrix formalism these geometric conditions can be taken into account. Finite detector widths and different detector sensitivities can be also considered, thus better modeling of the real physical

measurement process is achieved. Beams running through objects that potentially produce inconsistencies in the Radon space can be weighted appropriately [BUZ08]. The strength of the algebraic and the statistical techniques is that linear physical processes can be built into the imaging model via appropriate weighting, the model corresponds to the real physical situation leading to improved imaging quality [BUZ08]. Iterative statistical techniques are widely used in nuclear imaging in order to overcome problems due to the low signal-to-noise ratio resulted by inadequate photon statistics.

After explaining that the use of an FFL enables projection reconstruction similarly to that of Computed Tomography, a correlation of the measured and needed data for image reconstruction in each case, would help to understand why ART can be used for an FFL reconstruction.

In comparison to projection reconstruction in CT, in MPI instead of the total intensity in each projection the measurements give the total signal induced by the SPIOs in the receive coil normalized with respect to the receive coil sensitivity.

At this point it should be mentioned that the normalization of the signal is achieved by dividing the received signal with the inner product of the receive coil sensitivity $\vec{p}$ and the unit vector in direction of the total magnetic field $\hat{n}$. This inner product though, is equal to zero when the direction of the FFL movement is perpendicular to the direction of the receive coil sensitivity. Leading to a zero received signal at this specific angle. For that reason, reconstruction of the complete Radon data of the SPIO particle distribution requires signal from more than one receive coil [ERB14]. At least two receive coils oriented in different directions with linearly independent sensitivities p_1 and p_2 should be chosen so that the signal cancellation is avoided when summarizing the signal. Of course, the receive coils must cover the whole FOV so that there is not any loss of information.

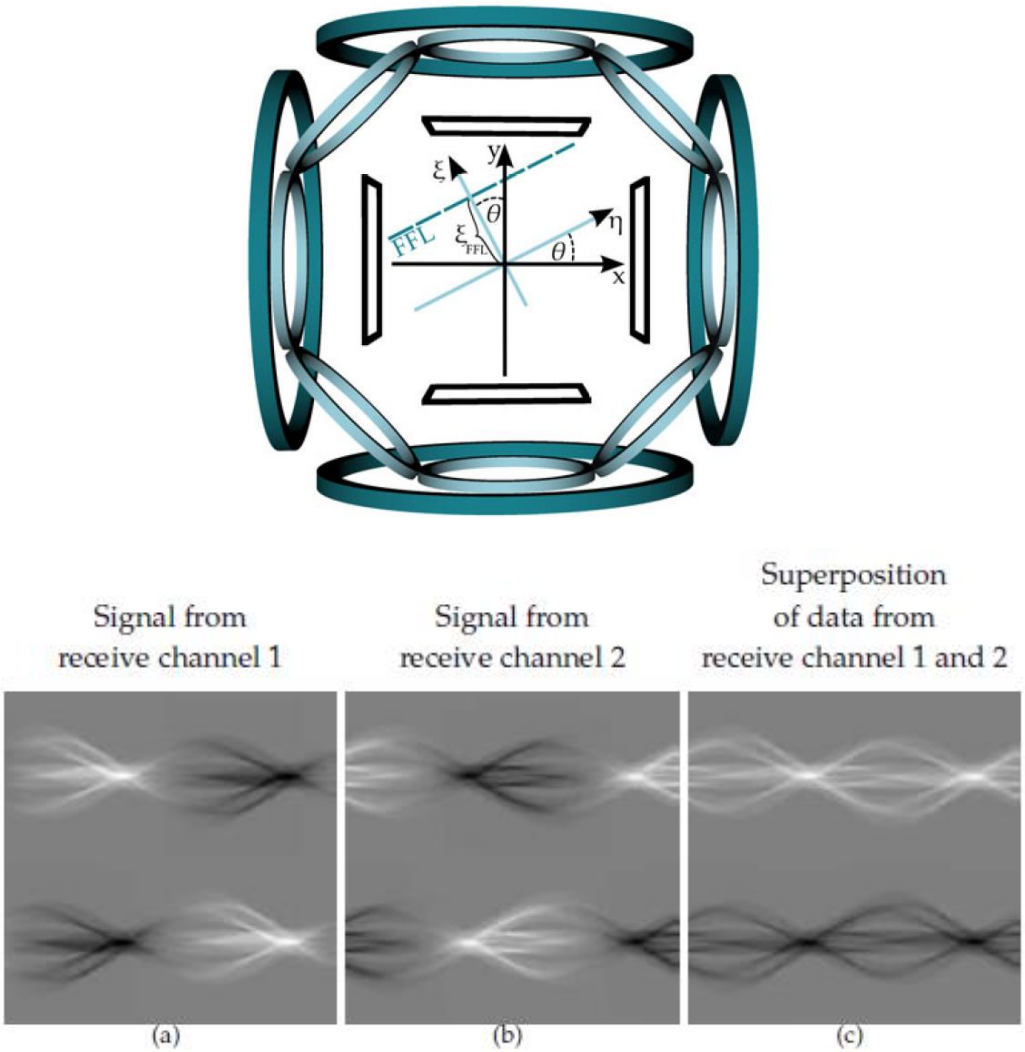

Figure 63. Illustration of an FFL scanner setup by [ERB14], with four rectangular receive coils (left). Right (a) and (b) show the voltage signal induced in two perpendicular receive coils and (c) the superposition of the two signals normalized with respect to the receive coil sensitivities [ERB14].

Additionally, in contrary to CT, the system matrix does not contain weights that reflects how much of the pixel that is to be reconstructed is passed through by the beam with respect to the entire area, but the form of the signal that comes from each pixel, based on the calibration measurement. Finally, the values that are to be reconstructed are not attenuation coefficients but SPIOs' concentration.

5.4 Quality of Reconstruction Procedure as a Function of the Number of Projections

In computed tomography, Fourier methods such as Radon transform and iterative reconstruction methods such as ART are the most commonly used for image reconstruction. Fourier methods are the preferred methods in applications where many projections can be

taken, however the algebraic methods have been shown to provide better results from either very few or limited views. Of course, the performance of these techniques decreases when projection data are missing or when a lot of noise is present.

As explained in previous subsection, ART solves the reconstruction problem by solving a linear system of equations. Considering a 4×4 system of equations, or a 2×2-pixel image, as presented in figure 64, using four projections from three projection angles is enough to determine the unknown values. When the grid that is to be reconstructed is finer, more projections have to be measured [BUZ08].

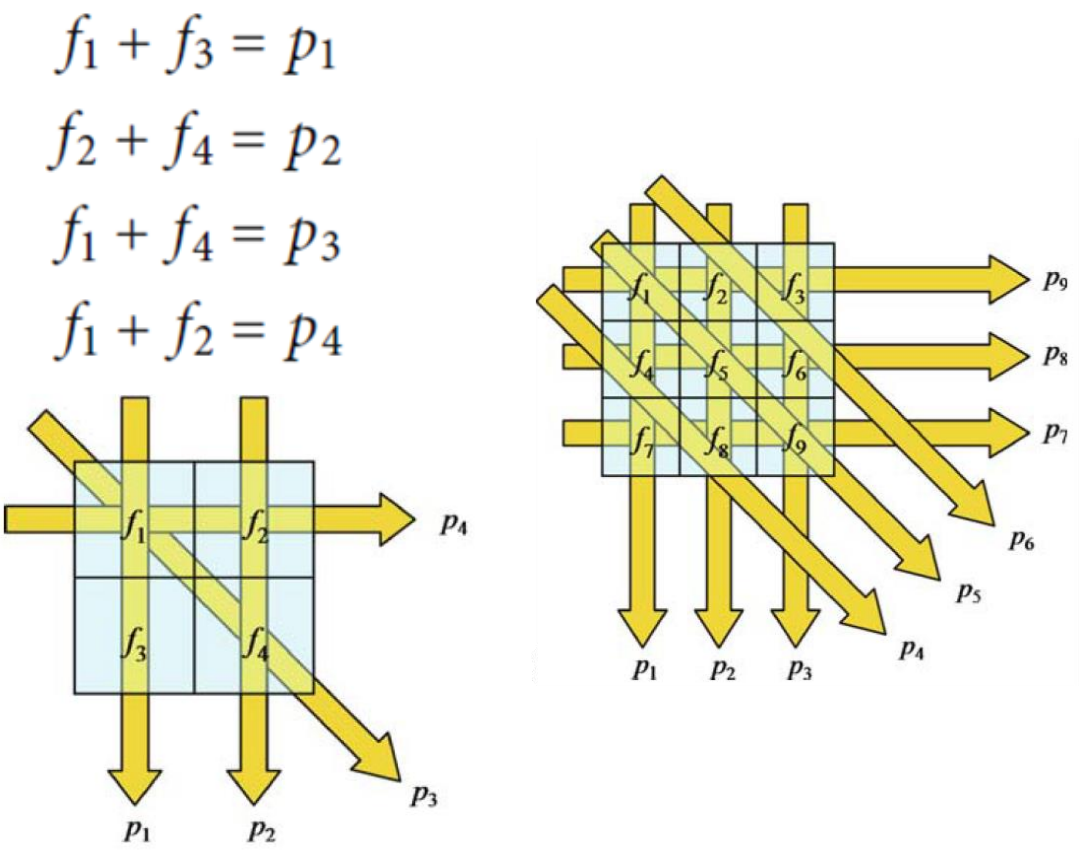

Figure 64. Sets of projections that results in a linear system of equations [BUZ08].

Next, reconstruction results by ART for different number of projections are presented.

First a simple phantom consisting of three sources, one circle and two ellipses of a Gaussian distribution, as shown in figure 65, was simulated using SIMULA. SIMULA is a tool for creating software phantoms and allows the use of these phantoms for reconstruction studies by creating tomographic projections. It's a custom-made code written in Fortran.

The phantom was discretized on a rectangular grid of matrix size 64×64 and the intensity of the sources was chosen to be the same for the two ellipses and the half of it for the circle.

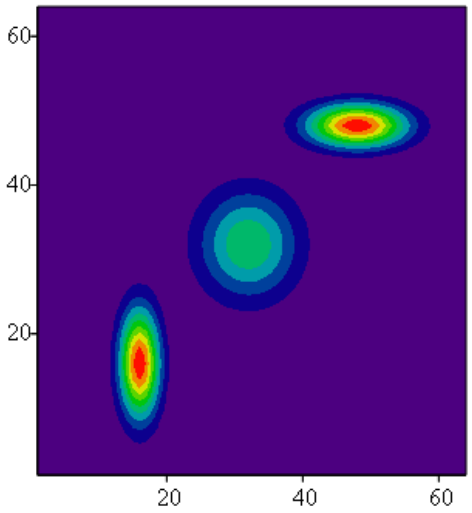

Figure 65. Software phantom created using SIMULA.

In the following figures the sinogram and the reconstructed images for this specific phantom, as resulted using ART algorithm are presented for different numbers of projections and the same iteration number.

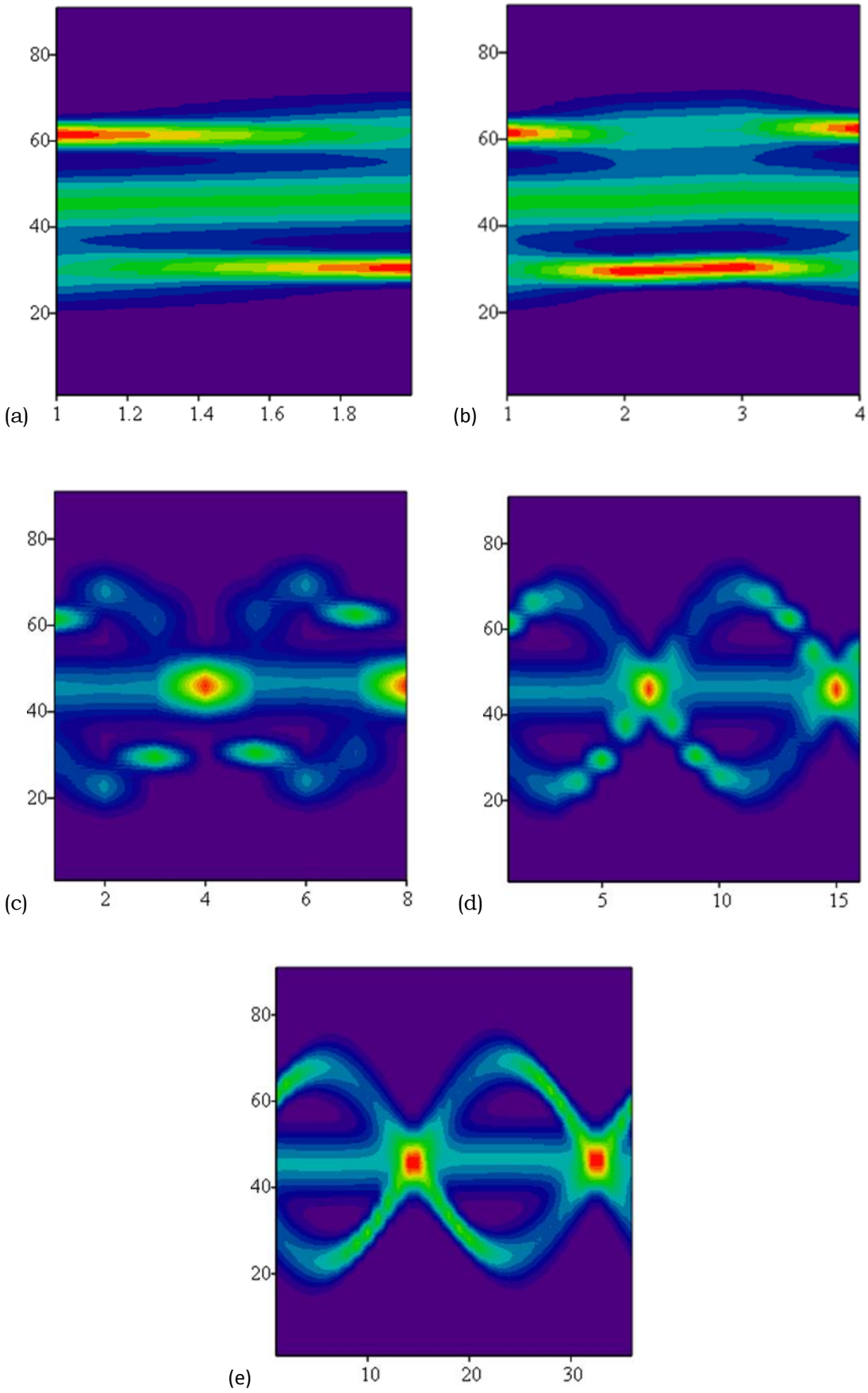

Figure 66. Resulted sinogram using ART for projection number: 2(a),4(b),8(c), 16(d) and 36(e) out of a range of 360º.

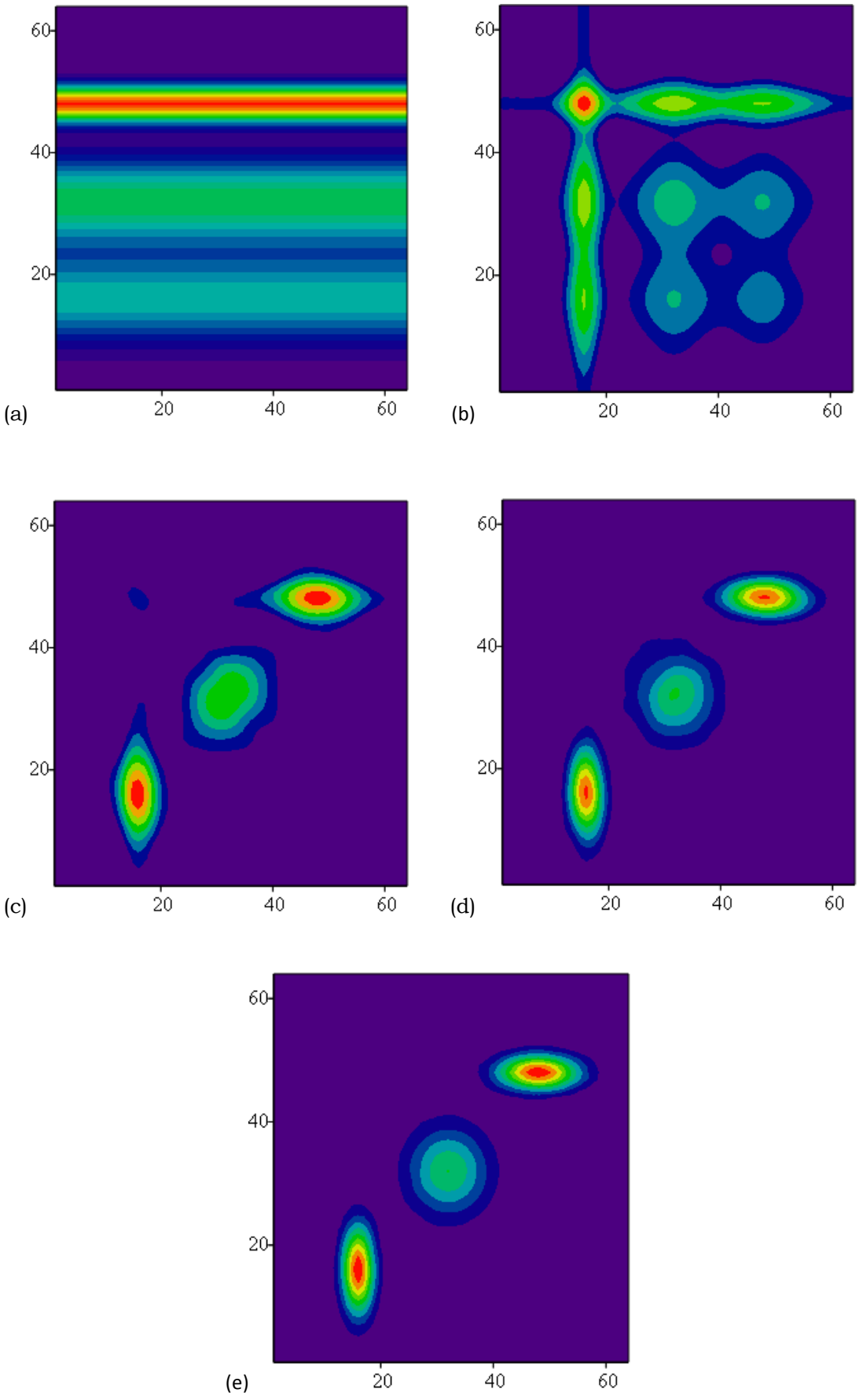

Figure 67. Reconstructed images using ART for projection number: 2(a),4(b), 8(c), 16(d) and 36(e) out of a range of 360º.

The image quality is obviously improving as the number of projections increases. Two or four projections are not enough to reconstruct the image. To evaluate how much the reconstructed image and the original image produced by SIMULA differ, chi square is calculated from the resulted reconstruction matrices by SIMULA and ART.

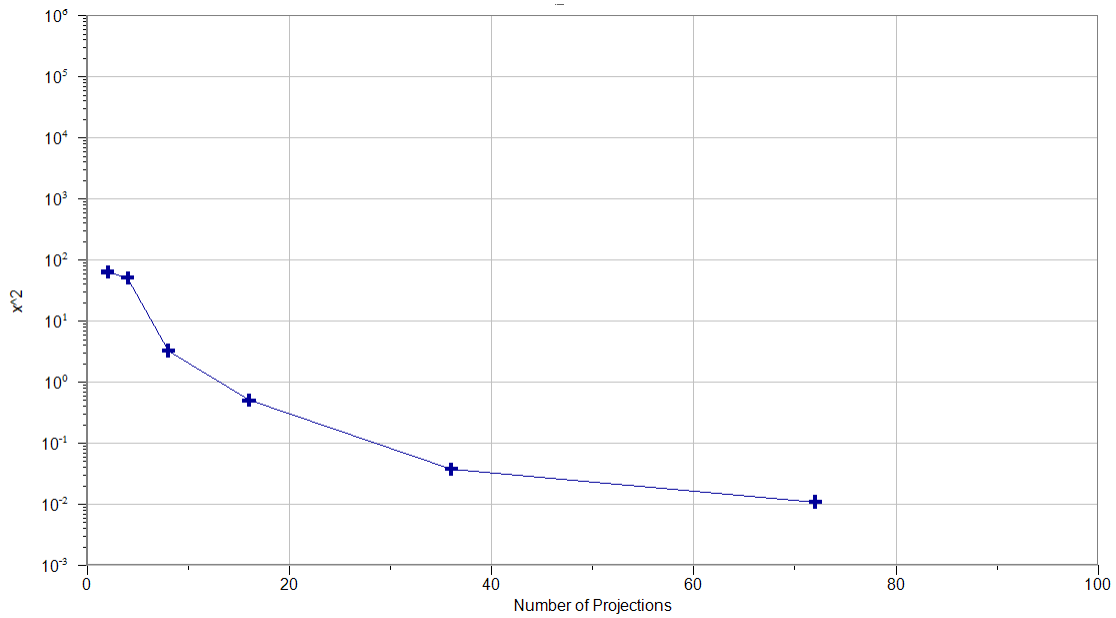

Figure 68. χ^2 with respect to the number of projections.

The reconstructed image using ART is converging to the original, produced by SIMULA, as the number of projections increases. Further increase in the projection number will not lead to a significant improvement.

5.5 Reconstruction with ART

In this section image reconstructions using ART are presented. The aim of these reconstructions is to eventually evaluate the impact of noise in the reconstruction of an MPI image using ART.

The Digital Subtraction Angiography (DSA) reconstructed image of a phantom of internal carotid artery with a sacciform aneurysm as given by [WEL20], was considered as the ideal reconstructed image (fig. 69) and converted into a software phantom using SIMULA as illustrated in figure 70.

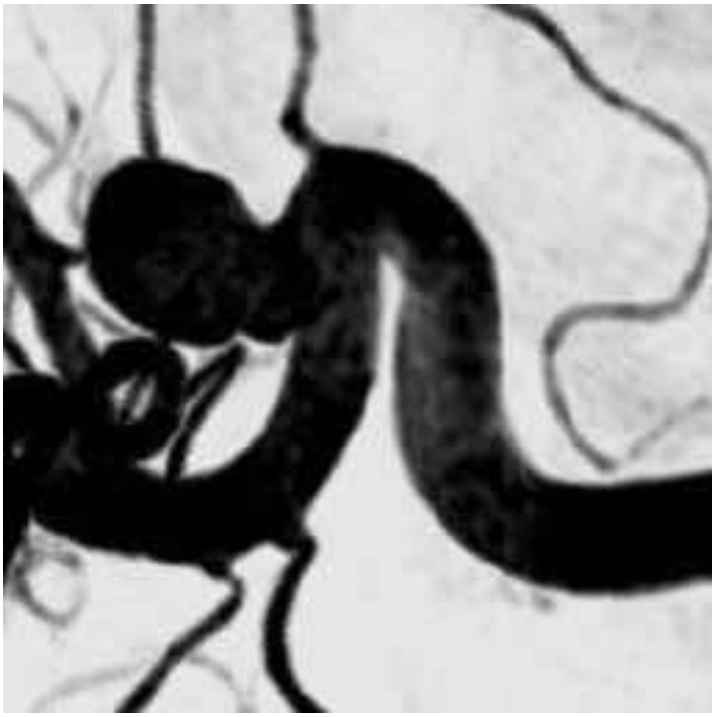

Figure 69. DSA reconstructed image of a phantom of internal carotid artery with a sacciform aneurysm [WEL20].

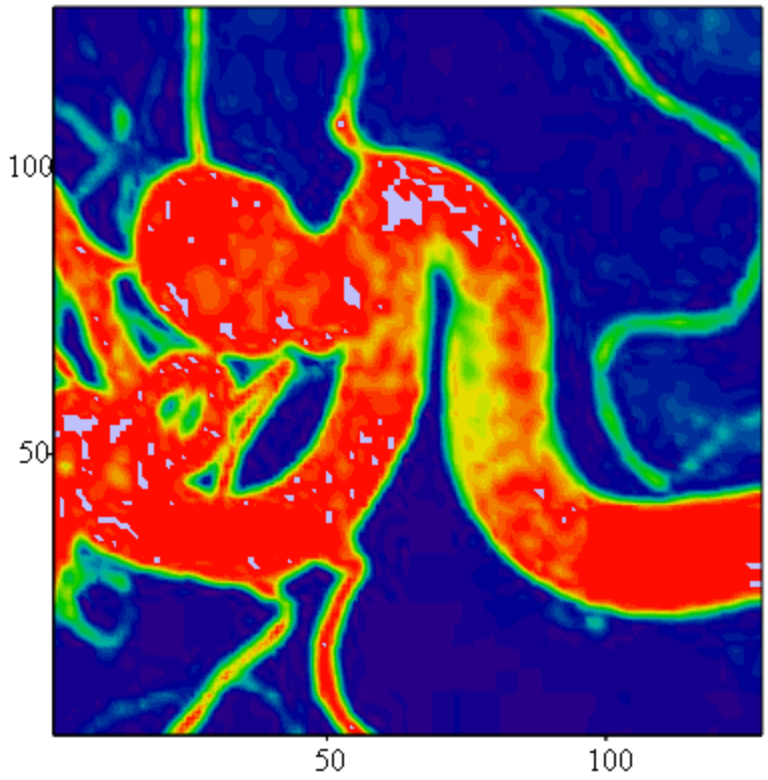

Figure 70. Software phantom of carotid artery with a sacciform aneurysm created using SIMULA.

The phantom was discretized on a rectangular grid of matrix size 128×128. Image reconstruction of the Phantom using ART followed, the number of projections was chosen to be 72 out of a 360° range

and the Grand iteration number was equal to 4. The reconstruction results are shown in fig. 71.

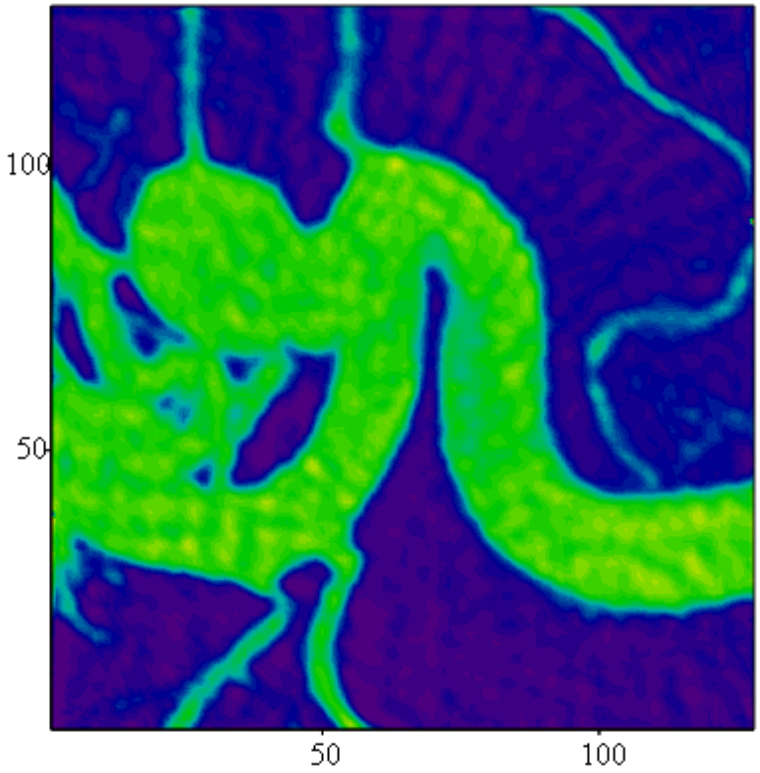

Figure 71. Reconstructed image of the carotid artery phantom using ART.

The reconstructed image as illustrated in figure 70, is the ideal reconstructed result. All the reconstructed images that follows were compared to this image in order to evaluate the effect of noise in the quality of the images. The number of projections and the number of iterations remained the same.

In MPI field homogeneity along the FFL and parallel to its alignment depends on the position of interest within the FOV. The decreasing field quality as increasing distance to the center leads to artifacts in the reconstructed image, thus the image quality is lower in the edges than the center. Intrinsic noise of the detector is also one of the main noise sources.

To add noise in the image, a normal distribution with a standard deviation σ and zero mean, was considered, so that the noise is generated from normally distributed random numbers, in each projection the random numbers generated equals to the number of elements in the projections. The results for different choices of σ are presented in the figures below.

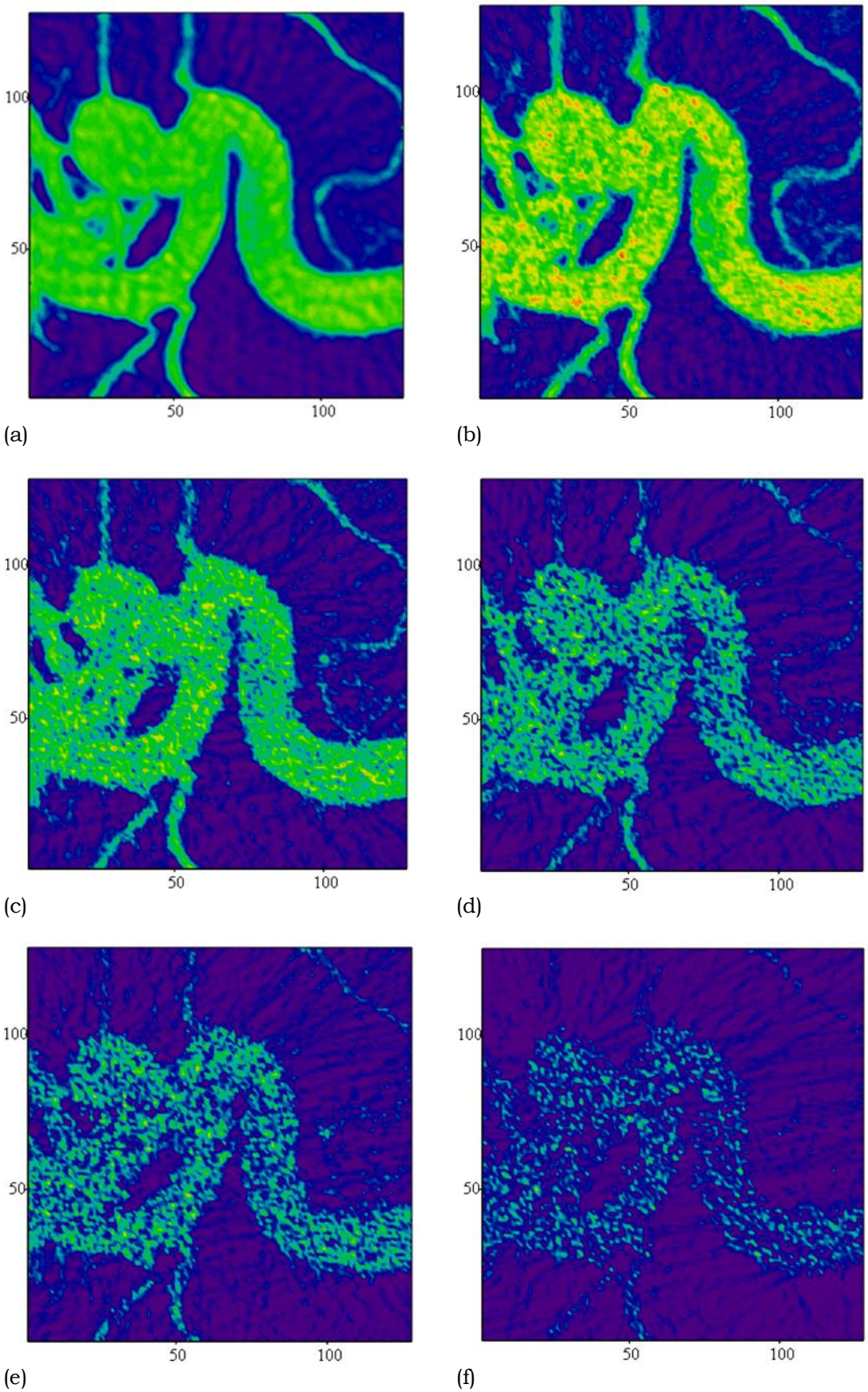

Figure 72. Reconstructed images of the carotid artery phantom using ART without noise (a) and with 2%(b), 5%(c), 8%(d), 10%(e) and 15%(f) Gaussian noise.

In order to introduce a more realistic model of noise and evaluate the effect of it in the reconstructed image an analog linear attenuation was added in the noise model so that there is zero attenuation in the center and linear increase towards the edges of the FOV. This noise model now includes the presence of analog signal distortion.

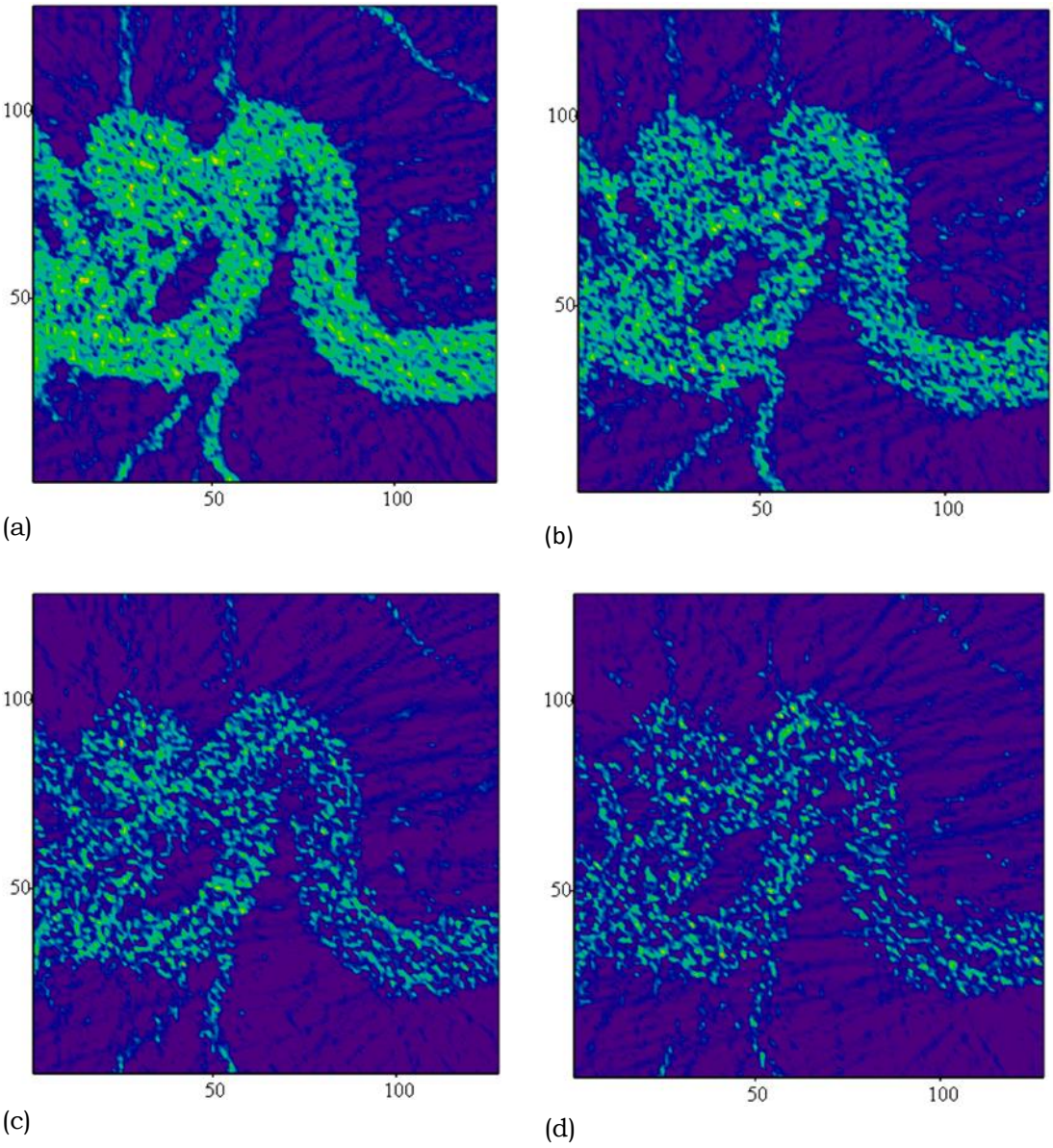

Figure 73. Reconstructed images of the carotid artery phantom using ART with 5% Gaussian noise and additional attenuation 15%(a), 25%(b), 35%(c) and 45% (d).

As expected, as the noise increases, the quality of the image is negatively affected. The image becomes blurrier, the boundaries are no longer well-defined and the details mostly out of the center can hardly be observed. However, there seems to be sufficient noise tolerance as small structures can be distinguished even for high noise levels. Enhanced ART with noise correction schemes could improve the results.

CHAPTER 6. CONCLUDING REMARKS

Magnetic Particle Imaging is a new medical imaging technique capable of directly imaging the distribution of Superparamagnetic iron oxide nanoparticles. MPI is still under development, pre-clinical researches show that high sensitivity, high resolution and fast image acquisition are some of the advantages that MPI has to offer. In addition, MPI provides high contrast, since the signal contrast results only from the SPIOs that have been injected into the body, and there is no background signal from other biological tissues. There is also zero signal attenuation due to different depths of interaction. These advantages indicate that MPI possibly outperforms imaging modalities such as Magnetic Resonance Imaging (MRI) and Computed Tomography (CT). The combination of MPI/CT and MPI/MRI is extremely promising.

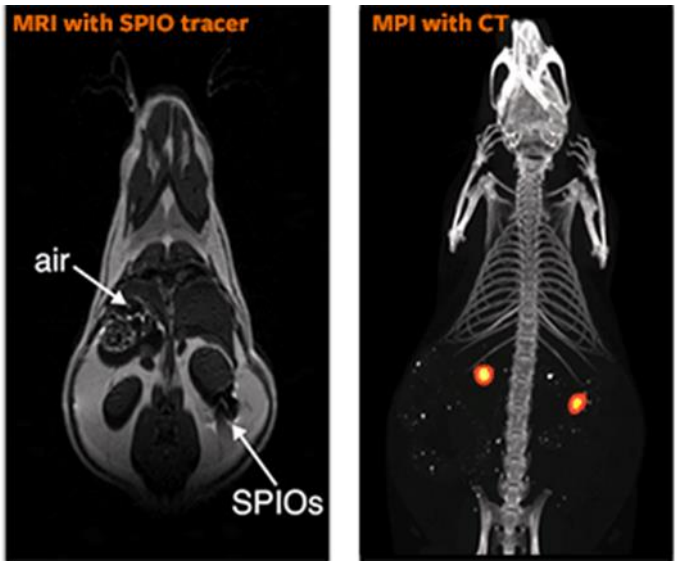

Figure 74. Comparison of MRI and MPI/CT in mouse [TAL19].

MPI is a tracer-based imaging technique, thus it could potentially replace Positron Emission Tomography (PET) and Single Photon Emission Tomography (SPECT), which are also tracer-based modalities but in contrast to MPI they use ionizing radiation.

	CT	MRI	PET	SPECT	MPI
Spatial resolution	0.5 mm	1 mm	4 mm	3-10 mm	1 mm
Acquisition time	1 s	10s	1 min	1 min	<0.1 s
Sensitivity	Low	Low	High	High	High
Quantifiability	Yes	No	Yes	Yes	Yes
Patient Risk	X-ray	Heating	β/γ radiation	γ radiation	Heating

Figure 75. Characterization of different image modalities [KAE14], [BUZ12], [WU19].

At first MPI was developed as an imaging technique capable for applications such as vascular imaging, angiography, oncology, inflammation, stem cell tracking, etc. The ability of MPI to visualize medical devices such as guide wires and catheters during an intervention has been investigated so did the guided drug delivery. MPI also seems to be a promising modality for hyperthermia treatment.

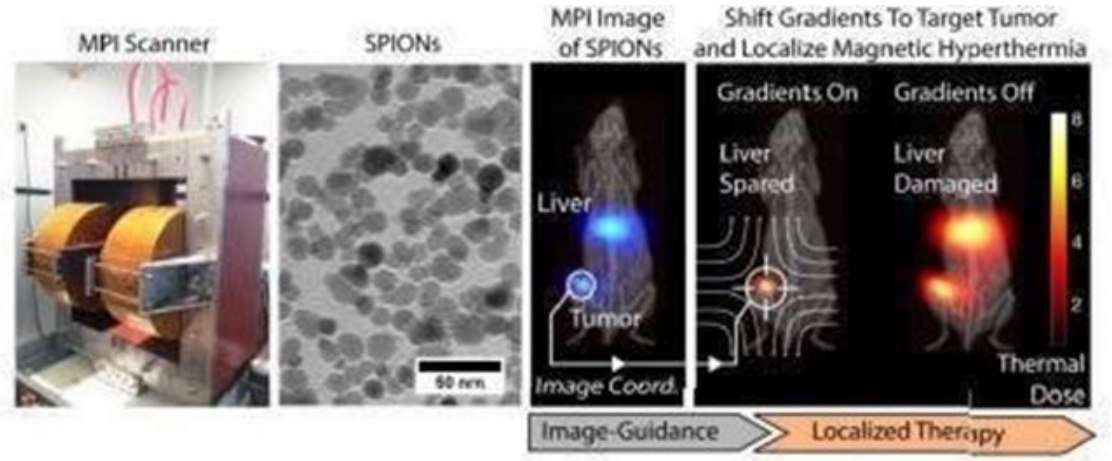

Figure 76. Magnetic Particle Imaging and pin point hyperthermia treatment/drug delivery in one [TAY18].

The basic principle of MPI is based on the nonlinear magnetization behavior of the SPIO tracer nanoparticles. MPI signal is generated from the tracers as they respond to applied magnetic fields. SPIOs, described by Langevin theory, magnetically align with external applied magnetic fields until they reach magnetization saturation. The application of an external sinusoidal magnetic field with fundamental frequency f_E (Drive field) causes a non-sinusoidal oscillation of particles magnetization. This change in magnetization induces a voltage in receive coils. Existence of higher harmonics in the Fourier spectrum of the measured voltage gives evidence for the existence of

SPIO particles inside the volume of interest. For spatial encoding of the MPI signal, one or more gradient fields (Selection field) are used to magnetically saturate all SPIOs out of a central Field-Free Region (FFR). Shifting this FFR through the imaging volume results in the magnetization change of the SPIOs in this region, whereas SPIOs around this region are saturated. As a result, only particles near this specific region contribute to the measured signal. Simulations that were conducted verify this principle of operation. Different scanner topologies have been suggested, aiming eventually to the construction of a human sized MPI scanner.

In MPI, spatial encoding can be achieved either by implementing a Field Free Point (FFP) or a Field Free Line (FFL) technique. FFP encoding scheme has a major disadvantage. The resolution as well as the SNR of this sensitive spot imaging method depend on the gradient strength of the selection field, an increase in the gradient strength results to the improvement of the spatial resolution but, at the same time, reduces the SNR. Field Free Line Magnetic Particle Imaging overcomes this problem and also allows reconstruction based on well-known projection reconstruction techniques.

Since, the reconstruction of an MPI image results from the solution of a linear system of equations, Algebraic Reconstruction Technique is an obvious choice. However, it is known that ART is noise-sensitive; this means that the convergence behavior becomes worse as noise covers the data. In MPI there are different sources that generates noise. Field inhomogeneities of the drive field, non-linearity of the gradient field and the intrinsic noise of the detector are the main causes of noise when proper sampling density and SPIO ferrofluid concentration is used. The simulation and addition of that type of noise in the data verifies that even though traditional ART is a possible solution for MPI with an FFL encoding scheme reconstruction, there is room for improvement in order to overcome artifacts generated by background noise and analog signal distortion.

Bibliography

[ANG09] Angeli Stelios, Stiliaris Efstathios: "*An Accelerated Algebraic Reconstruction Technique based on the Newton-Raphson Scheme*", IEEE Nuclear Science Symposium conference record. Nuclear Science Symposium, DOI: 10.1109/NSSMIC.2009.5401763, 2009.

[BOR12] Jörn Borgert *et al.* "*Fundamentals and applications of magnetic particle imaging*", Journal of cardiovascular computed tomography, DOI:10.1016/j.jcct.2012.04.007, 2012

[BUZ08] T. M. Buzug: "*Computed Tomography: From Photon Statistics to Modern Cone-Beam CT*", Springer, DOI: 10.1007/978-3-540-39408-2, ISBN: 978-3-540-39407-5, e-ISBN: 978-3-540-39408-2, 2008.

[BUZ10] T.M Buzug *et al.*: "*MAGNETIC NANOPARTICLES Particle Science, Imaging Technology, and Clinical Applications Proceedings of the First International Workshop on Magnetic Particle Imaging*", Institute of Medical Engineering, University of Lübeck, Germany, World Scientific Publishing Co. Pte. Ltd., ISBN:13 978-981-4324-67-0, ISBN:10 981-4324-67-1, 2010.

[BUZ12] T.M Buzug *et al.*: "*Magnetic particle imaging: Introduction to imaging and hardware realization*", Z. Med Phys. 22(2012) 323-334.

[COM] Introduction to COMSOL Multiphysics, COMSOL Documentation, © 1998–2015 COMSOL.

[ERB12] Erbe Marlitt *et al.*: "*Influence of Magnetic Field Optimization on Image Quality Achieved for Efficient Radon based Reconstruction in Field Free Line Imaging in MPI*", Springer Proceedings in Physics 140, 2012.

[ERB14] Erbe Marlitt, "*Field Free Line Magnetic Particle Imaging*", Springer Vieweg, ISBN: 978-3-658-05336-9, e-ISBN: 978-3-658-05337-6, 2014.

[FEE15] Feeman, T. G.: "*Algebraic Reconstruction Techniques. The Mathematics of Medical Imaging",* 137–161. DOI:10.1007/978-3-319-22665-1_9, 2015.

[FIC15] Bradley W. Ficko, Paolo Giacometti, Solomon G.Diamond, "*Nonlinear susceptibility magnitude imaging of magnetic nanoparticles*", Journal of Magnetism and Magnetic Materials, 378(2015)267–277.

[FON19] A. Fontanet *et al.*: "*Design and construction of 3D Helmholtz Coil system to calibrate 3D Hall probes"*, JACoW Publishing, ISBN: 978-3-95450-208-0, DOI:10.18429/JACoW-IPAC2019-THPTS055, 2019.

[GEH10] Gehrcke Jan-Philip: "*Characterization of the Magnetic Particle Imaging Signal Based on Theory, Simulation, and Experiment*", Master of Science with Honors in Physics thesis, University of Würzburg, 2010.

[GLE05] B. Gleich, J. Weizenecker: "*Tomographic imaging using the nonlinear response of magnetic particles*", *Nature,* 435:1214-1217, 2005.

[GLE08] B. Gleich, J. Weizenecker, J. Borgert: "*Experimental results on fast 2D-encoded magnetic particle imaging*", *Phys. Med. Biol.,* 53: N81-N84, 2008.

[GLE13] B. Gleich: "*Principles and Applications of Magnetic Particle Imaging*", Springer Vieweg, ISBN: 978-3-658-01960-0, e-ISBN: 978-3-658-01961-7, 2013.

[GOO10] P. W. Goodwill, S. M. Conolly: "*The x-space formulation of the magnetic particle imaging process: One dimensional signal, resolution, bandwidth, SNR, SAR, and magneto stimulation*", IEEE Trans. Med. Imaging, 29(11):1851-1859, 2010.

[GOO11] P. W. Goodwill and S. M. Conolly: "*Multidimensional x-space magnetic particle imaging*", IEEE Trans. Med. Imaging, 30(9):1581-1590, 2011.

[GOO12] P. W. Goodwill et al.: "*Projection X-Space Magnetic Particle Imaging*", IEEE Trans Med Imaging, 31(5): 1076–1085. doi:10.1109/TMI.2012.2185247, 2012.

[GOR74] *Gordon, R.: "A tutorial on art (algebraic reconstruction techniques)", IEEE Transactions on Nuclear Science, 21(3), 78-93, doi:10.1109/tns.1974.6499238, 1974.*

[GRA13] M. Graeser *et al.*: "*Analog receive signal processing for magnetic particle imaging*", Medical Physics. 40(no. 4):042303, 2013.

[GRI99] D.J. Griffiths: "*Introduction to Electrodynamics*", 3rd edition, Prentice-Hall, ISBN-10: 013805326X, ISBN-13: 9780138053260, 1999.

[GRU13] Grüttner M. *et al.*: "*On the formulation of the image reconstruction problem in magnetic particle imaging*", Biomedizinische Technik /Biomedical Engineering, 58(6). DOI:10.1515/bmt-2012-0063, 2013.

[HOU11] D.I. Hoult, Historical Perspective "*The Principle of Reciprocity*", Journal of Magnetic Resonance 213 (2011) 344–346

[KAE14] C. Kaethner *et al.: "On the Way to a Patient Table Integrated Scanner System in Magnetic Particle Imaging",* Proceedings of SPIE - The International Society for Optical Engineering 9038, DOI: 10.1117/12.2042765, 2014

[KNO09] T. Knopp *et al.*: "*Trajectory Analysis for Magnetic Particle Imaging*", Physics in Medicine and Biology, 54(2):385-397, 2009.

[KNO10] T. Knopp *et al.*, "*Model-Based Reconstruction for Magnetic Particle Imaging*" IEE Trans. Med. Imaging, 2010, vol. 29.

[KNO11] Tobias Knopp *et al.,* "*Receive Coil Array for Magnetic Particle Imaging*", IEEE, 2011.

[KNO12] T. Knopp "*Magnetic Particle Imaging: An Introduction to Imaging Principles and Scanner Instrumentation*", Springer Vieweg, ISBN: 978-3-642-04198-3, ISBN: 978-3-642-04199-0 (eBook), 2012.

[KNO15] M.T Knopp, A. Weber, "*Sparse Reconstruction of the Magnetic Particle Imaging System*", IEEE, 2015.

[KNO17] T. Knopp, N. Gdaniec and M. Möddel: "*Magnetic particle imaging: from proof of principle to preclinical applications*", Phys. Med. Biol. 62 (2017) R124–R178.

[KON11] J. Konkle, P. Goodwill, and S. Conolly, "*Development of a Field Free Line Magnet for Projection MPI*" in Proc. SPIE 7965, Medical Imaging 2011: Biomedical Applications in Molecular, Structural, and Functional Imaging, vol. 7965, p. 79650X-79650X-7, 2011.

[KON13] J. Konkle et al.: "*Projection Reconstruction Magnetic Particle Imaging*", IEEE, Trans Med Imaging., 32(2): 338–347, DOI:10.1109/TMI.2012.2227121, 2013.

[LAW97] Lawaczeck R. *et al.*: "*Magnetic iron oxide particles coated with carboxydextran for parenteral administration and liver contrasting*", Acta Radiol. 38, 584–597 ,1997.

[MED15] Medimagh H. *et al.* "*Artifacts in field free line magnetic particle imaging in the presence of inhomogeneous and nonlinear magnetic fields",* De Gruyter, Current Directions in Biomedical Engineering, 1:245–248, DOI: 10.1515/CDBME-2015-0061, 2015.

[PAN15] Panagiotopoulos *et al.*: "*Magnetic particle imaging: current developments and future directions*", International journal of medicine, 2015:10 3097-3114.

[RAH09] J. Rahmer *et al.:* "*Signal encoding in magnetic particle imaging: properties of the system function*", BMC Medical Imaging, 9:4 DOI:10.1186/1471-2342-9-4, 2009.

[RAP98] Raparia, D., Alessi, J., & Kponou, A. (n.d.).: "*The Algebraic Reconstruction Technique (ART)*", Proceedings of the 1997 Particle Accelerator Conference (Cat. No. 97CH36167), DOI:10.1109/pac.1997.751094, 1998.

[SCH15] Schulz V., *et al.*: "*A Field Cancelation Signal Extraction Method for Magnetic Particle Imaging*", *IEEE Trans. Magn.* DOI:10.1109/TMAG.2014.2325852, 2015.

[STR15] Marcel Straub *et al.*: "*Flexible and modular MPI simulation framework and its use in modeling a µMPI", IEE, Trans. Magn., DOI: 10.1109/TMAG.2014.2329733, 2015.*

[TAL19] Nazanin Talebloo *et al.*: "*Magnetic Particle Imaging: Current Applications in Biomedical Research*", Journal of Magnetic Resonance Imaging, DOI: 10.1002/jmri.26875, 2019.

[TAY18] Zhi Wei Tay *et al.* "*Magnetic Particle Imaging-Guided Heating in Vivo Using Gradient Fields for Arbitrary Localization of Magnetic Hyperthermia Therapy"* ACS Nano, 12,4, 3699-3713, doi.org/10.1021/acsnano.8b00893, 2018.

[TOP19] Can Bariş Top *et al.*, "*Trajectory analysis for field free line magnetic particle imaging*", Medical Physics, 46 (4), doi.org/10.1002/mp.13411, 2019.

[WAL12] Waldemar T. Smolik *et al.*: "*Numerical Modeling of Magnetic Field for Magnetic Particle Imaging",* IEE, DOI: 10.1109/IST.2012.6295571, 2012.

[WEI07] Weizenecker J, Borgert J, Gleich B: "*A simulation study on the resolution and sensitivity of magnetic particle imaging*", Phys. Med. Biol., 52:6363-6374, 2007.

[WEI08] Weizenecker J, Gleich B, Borgert J: "*Magnetic particle imaging using a field free line*". *J Phys D: Appl Phys,* 41:105009, 2008.

[WEI09] Weizenecker J *et al.*: "*Three-dimensional real-time in vivo magnetic particle imaging*". Phys. Med. Biol., 54(5): L1-L10, 2009.

[WEL20] Weller D. *et al.*: "*Combining Direct 3D Volume Rendering and Magnetic Particle Imaging to Advance Radiation-Free Real-Time 3D Guidance of Vascular Interventions*", Cardiovascular and Interventional Radiological Society of Europe 43:322–330, DOI:10.1007/s00270-019-02340-4, 2020.

[WIKI] https://en.wikipedia.org/

[WU19] L. C. Wu *et al.*: "*A Review of Magnetic Particle Imaging and Perspectives on Neuroimaging*", AJNR Am J Neuroradiol., 40(2): 206–212, DOI: 10.3174/ajnr.A5896, 2019

[ZHA17] Xingming Zhang, Tuan-Anh Le, Jungwon Yoon, "*Development of a real time imaging-based guidance system of magnetic nanoparticles for targeted drug delivery*", Journal of Magnetism and Magnetic Materials 427 (2017) 345–351

[ZHE15] Bo Zheng: "*System Hardware and in vivo Cell Tracking in Magnetic Particle Imaging*", UC Berkeley, 2015.